Monthly Notices of the ROYAL ASTRONOMICAL SOCIETY

MNRAS **546**, 1–38 (2026) https://doi.org/10.1093/mnras/stag086
Advance Access publication 2026 January 16

JADES: comprehensive census of broad-line AGN from reionization to cosmic noon revealed by JWST

Ignas Juodžbalis ,[1,2★] Roberto Maiolino,[1,2,3] William M. Baker ,[1,2,4] Emma Curtis Lake ,[5] Jan Scholtz ,[1,2] Francesco D'Eugenio ,[1,2] Bartolomeo Trefoloni,[6,7,8] Yuki Isobe ,[1,2,9] Sandro Tacchella ,[1,2] Andrew J. Bunker,[10] Stefano Carniani,[8] Stéphane Charlot,[11] Gareth C. Jones,[1,2] Eleonora Parlanti,[8,12] Michele Perna,[13] Pierluigi Rinaldi,[14] Brant Robertson,[15] Hannah Übler,[12] Giacomo Venturi[8] and Chris Willott[16]

[1] *Kavli Institute for Cosmology, University of Cambridge, Madingley Road, Cambridge CB3 OHA, UK*
[2] *Cavendish Laboratory – Astrophysics Group, University of Cambridge, 19 JJ Thomson Avenue, Cambridge CB3 OHE, UK*
[3] *Department of Physics and Astronomy, University College London, Gower Street, London WC1E 6BT, UK*
[4] *DARK, Niels Bohr Institute, University of Copenhagen, Jagtvej 128, DK-2200 Copenhagen, Denmark*
[5] *Department of Physics, Astronomy and Mathematics, Centre for Astrophysics Research, University of Hertfordshire, Hatfield AL10 9AB, UK*
[6] *Dipartimento di Fisica e Astronomia, Università di Firenze, via G. Sansone 1, I-50019 Sesto Fiorentino, Firenze, Italy*
[7] *INAF – Osservatorio Astrofisico di Arcetri, Largo Enrico Fermi 5, I-50125 Firenze, Italy*
[8] *Scuola Normale Superiore, Piazza dei Cavalieri 7, I-56126 Pisa, Italy*
[9] *Faculty of Science and Engineering, Waseda Research Institute for Science and Engineering, Waseda University, 3-4-1, Okubo, Shinjuku, Tokyo 169-8555, Japan*
[10] *Department of Physics, University of Oxford, Denys Wilkinson Building, Keble Road, Oxford OX1 3RH, UK*
[11] *Sorbonne Université, CNRS, UMR 7095, Institut d'Astrophysique de Paris, 98 bis bd Arago, F-75014 Paris, France*
[12] *Max-Planck-Institut für extraterrestrische Physik (MPE), Gießenbachstraße 1, D-85748 Garching, Germany*
[13] *Centro de Astrobiologia (CAB), CSIC–INTA, Cra. de Ajalvir Km. 4, E-28850 Torrejón de Ardoz, Madrid, Spain*
[14] *Steward Observatory, University of Arizona, 933 N. Cherry Avenue, Tucson, AZ 85721, USA*
[15] *Department of Astronomy and Astrophysics University of California, Santa Cruz, 1156 High Street, Santa Cruz, CA 96054, USA*
[16] *NRC Herzberg, 5071 West Saanich Rd, Victoria, BC V9E 2E7, Canada*

Accepted 2025 December 23. Received 2025 November 13; in original form 2025 April 7

ABSTRACT

The depth and coverage of the first years of *James Webb Space Telescope* observations have revealed low-luminosity active galactic nuclei (AGN) across a wide redshift range, shedding light on black hole (BH) assembly and feedback. We present our spectroscopic sample of 34 Type 1 AGN obtained from JADES survey data and spanning $1.5 < z < 9$. Our sample of AGN probes a BH mass range of 10^{6-9} M$_{\odot}$ at bolometric luminosities down to 10^{43} erg s^{-1}. Most of these AGN are hosted in low-mass ($M_{\star} \sim 10^{8}$ M$_{\odot}$) galaxies and are overmassive relative to the local M_{BH}–$M_{\star}$ relation, while remaining consistent with the local M_{BH}–σ_{*} relation. The wide redshift range provided by our sample allows us to trace the emergence of local M_{BH}–M_{*} scaling relation across cosmic time. Additionally, we explore the capability of narrow-line diagnostics in identifying Type 2 AGN and find that a significant fraction of our AGN would be missed by them due to low metallicity or lack of high-energy ionizing photons. We explore the UV luminosity function of AGN and their hosts and find that it is subject to significant cosmic variance and is also dependent on the AGN bolometric luminosity. Finally, we show that the electron scattering scenario recently proposed to explain broad Balmer lines is untenable on multiple grounds showing that there is no evidence of significant BH mass overestimation.

Key words: galaxies: active – quasars: supermassive black holes – galaxies: Seyfert.

1 INTRODUCTION

The origin and growth of the first supermassive black holes (SMBHs) and their influence on the galaxies hosting them have long remained an open problem in astrophysics. Tight scaling relations connecting the black hole (BH) mass to host galaxy properties found in local active galactic nuclei (AGN) (J. Kormendy & L. C. Ho 2013; A. E. Reines & M. Volonteri 2015; J. E. Greene, J. Strader & L. C. Ho 2020) suggest a strong coupling between BH and galaxy evolution. However, while various surveys have greatly expanded the redshift frontier through the years (A. Merloni et al. 2010; A. Bongiorno et al. 2014; J. Lyu et al. 2022),

---

★ E-mail: ij284@cam.ac.uk

until recently rest-frame optical studies in the $z > 4$ regime have remained limited to only the brightest and most massive quasars (QSOs) (X. Fan, E. Bañados & R. A. Simcoe 2023; C. Mazzucchelli et al. 2023), missing the low-mass low-luminosity AGN and complicating investigation into BH seeding and emergence of local scaling relations. Nevertheless, the presence of $\sim 10^9$ $M_\odot$ BHs at redshifts as high as 7 (E. Bañados et al. 2018; F. Wang et al. 2020) had already reinvigorated interest in SMBH seeding models. These models invoke direct collapse BHs (V. Bromm & A. Loeb 2003; Y. Luo et al. 2018), seeds produced by runaway collisions in dense clusters (M. B. Davies, M. C. Miller & J. M. Bellovary 2011; P. Kroupa et al. 2020), or Population III stellar remnants growing at super-Eddington rates (A. Trinca et al. 2022; R. Schneider et al. 2023), among other scenarios, in an attempt to explain these discoveries. The need to test these models has presented an even stronger impetus to search for smaller and less luminous BHs at high redshifts.

Feedback from AGN has also been invoked as a potential quenching mechanism that prevents high-mass galaxies from forming stars, bridging the discrepancy between galaxy luminosity and dark matter halo mass functions (A. Man & S. Belli 2018). However, the exact shape this feedback takes and its role in early galaxy formation is still an open problem, necessitating population studies probing AGN and their hosts at high redshifts (C. M. Harrison & C. Ramos Almeida 2024).

The launch of *James Webb Space Telescope* (*JWST*) has greatly expanded the scope of AGN research possible in the high-redshift regimes with results from first spectroscopic surveys revealing abundant populations of faint Type 1 AGN out to well before the epoch of reionization (Y. Harikane et al. 2023; J. E. Greene et al. 2024; R. Maiolino et al. 2024; J. Matthee et al. 2024; A. J. Taylor et al. 2024), exhibiting broad features in their Balmer emission lines. However, these discoveries soon posed more questions than answers, with the newfound objects displaying considerable X-ray weakness (T. T. Ananna et al. 2024; R. Maiolino et al. 2025; M. Yue et al. 2024a), radio weakness (G. Mazzolari et al. 2025, 2024a), signatures of metal poor broad-line region (BLR; B. Trefoloni et al. 2024), and being significantly overmassive with respect to the local BH mass–stellar mass relations (Y. Harikane et al. 2023; H. Übler et al. 2023; I. Juodžbalis et al. 2024b; R. Maiolino et al. 2024). These overmassive, yet in some cases dormant ($\lambda_{Edd} < 0.05$), BHs have presented compelling evidence for having experienced phases of super-Eddington growth (I. Juodžbalis et al. 2024b). However, the number statistics of AGN with well-constrained host properties remain small. Therefore, further exploration is needed to fully characterize the high-redshift AGN population, constrain BH seeding models, and trace the emergence of local scaling relations.

In addition to the large population of Type 1 AGN, first results from *JWST* spectroscopy have revealed populations of 'mini' or rapidly quenched low- to intermediate-mass ($M < 10^{10}$ $M_\odot$) galaxies (V. Strait et al. 2023; T. J. Looser et al. 2024; W. M. Baker et al. 2025e), alongside significant populations of the more massive ($M > 10^{10}$ $M_\odot$) traditionally quiescent systems (A. C. Carnall et al. 2024; F. D'Eugenio et al. 2024b; T. Nanayakkara et al. 2024; M. Park et al. 2024; W. M. Baker et al. 2025b, d). The high-z massive quiescent galaxies are often found to host AGN (A. C. Carnall et al. 2023; F. D'Eugenio et al. 2024b; W. M. Baker et al. 2025d; L. Bugiani et al. 2025) with an AGN fraction of $\gtrsim 45$ per cent (W. M. Baker et al. 2025d) and frequently hosting outflows likely requiring AGN feedback to explain (S. Belli et al. 2024; F. Valentino et al. 2025). It remains an open question as to the potential for AGN feedback to quench the lower mass, $M \sim 10^9$ $M_\odot$, systems at $z > 4$ with none to date showing signs of current AGN activity (however, any AGN quenching episode could have occurred prior to observation, with typical quenching lookback times of 10–30 Myr in rapidly quenched galaxies, T. J. Looser et al. 2024; W. M. Baker et al. 2025e). These results suggest that AGN feedback is likely to be a crucial component for understanding high-z galaxy quenching, at least at the most massive end (C. d. P. Lagos et al. 2025; W. M. Baker et al. 2025a). Additionally, further investigation into the frequency, scope, and properties of AGN in lower mass galaxies is urgently needed.

An additional problem complicating the studies of AGN at the current redshift frontier is the difficulty of selecting Type 2 AGN, which are thought to comprise the majority of AGN population (E. Lusso et al. 2013). Standard narrow emission-line diagnostics, such as the BPT diagram (J. A. Baldwin, M. M. Phillips & R. Terlevich 1981), tend to struggle at higher redshifts due to the sensitivity of their lines to metallicity (see H. Übler et al. 2023), which is considerably lower in the young Universe (D. Masters et al. 2014; A. L. Coil et al. 2015). While several alternative narrow-line diagnostic diagrams have been proposed (M. Shirazi & J. Brinchmann 2012; A. Feltre, S. Charlot & J. Gutkin 2016; K. Nakajima et al. 2023; J. Scholtz et al. 2023; G. Mazzolari et al. 2024b), larger samples of robustly confirmed AGN are instrumental to testing their validity and capabilities in providing a pure and complete sample of Type 2 AGN. As Type 1 AGN are selected through a direct detection of the BLR, a large sample of such objects would provide a robust benchmark in validating high-redshift Type 2 diagnostics.

In this paper, we present a solid sample of 34 broad-line AGN at $1.5 < z < 9$, from which 20 are newly discovered, obtained from the data collected across the entirety of the JWST Advanced Deep Extragalactic Survey (JADES) spectroscopic survey data (A. J. Bunker, NIRSPEC Instrument Science Team & JAESs Collaboration 2020; M. Rieke 2020; D. J. Eisenstein et al. 2023). These observations offer considerable depth and a range in spectral resolution allowing for robust constraints of BLR and narrow-line region (NLR) properties for Type 1 AGN down to $L_{bol} \sim 10^{43}$ erg s^{-1}. Deep imaging, accompanying the JADES spectroscopy (F. D'Eugenio et al. 2024a), allows for detailed investigations into the properties of galaxies hosting faint AGN in the early Universe. Additionally, the redshift range probed by our sample enables us to probe the redshift evolution of AGN and their host properties, tracing the emergence of local scaling relations. We will also show how the narrow-line emission properties displayed by our sample AGN imply the likely presence of a Type 2 population indistinguishable from star-forming galaxies by current diagnostics.

The paper is organized as follows – in Section 2 we introduce the JADES survey, its photometric and spectroscopic data used in our analysis. Section 3 describes our methods for selecting broad-line AGN and Section 4 lays out our methods of estimating their BH masses and accretion rates. Section 5 describes our methods of constraining the host properties of our sample BHs. The BH–host scaling relations of our sample, together with host morphologies, are discussed in Section 6. Section 7 describes spectral stacking of our sample sources and assesses the viability of searching for Type 2 AGN via narrow-line diagnostics. In Section 8 we present an initial exploration into the shapes of the broad lines of our sources and rule out scattering scenarios that would imply ~ 2 dex overestimation of BH masses. The contribution of

Type 1 AGN hosts to the high-redshift UV Luminosity Function is discussed in Section 9. Lastly, Section 10 provides summary and conclusions.

Throughout this work we assume a flat Lambda cold dark matter cosmology with $\Omega_\mathrm{m} = 0.315$ and $H_0 = 67.4\ \mathrm{km\,s^{-1}\,Mpc^{-1}}$ (Planck Collaboration VI 2020). All reported magnitudes are in the AB system.

2 DATA DESCRIPTION

The data used in this study have been obtained as part of the first 3 yr of the JADES survey. This survey consists of deep *JWST* imaging and spectroscopy in GOODS-N and GOODS-S fields. The full description of the survey can be found in D. J. Eisenstein et al. (2023); however, a summary will be provided here to add necessary context.

The JADES photometry largely consists of near-infrared (NIRCam) imaging utilizing the seven of the wide (*F*090*W*, *F*115*W*, *F*150*W*, *F*200*W*, *F*277*W*, *F*356*W*, and *F*444*W*) together with two medium (*F*335*M* and *F*410*M*) filters. The imaging consists of three tiers – Medium, covering 175 arcmin^2, Deep – covering 36 arcmin^2, and Deepest – produced by overlapping Deep pointings and covering a 9 arcmin^2 area. The total area covered by JADES imaging, excluding overlap, is thus of order 220 arcmin^2. In terms of depth, the limiting AB magnitude of the Medium pointings is 28.6 to 29.0, depending on the filter. Deep pointings range from 29.75 to 30.14, while Deepest from 30.02 to 30.52.

The photometric data were reduced according to procedure presented in B. E. Robertson et al. (2023), S. Tacchella et al. (2023), and W. M. Baker et al. (2025c). In summary, v1.9.2 of the *JWST* calibration pipeline (H. Bushouse et al. 2022) was used together with the CRDS pipeline mapping context 1039. Stages 1 and 2 of the pipeline, meant for applying the detector corrections and flat-fielding, respectively, were run with JADES' own sky-flat provided for the flat-fielding, otherwise keeping to the default parameters. After Stage 2, custom procedures were performed to account for $1/f$ noise and subtract scattered light artefacts, 'wisps', along with the large-scale background. Astrometric alignment was performed using a custom version of *JWST* `TweakReg`,[1] with corrections derived from *Hubble Space Telescope* (*HST*) *F*814*W* and *F*160*W* mosaics along with *Gaia* Early Data Release 3 astrometry. The images of individual exposures were then stacked in Stage 3 of the pipeline with the final pixel scale being 0.03 arcsec per pixel.

The spectroscopic part of the survey consists of several tiers, characterized by their depth, 'Medium' or 'Deep' along with photometry from which targets were selected, *HST* for targets selected with the *HST* or *JWST* for Webb-selected objects (PIDs 1210, 1287, 1286, 1181, and 1180, PIs Eisenstain and Luetzgendorf). The first two data releases were presented in A. J. Bunker et al. (2024) and F. D'Eugenio et al. (2024a) with the entire data set to be presented in the upcoming Data Release 4. The NIRSpec dispersers used in the survey were prism, the R1000, and G395H/F290LP (R2700) gratings. However, the high-resolution, R2700, grating had less coverage than prism and R1000; we thus used them for sample selection, while employing R2700 data for more accurate kinematics measurements for sources where it was available.

Table 1. A summary of grating/filter configurations for the R1000 and R2700 dispersers of NIRSpec.

Disperser + Filter	Nominal wavelength range (μm)
G140M/F070LP	0.70–1.27[a]
G235M/F170LP	1.66–3.07
G395M/F290LP	2.87–5.10
G395H/F290LP	2.87–5.14

[a] The data processing pipeline employed by JADES recovers G140M/F070LP spectra beyond the nominal wavelength range, see text for details.

The medium-resolution grating (R1000) consists of three individual gratings – G140M, G235M, and G395M that can be used with four separate filters – *F*070*LP*, *F*100*LP*, *F*170*LP*, and *F*290*LP*. The available combinations of these used by JADES are presented in Table 1.

Despite not using the G140M/100LP configuration, the survey data do access the 1.27–1.66 μm range as F070LP retains data beyond the nominal cut-off at the cost of it overlapping with lower orders of dispersion. The data reduction pipeline employed by JADES is able to disentangle the different orders and give access to the full range of wavelengths covered by F070LP. The precise exposure time for each disperser is tier dependent with the *HST*/Medium tiers receiving a nominal 1.7 h of exposure per source in the prism and 0.8 h per source in each of the medium gratings; *JWST*/Medium tiers had 2.6 h of exposure in each configuration. The deep tiers had 7 h exposures in R1000 gratings and 28 h in prism. It should be noted that not all objects within a tier received the same exposure hours. In some cases the exposure time was one-third to two-thirds of the nominal as the source ended up in fewer dithers, while in others the exposure times were longer due to sources ending up in multiple pointings. The exposure times for each individual source are listed in JADES Data Release 3 (DR3) catalogue (F. D'Eugenio et al. 2024a). In addition to the main Medium/Deep tiers an additional 'Ultra Deep' set of observations was carried out in GOODS-S as part of a GO 'Large Programme' (PID:3215, PIs Eisenstein and Maiolino) consisting of 7 to 47 h exposures for prism and G395M/F290LP, G140M/F070LP configurations of R1000, the G235M/F170LP being unused. Complementing the R1000 and prism, some tiers also made use of the high-resolution grating G395H, with resolution $R = 2700$. However, the R2700's high resolution can reduce the S/N of broad wings and the spectra may end up truncated on the red side, thus this grating has relatively little coverage in the survey. In total, the survey contains spectra of $\sim$5000 objects across the GOODS-N and GOODS-S fields spanning redshifts from 0.6 to 14. However, not all observed spectra were of high enough quality for emission-line analysis. The quality of the spectra, determined through visual inspection, is quantified via a flagging system, see table 6 in F. D'Eugenio et al. (2024a) for a summary. We thus exclude spectra that do not contain flags 6 or 7, implying no detected emission lines, or contain flags 2 or 10, signifying tentative redshifts or corrupted grating data, from further analysis. This produces an effective parent sample of $\sim$2500 sources.

The NIRSpec data were processed according to procedures laid out in A. J. Bunker et al. (2023) and other similar JADES papers, such as S. Carniani et al. (2023). A full description of the data reduction procedure will be presented in Carniani et al. (in preparation); in summary the spectral data were reduced using the pipeline developed by the NIRSpec GTO team and the ESA NIRSpec Science Operations Team. The first stage of this pipeline

---

[1] https://drizzlepac.readthedocs.io/en/deployment/tweakreg.html

involved removing cosmic rays and snowball artefacts and the second stage was where background subtraction was performed. Afterwards 2D cut-outs of each spectrum were generated and optics corrections performed. Path-loss corrections were calculated for each observation, taking into account the intra-shutter position, assuming a point-source geometry and a 5-pixels extraction box (i.e. the full shutter height). Due the compact nature of the objects, to maximize the S/N, complementary 3-pixel extractions were used for broad-line detection. Even though a 3-pixel box is not the extraction box the path-loss corrections were optimized for, when compared, the two extractions do not appear to have significant differences in the measured line fluxes. The 5 pixel extractions were utilized in constraining the host properties from the spectra. As a final step, the extracted individual exposures are stacked using a weighted sum and sigma-clipped to remove outlier regions resulting from residual bad pixels or cosmic rays. It should be noted that the sigma clipping procedure employed by the pipeline can erroneously remove bright spectral features, thus the final product contains two stacks – one with sigma clipping, the other without. Generally, we use the sigma clipped data in our analysis as the unclipped data contain more detector artefacts. However, in some cases sigma clipping may erroneously remove the tops of bright and narrow emission lines. This does not affect the broad-line selection; however, it can cause issues constraining fluxes and shapes of emission lines. Fortunately, only one source in our final AGN sample, GN-28074, is affected by sigma clipping in this manner. For this source, we substitute the sigma clipped lines with those from the unclipped data, see I. Juodžbalis et al. (2024a) for details.

3 SPECTRAL FITTING AND SAMPLE SELECTION

The core method used to search for AGN in this study is emission-line decomposition into multiple Gaussian components, following the methodology of R. Maiolino et al. (2024). This is done to separate the narrow-line emission, coming from low-density gas ionized by either star formation or AGN activity, from the broad components indicating the presence of high-velocity gas characteristic of the BLRs surrounding an accreting BH. The main emission line chosen for the analysis was the Hα line as this emission feature tends to be bright, only weakly absorbed by neutral hydrogen and, owing to its rest-frame wavelength of $\lambda = 6563$ Å, detectable by *JWST* between $z = 0.5$ and $z = 7.0$ allowing for self-consistent probing of the AGN population in the low- and high-redshift regimes. Additionally, results by R. Abuter et al. (2024) have shown that, while single epoch virial estimators can significantly overestimate BH masses, this bias is smallest for Hα , for which it is consistent with the scatter on the relation. This is similar to the methodology adopted in R. Maiolino et al. (2024), who have conducted a search for Type 1 AGN across the first set of JADES tiers. Our work expands these methods across the full breadth of the JADES survey and benefits from an improved data reduction pipeline.

The procedure used to identify broad Hα line emission consisted of initially fitting two distinct models (with outflow fitting in the [O III] carried out at a later stage) to each R1000 spectrum. The first model contained just the narrow-line emission from the Hα line and the [N II]$\lambda\lambda$6550,6585 doublet. The narrow lines were constrained to have the same widths and the same systemic velocity. The ratio between the peaks of the [N II] lines was constrained to 3 as it is set by the atomic physics and insensitive to density and temperature (I. Dojčinović, J. Kovačević-Dojčinović & L. Č. Popović 2023). The second model then simply contained an additional broad-line component of Hα added on top of the narrow lines. The kinematics of broad Hα was allowed to vary with respect to the narrow lines. Fitting the two models was carried out using Bayesian methods with mostly uniform priors on the line peak height and full width at half-maximum (FWHM), with the latter allowed to vary between 100 and 800 km s^{-1} for the narrow and 800 to 10 000 km s^{-1} for the broad lines. The prior on line centroid velocities was Gaussian, centred on the measured redshift of the source, with a standard deviation of about 400 km s^{-1}. The posterior distributions were then estimated from the priors and the data using a Markov Chain Monte Carlo integrator (D. Foreman-Mackey et al. 2013). The relative performance of the two models was quantified using the Bayesian information criterion (BIC):

$$BIC = \chi^2 + k \ln n, \quad (1)$$

where χ^2 is the chi-square of the fit, k the number of model parameters, and n the number of data points. The difference in BIC between the narrow-line-only model and the model containing the broad line was then computed as $\Delta BIC = BIC_{\rm Narrow} - BIC_{\rm Narrow+Broad}$. The lower floor for accepting the BLR model was $\Delta BIC > 5$. In addition, the broad component was required to have a signal-to-noise ratio[2] of at least 5 (Fig. C1 shows the distribution of the entire parent sample in terms of these selection values). We have also inspected and removed sources for which the significance was driven by 1–2 pixels as those were likely artefacts of correlated NIRSpec uncertainties (B. Dorner 2012). This makes our selection conservative and ensures that only solid detections are included in the main sample. The ΔBIC criterion adopted here is a bit looser than $\Delta BIC > 10$ required by R. Maiolino et al. (2024); however, only three out of 30 sources in the main sample have $\Delta BIC < 10$, hence our conclusions are robust against variations in selection criteria.

An additional complication in measuring intrinsic line kinematics from a given fit is the instrumental broadening effect encapsulated in a line spread function (LSF). Any spectrum observed in a detector is a convolution between the object's intrinsic spectrum and the LSF. However, this LSF can be readily approximated as a Gaussian profile of some FWHM. Therefore, the deconvolution of measured quantities can be performed algebraically, via $\mathrm{FWHM_{int}} = \sqrt{\mathrm{FWHM_{meas}}^2 - \mathrm{FWHM_{LSF}}^2}$ relation, where FWHM$_{\rm meas}$ and FWHM$_{\rm LSF}$ are the measured and instrumental FWHM respectively. The full description of the *JWST* LSF for NIRSpec-MSA observations is presented in A. Graaff et al. (2024); however, the LSF corrections were negligible for the broad lines of our AGN as they were > 10 times wider than FWHM$_{\rm LSF}$.

In addition to the Hα line we also fit the [O III]$\lambda\lambda$4959,5007 doublet together with Hβ in order to constrain the presence of ionized outflows, to disentangle BLR components from outflows, and also to derive dust attenuation utilizing the Balmer decrement. The outflow component fitted to the [O III] doublet used a flat FWHM prior constrained to between 600 and 2500 km s^{-1}. In cases where the outflow contribution was found to be significant, utilizing the same significance tests as with broad Hα detection, we refit the Hα with an added outflow component, utilizing an informative Gaussian prior constrained by the fits to

---

[2] We define S/N as the ratio of the total line flux integrated over the FWHM to the quadrature-combined error in the same range.

the [O III] lines, in order to reassess the significance of the BLR. The rationale of this step is that a BLR component does not have a counterpart in [O III], hence broad wings in Hα that are not seen in [O III] cannot be ascribed to outflows but to a BLR component. In the case of GN-200679, the spectrum lacked R1000 coverage of [O III], thus we consider this source a tentative Type 1 AGN as the possibility that the broad Hα profile is an outflow could not be discounted. In addition, we find that, after accounting for outflows, the fitted BLR component for GN-23924 is heavily subdominant, despite remaining formally significant and passing visual inspection. We thus conservatively mark this object as tentative. Overall, four sources in our sample have significant outflow detections. The fits to [O III] lines of the targets that were not published before are shown in Fig. D1.

We also note that after a careful inspection of the single-Gaussian BLR fit residuals two of our sample sources (GS-49729 and GS-159717) presented significant broad wings of the broad-line profile, not reproduced by a single Gaussian fit. We refit these sources with a 2-Gaussian BLR model, constraining one Gaussian to be narrower than the other and find that such a fit reproduces the BLR shape considerably better (Figs A2 and A3), while such a double-Gaussian structure may be indicative of merging BHs with separate BLRs, as discussed in R. Maiolino et al. (2024), the two components being located at the same systematic velocity suggests that both profiles originate from the same BLR and the double-Gaussian nature is due to intrinsic non-Gaussianity found in the BLR of some AGN (W. Kollatschny & M. Zetzl 2013). We thus treat both Gaussian components as modelling the same line profile and re-estimate the broad Hα luminosity and FWHM from the combined profile. The presence of merging BHs in our sample is still a possibility, as confirmed BH mergers do sometimes exhibit matching systemic velocities of the broad lines (P. R. Capelo et al. 2017). However, access to high-resolution IFU data is required for a robust survey of BH mergers in our sample AGN.

In addition to non-Gaussian features, two of our sample sources (GN-28074 and GS-159717) presented clear evidence of absorption features in their broad lines. The implications of these features are explored in depth in I. Juodžbalis et al. (2024a) and F. D'Eugenio et al. (2025b). In this work, we simply account for their presence by modelling them with a Gaussian optical depth distribution:

$$\tau_\lambda = \tau_0 \exp\left[-0.5\left(\frac{\lambda - \lambda_0 e^{\Delta v/c}}{\sigma}\right)^2\right], \qquad (2)$$

where τ_0 is the optical depth at the core of the line, Δv the velocity shift of the absorber, and σ its velocity dispersion, coupled with a standard attenuation model:

$$f_\lambda = 1 - C_f + C_f e^{-\tau_\lambda}, \qquad (3)$$

where C_f is the covering fraction of the absorbing medium.

3.1 Comparison with previous AGN samples in JADES

The previous procedure has yielded 28 robust and two tentative broad-line AGN sources spanning redshifts from 1.7 to 7 (Table 2), out of which 11 overlap with the R. Maiolino et al. (2024) sample as it originates from earlier JADES data. We do not recover all 12 BLR presented in R. Maiolino et al. (2024) as one of their tentative sources (ID-3608) does not pass our BIC criterion. In addition, one of our objects (GS-204851) has been identified as a tentative AGN candidate in J. Matthee et al. (2024), as GOODS-S-13971. Our higher signal-to-noise data allow to robustly confirm the aforementioned object as an AGN. Recent work by V. Kokorev et al. (2024) has identified a candidate broad-line AGN in a quenched galaxy from JADES DR3 spectroscopy (F. D'Eugenio et al. 2024a). While this source is in our parent catalogue, our fits fail to detect a significant broad component with $\Delta BIC < 5$; we thus do not include this source in our sample. This galaxy is included as ID 72 127 within the quiescent galaxy sample of W. M. Baker et al. (2025d). The BHs apparently following the local scaling relations recently reported by J. Li, Y. Shen & M.-Y. Zhuang (2025b) likewise do not pass our BIC and S/N selection criteria. Finally, we note that two additional objects (GN-38509 and GN-28074) have been identified as particularly interesting and published separately from the main sample (I. Juodžbalis et al. 2024a, b). Therefore, our full sample of 30 Type 1 AGN contains 16 new sources. Recent work by K. N. Hainline et al. (2025), which searched for Little Red Dots (LRDs) among our sample of broad-line selected sources, has shown that up to 30 per cent of our sample sources could be classified as LRDs, a sub population of red AGN identified in previous *JWST* surveys (J. Matthee et al. 2024); however, the majority of our AGN do not fall into this category.

3.2 Tentative broad Hβ emitters

In addition to the main sample above, visual inspection of the prism spectra revealed four additional objects at $7 < z < 9$ that appeared to have a broad component in the Hβ line. Individually, these proved to be statistically insignificant; however, a stack of them, weighted by inverse root mean square (rms) error, revealed a significant broad Hβ component as shown in Appendix B. The full description of our stacking procedure is provided in Section 7, while here we summarize that the significance of the broad Hβ feature remains even when weighting by [O III]λ5007 luminosity. Additionally, we check through jackknife resampling that the significance is not driven by one particular object. We thus place these four objects in our sample, bringing the total to 34 AGN, with 20 of them being new discoveries.

The prism spectra of all objects together with fits to the Hα line are presented in Fig. 1 and Figs A1, A2 and A3 in Appendix A. We have also carried out a search for broad Hβ emitters across both R1000 and prism in order to push our upper redshift limit to $z = 9$; however, no significant sources were detected. The lower resolution and higher depth of prism means that it is significantly more sensitive to faint broad lines than R1000. Hence, we fitted all prism spectra available in order to look for more massive dormant BHs like GN-38509 (I. Juodžbalis et al. 2024b); however, no additional BLR candidates were uncovered that were not already selected by our fits to R1000.

4 CONSTRAINING BH PROPERTIES

We utilize our fits to the BLR emission to constrain the BH mass using single-epoch virial relations. Recent results by R. Abuter et al. (2024) measured the BLR size via interferometric data, and have put into question the usage of BH virial relations using transitions such as C IV, Mg II , or Hβ (H. Netzer et al. 2007; C. A. Negrete et al. 2012); however, their finding that the discrepancy is reduced to only a factor 2.5 when using the Hα line is reassuring, as this is within the 0.3 dex calibration uncertainties; this is verified further by C. Bertemes et al. (2025) testing of different BH mass constraints for a bright QSO. Furthermore, the deviations are associated with super-Eddington accretion influencing the

Table 2. Summary of the key derived AGN properties for all objects in our catalogue. The first column provides the catalogue ID, the second and third their coordinates. Column four gives the best-fitting redshift estimates, with uncertainties of order 0.001. The following columns list the main properties of the BLR – the BH mass in Solar masses (with the uncertainties including the 0.3 dex scatter on equation 4), bolometric luminosity in erg s^{-1}, and the Eddington ratio. Columns eight and nine give the observed ratio of narrow Hα and Hβ lines and the derived A$_V$, respectively. An A$_V$ of 0 is listed for sources with negative A$_V$ values that were consistent with 0. A dash in a column indicates that the value could not be measured due to the relevant lines falling in a detector gap or outside the NIRSpec coverage. The final column contains the literature reference for previously published sources [1. R. Maiolino et al. (2024), 2. J. Matthee et al. (2024), 3. I. Juodžbalis et al. (2024b), 4. I. Juodžbalis et al. (2024a)]. The observed Balmer decrement for the narrow lines of GS-209777 (marked with '$*$') was steeper than that of the broad lines; we thus use the uncorrected estimates for this source. Objects marked with the dagger symbol had line profiles more complex than a simple Gaussian. Further analysis of these is given in Section 8 with different BH mass estimates presented in Table 7.

Object ID	RA	Dec.	z	$\log M_{BH}/\mathrm{M}_\odot$	$\log L_{bol}/(\mathrm{erg\ s^{-1}})$	λ_{Edd}	$\mathrm{F}_{H\alpha;\ nr}/\mathrm{F}_{H\beta;\ nr}$	A$_V$	Ref.
Robust									
GS-30148179	53.14208	−27.77985	5.922	$7.12^{+0.34}_{-0.35}$	$44.25^{+0.06}_{-0.08}$	$0.11^{+0.05}_{-0.03}$	$2.52^{+0.18}_{-0.19}$	0	–
GS-10013704	53.12654	−27.81809	5.919	$7.44^{+0.31}_{-0.31}$	$44.29^{+0.02}_{-0.02}$	$0.055^{+0.007}_{-0.006}$	$2.55^{+0.20}_{-0.16}$	0	1.
GS-210600	53.16611	−27.77985	6.306	$7.41^{+0.33}_{-0.34}$	$44.29^{+0.09}_{-0.11}$	$0.057^{+0.016}_{-0.013}$	$2.99^{+0.22}_{-0.25}$	$0.12^{+0.19}_{-0.23}$	–
GS-209777	53.15847	−27.77405	3.709	$8.90^{+0.30}_{-0.30}$	$45.42^{+0.01}_{-0.01}$	$0.027^{+0.001}_{-0.001}$	$7.26^{+2.52}_{-1.63}*$	$2.59^{+0.83}_{-0.70}*$	–
GS-204851†	53.13859	−27.79025	5.480	$7.68^{+0.32}_{-0.31}$	$44.97^{+0.17}_{-0.12}$	$0.16^{+0.03}_{-0.02}$	$2.95^{+0.44}_{-0.28}$	$0.08^{+0.38}_{-0.28}$	2.
GS-179198	53.08898	−27.86069	3.830	$7.23^{+1.42}_{-0.33}$	$43.92^{+4.46}_{-0.08}$	$0.04^{+9.44}_{-0.01}$	$3.61^{+136.0}_{-0.16}$	$0.62^{+9.8}_{-0.12}$	–
GS-172975	53.08773	−27.87124	4.741	$7.25^{+0.32}_{-0.32}$	$44.07^{+0.04}_{-0.04}$	$0.05^{+0.01}_{-0.01}$	$2.50^{+0.65}_{-0.40}$	0	–
GS-159717†	53.09753	−27.90126	5.077	$7.44^{+0.30}_{-0.30}$	$45.13^{+0.008}_{-0.008}$	$0.38^{+0.04}_{-0.04}$	$2.77^{+0.61}_{-0.38}$	0.	–
GS-159438	53.05447	−27.90246	3.239	$6.47^{+0.32}_{-0.31}$	$44.11^{+0.03}_{-0.04}$	$0.35^{+0.05}_{-0.08}$	$3.18^{+0.08}_{-0.07}$	$0.28^{+0.07}_{-0.06}$	–
GN-77652	189.29323	62.19900	5.229	$6.62^{+0.34}_{-0.32}$	$44.11^{+0.04}_{-0.05}$	$0.24^{+0.09}_{-0.08}$	$2.62^{+1.45}_{-0.53}$	0	1.
GN-73488†	189.19740	62.17723	4.133	$7.83^{+0.30}_{-0.30}$	$45.22^{+0.07}_{-0.05}$	$0.20^{+0.01}_{-0.01}$	$5.34^{+0.33}_{-0.24}$	$1.68^{+0.16}_{-0.12}$	1.
GN-62309	189.24898	62.21835	5.172	$6.29^{+0.36}_{-0.33}$	$43.56^{+0.13}_{-0.12}$	$0.15^{+0.05}_{-0.05}$	$2.95^{+0.33}_{-0.26}$	$0.08^{+0.28}_{-0.24}$	1.
GN-61888	189.16802	62.21701	5.874	$7.04^{+0.33}_{-0.32}$	$44.38^{+0.09}_{-0.07}$	$0.18^{+0.05}_{-0.03}$	$3.60^{+0.43}_{-0.31}$	$0.62^{+0.30}_{-0.24}$	1.
GN-53757	189.26978	62.19421	4.447	$7.33^{+0.31}_{-0.31}$	$44.29^{+0.02}_{-0.02}$	$0.07^{+0.01}_{-0.009}$	$2.63^{+0.42}_{-0.34}$	0	1.
GS-49729†	53.17850	−27.78411	3.189	$7.67^{+0.30}_{-0.30}$	$44.83^{+0.02}_{-0.02}$	$0.115^{+0.005}_{-0.004}$	–	–	–
GS-38562†	53.13586	−27.87165	4.822	$7.51^{+0.30}_{-0.31}$	$44.70^{+0.06}_{-0.06}$	$0.12^{+0.01}_{-0.01}$	$3.23^{+0.22}_{-0.21}$	$0.32^{+0.18}_{-0.19}$	–
GN-38509	189.09144	62.22811	6.678	$8.57^{+0.37}_{-0.38}$	$44.84^{+0.14}_{-0.14}$	$0.015^{+0.008}_{-0.005}$	$5.51^{+0.86}_{-0.69}$	$1.74^{+0.38}_{-0.37}$	3.
GN-29648	189.20920	62.26427	2.960	$6.81^{+0.39}_{-0.35}$	$43.90^{+0.08}_{-0.06}$	$0.11^{+0.12}_{-0.03}$	$4.51^{+0.26}_{-0.16}$	$1.22^{+0.15}_{-0.10}$	–
GN-28074†	189.06457	62.27382	2.259	$8.55^{+0.30}_{-0.30}$	$45.76^{+0.02}_{-0.02}$	$0.129^{+0.004}_{-0.003}$	$4.14^{+0.16}_{-0.14}$	$1.78^{+0.07}_{-0.06}$	4.
GN-20621	189.12252	62.29285	4.682	$7.05^{+0.35}_{-0.34}$	$44.17^{+0.16}_{-0.13}$	$0.11^{+0.05}_{-0.03}$	$3.44^{+0.72}_{-0.50}$	$0.50^{+0.50}_{-0.42}$	1.
GS-17341	53.08727	−27.72962	3.598	$6.76^{+0.38}_{-0.37}$	$44.01^{+0.16}_{-0.12}$	$0.15^{+0.09}_{-0.05}$	$4.00^{+0.93}_{-0.61}$	$0.90^{+0.56}_{-0.45}$	–
GS-13329	53.13904	−27.78443	3.936	$6.86^{+0.34}_{-0.37}$	$44.11^{+0.09}_{-0.10}$	$0.14^{+0.06}_{-0.03}$	$3.37^{+0.42}_{-0.40}$	$0.44^{+0.31}_{-0.34}$	–
GN-11836	189.22059	62.26368	4.409	$6.06^{+0.32}_{-0.32}$	$44.11^{+0.05}_{-0.05}$	$0.11^{+0.03}_{-0.02}$	$3.62^{+0.12}_{-0.11}$	$0.63^{+0.09}_{-0.08}$	1.
GS-9598	53.16181	−27.77072	3.324	$6.48^{+0.45}_{-0.35}$	$43.85^{+0.09}_{-0.11}$	$0.18^{+0.09}_{-0.08}$	$3.37^{+0.42}_{-0.40}$	$1.01^{+0.16}_{-0.16}$	–
GS-8083	53.13284	−27.80186	4.753	$7.10^{+0.31}_{-0.31}$	$44.03^{+0.04}_{-0.04}$	$0.07^{+0.01}_{-0.009}$	$3.12^{+0.25}_{-0.23}$	$0.23^{+0.11}_{-0.11}$	1.
GN-2916	189.10774	62.26952	3.664	$7.05^{+0.44}_{-0.43}$	$43.91^{+0.13}_{-0.14}$	$0.06^{+0.07}_{-0.03}$	$2.89^{+0.33}_{-0.31}$	$0.03^{+0.29}_{-0.31}$	–
GN-1093	189.17974	62.22463	5.594	$7.14^{+0.34}_{-0.33}$	$44.32^{+0.13}_{-0.11}$	$0.12^{+0.04}_{-0.03}$	$4.86^{+0.80}_{-0.59}$	$1.43^{+0.41}_{-0.35}$	1.
GN-954	189.15197	62.25964	6.759	$7.70^{+0.31}_{-0.32}$	$45.17^{+0.15}_{-0.17}$	$0.23^{+0.03}_{-0.04}$	$3.44^{+0.44}_{-0.46}$	$0.49^{+0.32}_{-0.39}$	1.
Tentative									
GS-200679	53.11392	−27.80620	4.547	$6.19^{+0.60}_{-0.30}$	$43.63^{+0.09}_{-0.39}$	$0.23^{+0.02}_{-0.19}$	–	–	–
GN-23924	189.03205	62.25089	1.676	$7.22^{+0.32}_{-0.33}$	$43.61^{+0.10}_{-0.11}$	$0.020^{+0.010}_{-0.007}$	$4.17^{+0.25}_{-0.23}$	$0.25^{+0.13}_{-0.13}$	–
Tentative Hβ									
GS-20057765	53.04080	−27.85901	8.913	$7.33^{+0.62}_{-0.70}$	$44.16^{+0.19}_{-0.30}$	$0.051^{+0.090}_{-0.036}$	–	–	–
GS-20030333	53.05373	−27.87789	7.891	$7.42^{+0.65}_{-0.48}$	$44.44^{+0.11}_{-0.14}$	$0.08^{+0.078}_{-0.056}$	–	–	–
GS-164055	53.08168	−27.88857	7.397	$7.63^{+0.59}_{-0.66}$	$44.21^{+0.16}_{-0.21}$	$0.03^{+0.048}_{-0.020}$	–	–	–
GN-4685	189.09629	62.23914	7.415	$7.36^{+0.45}_{-0.42}$	$44.13^{+0.10}_{-0.12}$	$0.045^{+0.020}_{-0.020}$	–	–	–

size of the BLR, while most of our sample is likely in a sub-Eddington regime. We thus obtain our BH masses via the virial relation (A. E. Reines & M. Volonteri 2015):

$$\log\frac{M_{\mathrm{BH}}}{\mathrm{M}_\odot} = 6.60 + 0.47\log\left(\frac{L_{H\alpha}}{10^{42}\ \mathrm{erg\,s^{-1}}}\right) + 2.06\log\left(\frac{\mathrm{FWHM}_{H\alpha}}{1000\ \mathrm{km\,s^{-1}}}\right), \tag{4}$$

where $L_{H\alpha}$ is the luminosity of the broad Hα line and FWHM$_{H\alpha}$ its width. We estimate the bolometric luminosities of our AGN following the calibrations of J. Stern & A. Laor (2012), which give $L_{bol} = 130 L_{H\alpha}$.

Estimating the extinction correction to the BLR is not trivial even when a broad component in both Hβ and Hα lines is seen, as the intrinsic Balmer decrement can be significantly steeper than the case B scenario, due to collisional excitation enhancing Hα relative to Hβ, and can potentially reach values up to 10 (D.

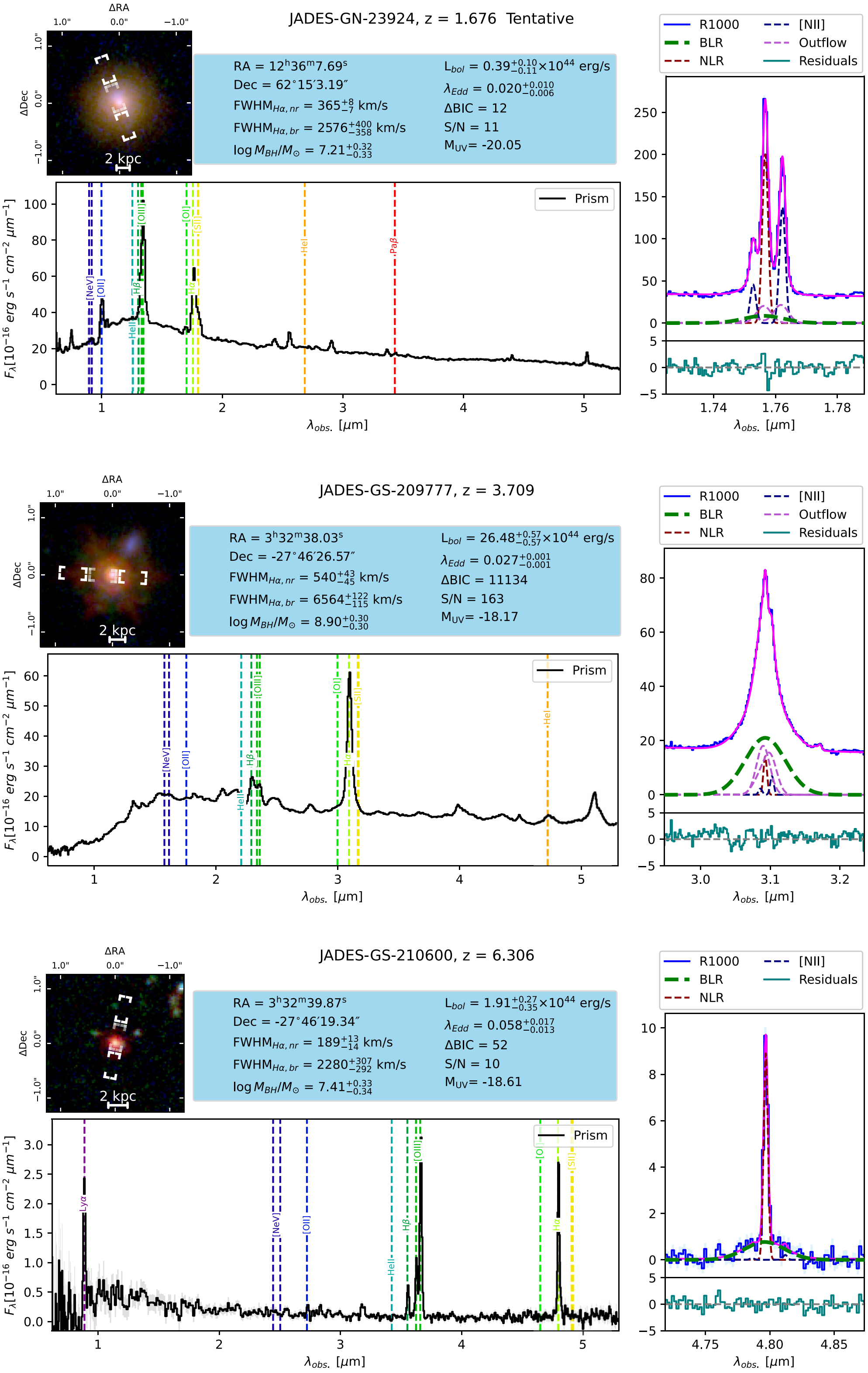

Figure 1. Fits of objects representative of our sample sources across the redshift range. Each figure showcases the RGB NIRCam stamps at the top together with the plotted MSA slit position. The stamps are made with *F090W*, *F200W*, and *F400W* as blue, green, and red channels, respectively. The prism spectrum is shown in the bottom left and the fits to the Hα line region in R1000 together with the corresponding residuals are located in the bottom right; the solid magenta curve shows the best fit to the Hα line profile. Quantities derived from R1000 fitting are shown in the blue box. Top: the lowest redshift ($z = 1.676$) source of our sample, located in a massive elliptical host with a clear stellar continuum and a Balmer break. This object has been marked as tentative due to the presence of [O III] outflows. Middle: a massive $z = 3.709$ QSO with a red optical continuum and Hα emission dominated by BLR and outflows with very weak narrow lines. Bottom: one of the highest redshift sources in our sample ($z = 6.306$), a low-luminosity AGN.

Ilić et al. 2012). In our analysis, we measure the A_V utilizing fluxes of the narrow Hβ and Hα lines and assume a standard case B decrement of 2.86 for the narrow lines along with the SMC extinction curve (K. D. Gordon et al. 2003). We use the same A_V values to correct the BLR emission, assuming that the host's ISM is the dominant contributor to the extinction there (R. Gilli et al. 2022).

The BH properties for the four sources with tentative broad Hβ detections were estimated using the Hβ based mass scaling relation from M. Vestergaard & B. M. Peterson (2006):

$$\log \frac{M_{\rm BH}}{\rm M_\odot} = 6.67 + 0.63 \log\left(\frac{L_{H\beta}}{10^{42}\,{\rm erg\,s^{-1}}}\right) + 2\log\left(\frac{{\rm FWHM}_{H\beta}}{1000\,{\rm km\,s^{-1}}}\right). \quad (5)$$

Due to a lack of Hα coverage constraining the A_V, we assume $A_V = 0$ for these sources. While dust attenuation on average can be expected to decrease with increasing redshift (R. J. Zhao & S. R. Furlanetto 2024), this is not necessarily true for individual sources, thus the BH masses and luminosities may be somewhat underestimated for these objects.

For the bolometric luminosity estimates, we use the same Hα-based calibrations as for the main sample sources (J. Stern & A. Laor 2012), assuming a case B decrement. As the Balmer decrement in BLR is generally steeper than the case B value, our luminosity estimates, and consequently Eddington ratios, may be lower limits.

4.1 Properties of the final BH sample

Our final sample of accreting BHs and their hosts contains 34 sources with BH masses ranging from 10^6 to 10^9 M$_\odot$, with a mean $M_{\rm BH} \approx 10^{7.2}$ M$_\odot$, corresponding to the knee of the BH mass function at $z = 4$ (B. C. Kelly & A. Merloni 2012) and aligning with other BHs discovered with *JWST* from other studies (Fig. 2). Most of our sample sources (70 per cent) are located at $z > 4$ with a median redshift of 4.8. The L_{bol} of our sample sources ranges from $10^{43.5}$ to $10^{45.5}$ erg s^{-1}, with the majority concentrated at $\sim 10^{44}$ erg s^{-1}. Fig. 2 showcases the comparison of our sample to other *JWST* surveys (Y. Harikane et al. 2023; J. Matthee et al. 2024) as well as high-redshift QSOs (C. Mazzucchelli et al. 2023) in terms of L_{bol} and M_{BH}. As can be seen, our sample goes $\sim$ 1 dex fainter in luminosity than other *JWST* surveys. We thus provide a deep view into the low-mass low-luminosity regime of AGN activity that was completely inaccessible in the pre-*JWST* era as previous all-sky QSO surveys could only explore sources at $L_{bol} > 10^{47}$ erg s^{-1} and $M_{\rm BH} > 10^{8.5}$ M$_\odot$ – close to the upper BH mass range of our sample. As the upper BH mass bound ($M_{BH} \sim 10^9$ M$_\odot$) of our sample sources approaches the masses of typical $5 < z < 6$ QSOs, our observations have the potential to probe the 'post-QSO' regime of SMBH activity (i.e. faded QSO or 'dormant' BHs), as indeed illustrated by GN-38509 (I. Juodžbalis et al. 2024b). While detailed completeness simulations are beyond the scope of this work, we do explore our completeness in selecting Type 1 AGN from the parent sample using the approach presented in I. Juodžbalis et al. (2024b) consisting of injecting simulated broad profiles into NIRSpec data. The spectra simulated in I. Juodžbalis et al. (2024b) were redshifted to z=6–7; here, we extend the simulation down to $z = 4$. The median 50 per cent completeness limit for our sample selection is shown as a violet line in Fig. 2 and indicates that the sample is luminosity complete down to $L_{bol} = 10^{44}$ erg s^{-1}.

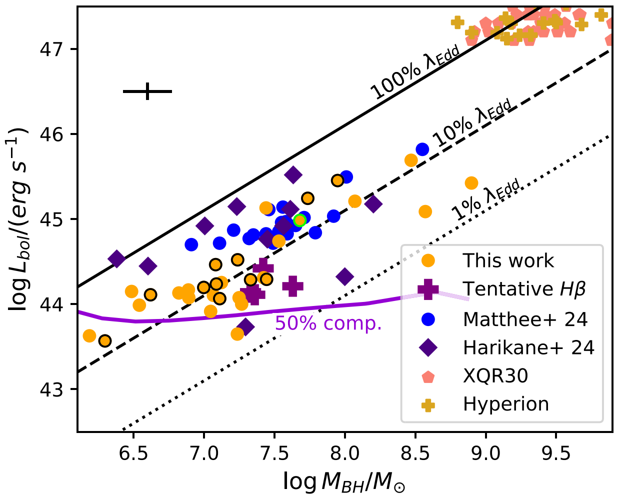

Figure 2. L_{bol}–M_{BH} diagram of our sample sources (orange points) compared to previous samples by Y. Harikane et al. (2023) and J. Matthee et al. (2024) (blue points and diamonds) as well as high-redshift QSOs from XQR30 and Hyperion, C. Mazzucchelli et al. (2023) and L. Zappacosta et al. (2023) (light red pentagons and yellow '+' respectively). Constant Eddington ratios are shown by black lines. The 50 per cent completeness boundary for our sample is shown as a solid violet line. The average error on each of our sample points is indicated by the black bars in the upper left. Sample sources previously published in R. Maiolino et al. (2024) are indicated by a black outline, while the source discovered by J. Matthee et al. (2024) is outlined in green. The apparent correlation between L_{bol} and M_{BH} is likely overstated in the plot as both axes depend on the Hα luminosity through the scaling relations.

5 CONSTRAINING HOST PROPERTIES

As a core goal of this paper is investigating the scaling relations between BHs and their host galaxies, we conduct an analysis of the properties of the galaxies hosting our sample AGN. We focus on inferring their stellar velocity dispersions (σ_*) and measuring stellar masses (M_*). In addition, many BHs found by *JWST* were discovered to be overmassive relative to the stellar masses of their hosts (Y. Harikane et al. 2023; H. Übler et al. 2023; L. J. Furtak et al. 2024; D. D. Kocevski et al. 2024; R. Maiolino et al. 2024), while remaining consistent with the local M_{BH}–σ_* relation (R. Maiolino et al. 2024). The enhanced statistics and redshift coverage afforded by our sample allows us to look for signs of redshift evolution of these scaling relations. We thus endeavour to robustly establish the host galaxy properties of our sample AGN.

5.1 Velocity dispersion

We measure the host galaxies' ionized gas velocity dispersions of our sources by fitting the nebular emission lines in the highest resolution data available (either R1000 or R2700) and using the FWHM of the narrow Hα or, if unavailable, narrow [O III] lines and applying the LSF correction. While the JADES survey has prism + R1000 coverage for all objects, only some tiers were observed in R2700 G395H/F290LP configuration. Additionally, since about two-thirds of the R2700 spectra are truncated to some degree (because the red part of the long R2700 possibly falling

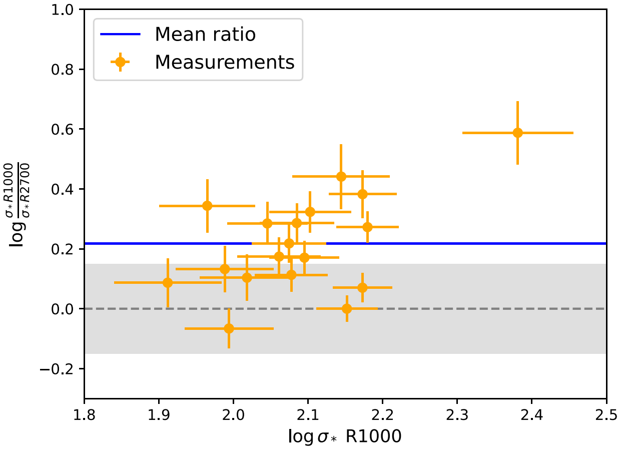

Figure 3. Comparison of inferred σ_* values, corrected for LSF, obtained by fitting the medium- and high-resolution emission-line spectra of ionized gas. The y-axis shows the inferred σ_* ratio, while the x-axis shows the σ_* inferred from R1000. The grey shaded region indicates the 0.3 dex scatter on the R. Bezanson et al. (2018) calibration relation. The mean ratio is indicated by the blue line and shows that R1000 data on average overestimates σ_* by about 80 per cent.

outside the detector, depending on the location on the MSA), many of the R2700 spectra do not have strong nebular lines in the available range. As a result, only 18 of our sources have R2700 coverage with strong nebular lines available for measuring the velocity dispersion. The stellar velocity dispersions were inferred from the measured ionized gas integrated line widths using the average gas-to-stellar measurements from R. Bezanson et al. (2018), assuming a scaling factor of 1.3. For the sources lacking R2700 coverage, we were forced to rely on the R1000 data. In order to assess and correct overestimation coming from using the R1000 data we perform a comparison of the inferred σ_* values given by both gratings. The comparison is shown in Fig. 3 and illustrates that, while R1000 measurements on average overestimate the σ_* value by around 0.26 dex with a standard deviation (STD) of 0.16 dex, around half of measurements are consistent within the ~0.15 dex scatter on the R. Bezanson et al. (2018) calibration. While Fig. 3 does appear to display a linear trend, the apparent correlation is largely driven by the outlying point at $\log \sigma_* = 2.4$. Based on these considerations, we adopt a constant correction factor of 0.26 dex and add the STD of this factor to the fit uncertainties in quadrature.

We note that σ_* could not be reliably measured for the tentative Hβ sources due to low S/N of the [O III] doublet and narrow Hβ in R1000, while the prism resolution of ~ 1000 km s^{-1} is inadequate for accurate narrow-line width measurements.

5.2 Stellar masses from spectroscopic decomposition

We use two different methods to derive stellar masses for our sources: fits to the NIRSpec prism spectra using BEAGLE, and fits to the NIRCam photometry using CIGALE. The comparison of the two methods indicates a scatter of 0.4 dex but no strong systematic disagreements. The two methods are described here.

We use a version of BEAGLE (J. Chevallard & S. Charlot 2016) to constrain host stellar masses from NIRSpec prism spectroscopy. The method used is similar to the one laid out in R. Maiolino et al. (2024) and we summarize the key features here. We fit the prism spectroscopy extracted from a 5 pixel aperture corrected assuming a point source spatial distribution. In cases where the source is clearly extended we instead use CIGALE to fit to the NIRCam photometry as described further in the text. The continuum from the AGN is modelled as a simple power law. We perform two fits to each source modelling the AGN component with a frequency power-law slope of −2.33 (N. I. Shakura & R. A. Sunyaev 1973) and −1.54 (D. E. Vanden Berk et al. 2001), with the level of dust attenuation of the power-law component allowed to vary freely and modelled by the SMC extinction law (Y. C. Pei 1992). The stellar component was modelled using the delayed exponential star formation history (SFH) with a 10 Myr starburst and a 300 M$_\odot$ IMF cut-off. This SFH allows the recent star formation rate to vary freely and independently from the past star formation, reducing the biases inherent in stricter parametric forms that tie together the current star formation to the integrated stellar mass. The dust attenuation of the stellar component was modelled with the S. Charlot & S. M. Fall (2000) attenuation curve. Before fitting, regions of the spectra containing strong emission lines were masked as BEAGLE does not contain models for BLR emission. Additionally to the fitting performed in R. Maiolino et al. (2024), the measured narrow Hα flux was used as an upper limit to the model Hα line flux from the star-forming component. The variable parameters and priors are given in Table 3.

We note that the above procedure takes into account only spectroscopy. In principle, this could cause the stellar masses to be significantly underestimated for extended hosts due to some of their light ending up outside the shutter. To mitigate this issue and provide an additional check on BEAGLE stellar mass estimates, we carry out photometric fitting of our sample sources using CIGALE(M. Boquien et al. 2019). The photometry used came from the JADES DR3 catalogue (F. D'Eugenio et al. 2024a) and was available for 28 of our sources. The SFH was modelled using a delayed SFH model with an exponential burst and BC03 stellar population models from G. Bruzual & S. Charlot (2003) were used to model stellar emission. Stellar dust attenuation was modelled using the D. Calzetti et al. (2000) dust attenuation law, while D. A. Dale et al. (2014) models were used to compute dust emission. The AGN accretion disc emission was modelled using an attenuated power law from M. Stalevski et al. (2016). The parameters used for each model are summarized in Table 4.

After fitting each source according to the procedures above, we compare the M_* values given by BEAGLE to those of CIGALE and find that they are generally consistent within ~ 0.4 dex. We obtain our final M_* estimates for sources for which either BEAGLE or CIGALE give reduced-chi-square $\chi^2_R < 3$, preferring the BEAGLE result if both fits are equally good and the source does not contain significant extended components. For hosts with extended morphology (a total of five), we use the CIGALE estimates. Following these procedures we were able to estimate stellar masses for most of our sources, except GS-209777 for which the stellar component is likely completely subsumed by AGN emission (Fig. 1) and thus both BEAGLE and CIGALE fail to give satisfactory fits. In addition, the photometric stellar mass estimates for GN-28074 and GS-159717 are higher than the upper limit on M_{dyn} (I. Juodžbalis et al. 2024a; D'Eugenio (in preparation)), while BEAGLE fitting fails to reproduce the spectral shape well, thus we are unable to reliably estimate their host's stellar mass. The stellar mass and σ_* estimates for our sample sources are given in Table 5 .

Table 3. Parameters and priors used in BEAGLE fitting.

Component	Parameter	Description	Prior
SFH	$\log(M_{tot}/\mathrm{M}_\odot)$	Integrated SFH mass	Uniform $\in [5, 12]$
	$\log(\tau_{SFR}/\mathrm{yr})$	Exponential decline in delayed SFH ($SFR \propto t\exp[-t/\tau_{SFR}]$ for $t > 10$Myr)	Uniform $\in [6, 12]$
	$\log(t/\mathrm{yr})$	Maximum age of stars	Uniform $\in [7, 10.8]$
	$\log(SFR/\mathrm{M}_\odot\,\mathrm{yr}^{-1})$	Constant SFR for $t < 10$Myr	Uniform $\in [-4, 4]$
	$\log(Z_*/\mathrm{Z}_\odot)$	Metallicity of the stars	Uniform $\in [-2.2, 0.24]$
	$m_{\mathrm{up}}/\mathrm{M}_\odot$	IMF upper mass cut-off	Fixed to 300
Nebular	$\log(Z_{gas}/\mathrm{Z}_\odot)$	Nebular gas metallicity	Fixed to Z_*
	$\log U$	Ionization parameter	Uniform $\in [-4, -1]$
	ξ_d	Dust-to-metal mass ratio	Fixed to 0.3
Attenuation	$\hat{\tau}_V$	Effective V-band optical depth to stars	Exponential $\in [0, 6]$
	μ	Fraction of $\hat{\tau}_V$ from dust in the diffuse inter-stellar medium	Fixed to 0.4
	$\hat{\tau}_{V,AGN}$	Effective V-band optical depth of the AGN power-law component	Exponential $\in [0, 6]$
AGN emission	$\log(f_{AGN})$	fractional contribution of AGN to 1500 Å	Uniform $\in [-3, 3]$
	$\mathrm{slope}_{\mathrm{PL}}$	AGN continuum power law slope	Fixed -1.54 or -2.33

Table 4. A summary of CIGALE fitting parameters used. The first column indicates the emission component, second column lists the exact model, and the third column lists parameters used to compute model grid. Parameters not listed were kept to CIGALE defaults.

Component	Model	Parameters
SFH	Delayed SFH	$T_{main} = 100, 1000, 5000, 10000$ Myr
		$T_{burst} = 5, 20$ Myr
		$f_{burst} = 0, 0.2$
SSP	BC03	$Z_* = 0.02, 0.0001$
Nebular		$\log U = -1.0, -2.0, -3.8$
		$Z_{gas} = 0.02, 0.0004$
		$n_e = 100, 1000\ \mathrm{cm}^{-3}$
		$FWHM = 300, 600, 2000\ \mathrm{km\ s}^{-1}$
Attenuation	Calzetti00	$E(B-V) = 0, 0.3, 1.0, 1.5, 3.0$
Dust emission	Dale2014	$\alpha = 1.3125, 2.0, 4.0$
AGN emission	Skirtor	$i = 30, 70$
		$f_{AGN} = 0, 0.1, 0.5, 0.6, 0.8, 0.9$
		$E(B-V) = 0.03, 0.5, 1.5, 3.0$

5.3 AGN–host galaxy imaging decomposition and stellar masses from resolved SEDs

The stellar mass estimation methods described in the previous section are prone to degeneracies stemming from the difficulty in disentangling AGN and host galaxy emission. In order to investigate their impact on the stellar mass estimates and obtain more unbiased measurements, we use the tool `ForcePho` (Johnson B., in preparation) to decompose each of our sample sources into galaxy and AGN components and perform fractional SED fitting to re-examine their stellar masses.

The decomposition procedure followed the methodology of S. Tacchella et al. (2023), W. M. Baker et al. (2025c), and I. Juodžbalis et al. (2024b) in which the AGN emission was modelled as a point source, while the underlying galaxy was assumed to follow a Sérsic light profile. Within `ForcePho`, the point source component has its half-light radius limited to $r_e < 0.01$ arcsec (making it completely unresolved by NIRCam), while the Sérsic index is fixed to one to avoid any significant extended flux resulting from higher order profiles. The host galaxy component has a freely varying Sérsic index from 0.8 to 6 and varying effective radius. `ForcePho` works by fitting the individual exposures simultaneously enabling it to extract sub-pixel information due to dithering (W. M. Baker et al. 2025c). It enables the flux to vary freely between the bands, while the structural information (e.g. position, Sérsic index, half-light radius, and ellipticity) of the profile are based on the combined information of all the bands. This enables it to fit varying colour gradients as multiple distinct components (e.g. central cores and discs, W. M. Baker et al. 2025c). The PSF is modelled as a combination of Gaussians using a Gaussian Mixture Model (GMM) enabling straightforward convolutions with the Sérsic profiles used to model the light distribution. Recovery tests of the PSF approximations in the case of multiple component fits have been performed previously in W. M. Baker et al. (2025c).

Each fit was visually inspected and those with significant residuals were discarded. This mostly included bright point-source-dominated objects such as GN-28074, GS-209777, and GS-49729 as the GMM approximation used by `ForcePho` breaks down for bright point sources that illuminate the non-Gaussian wings of the PSF. The decomposition also failed for GS-159717 due to significant foreground contamination by a $z \sim 1$ galaxy D'Eugenio (in preparation). In addition, `ForcePho` struggled with objects exhibiting complex morphology, such as GS-204851, which consists of several distinct clumps (Fig. A4). It should be noted, however, that such clumpy hosts are likely interacting merging systems and present a general problem of which clumps should be attributed to the AGN host.

We also discard fits that appear to be well modelled by a single Sérsic profile. In these cases, the point source component absorbs all the flux, while the radius of the host galaxy expands to unfeasible sizes and records near zero fluxes by fitting any remaining background.

The fitting of the decomposed point source photometry was carried out using CIGALE with the same model components as in Table 4, except with f_{AGN} being fixed to 0. In addition, we mask all filter bands that include the [O III]$\lambda\lambda$4959,5007 doublet and Hα in their transmission window to avoid residual contamination by AGN photoionization. We utilized the same acceptance criteria as in the previous section, requiring $0.5 < \chi^2_R < 3$ for a robust result. This fitting produced stellar masses and sizes for 14 objects out of the whole sample, mostly located at $4 < z < 7$, with a median redshift of 5. As `ForcePho` performs better on brighter extended sources, we expect this subset to be slightly biased towards higher M_* hosts. We use the stellar masses obtained from `ForcePho` photometry to assess the potential biases introduced to previous

Table 5. Summary of host properties derived for our sample AGN. The first column lists the IDs of each object in the same order as Table 2. The second and third columns contain M_* estimates and χ^2_R values given by BEAGLE fitting. Columns 4 and 5 contain the same values, but obtained from CIGALE fits. Column 6 gives the estimates of stellar velocity dispersions for each host. The remaining three columns show the half-light radii obtained from `ForcePho` decompositions, the M_* values obtained from decomposed photometry, and Sérsic indices. Sources marked with '†' are significantly extended, thus CIGALE fitting results were used as best estimates for their M_*. Values of $\log \sigma_*$ marked with '$*$' were inferred from fitting R1000 rather than R2700 data. The uncertainties on them also reflect the ~0.15 dex intrinsic scatter on the calibrations, which ends up dominating the combined errors in most cases.

Object ID	$\log M_*/\mathrm{M}_\odot$ BEAGLE	χ^2_R BEAGLE	$\log M_*/\mathrm{M}_\odot$ CIGALE	χ^2_R CIGALE	$\log \sigma_*$	M_{UV}	R_e [pc]	$\log M_*/\mathrm{M}_\odot$ FPHO	n_s
Robust									
GS-30148179	$8.95^{+0.58}_{-0.58}$	1.46	$8.78^{+0.04}_{-0.04}$	0.36	$2.10^{+0.13}_{-0.13}$	−20.36	–	–	–
GS-10013704	$8.90^{+0.90}_{-0.90}$	0.85	$8.28^{+0.08}_{-0.08}$	0.62	$1.86^{+0.14}_{-0.14}$	−18.95	137^{+23}_{-23}	$9.04^{+0.02}_{-0.02}$	$0.89^{+0.14}_{-0.14}$
GS-210600	$8.40^{+0.61}_{-0.61}$	1.49	$8.26^{+0.02}_{-0.02}$	1.59	$1.76^{+0.14}_{-0.14}$	−18.61	283^{+45}_{-45}	$7.51^{+0.08}_{-0.08}$	$0.81^{+0.13}_{-0.13}$
GS-209777	–	–	–	–	$2.14^{+0.21}_{-0.21}*$	−18.17	–	–	–
GS-204851	$10.74^{+0.09}_{-0.09}$	0.93	$8.94^{+0.04}_{-0.04}$	1.75	$1.91^{+0.13}_{-0.13}$	−18.85	–	–	–
GS-179198†	$8.44^{+0.05}_{-0.05}$	0.79	$9.43^{+0.06}_{-0.06}$	0.53	$1.92^{+0.13}_{-0.13}$	−19.10	380^{+61}_{-61}	$8.41^{+0.17}_{-0.17}$	$5.88^{+0.94}_{-0.94}$
GS-172975	$8.98^{+0.14}_{-0.14}$	0.81	$8.30^{+0.70}_{-0.70}$	1.21	$1.70^{+0.16}_{-0.16}$	−17.74	–	–	–
GS-159717	–	–	–	–	$1.62^{+0.14}_{-0.14}$	−19.09	–	–	–
GS-159438†	$8.35^{+0.13}_{-0.13}$	2.64	$9.14^{+0.18}_{-0.18}$	1.97	$2.15^{+0.13}_{-0.13}$	−20.98	–	–	–
GN-77652	$8.36^{+1.64}_{-1.64}$	1.82	$8.20^{+0.04}_{-0.04}$	1.42	$1.79^{+0.31}_{-0.31}$	−18.27	269^{+44}_{-44}	$7.79^{+0.13}_{-0.13}$	$0.85^{+0.14}_{-0.14}$
GN-73488	$9.71^{+0.33}_{-0.33}$	1.83	$8.50^{+0.53}_{-0.53}$	2.26	$2.06^{+0.15}_{-0.15}$	−18.87	–	–	–
GN-62309	$7.78^{+0.34}_{-0.34}$	0.94	$8.52^{+0.18}_{-0.18}$	0.94	$1.80^{+0.13}_{-0.13}$	−18.58	293^{+48}_{-48}	$8.44^{+0.26}_{-0.26}$	$3.11^{+0.50}_{-0.50}$
GN-61888	$8.53^{+1.73}_{-1.73}$	0.84	$8.25^{+0.10}_{-0.10}$	0.56	$1.78^{+0.14}_{-0.14}$	−18.78	–	–	–
GN-53757	$10.38^{+0.19}_{-0.19}$	0.63	$9.44^{+0.31}_{-0.31}$	1.19	$1.79^{+0.15}_{-0.15}$	−18.86	618^{+99}_{-99}	$8.81^{+0.26}_{-0.26}$	$0.80^{+0.13}_{-0.13}$
GS-49729	–	–	$10.14^{+0.25}_{-0.25}$	3.14	$2.08^{+0.21}_{-0.21}*$	−21.38	–	–	–
GS-38562	$9.76^{+0.09}_{-0.09}$	1.09	$9.57^{+0.08}_{-0.08}$	1.19	$1.83^{+0.14}_{-0.14}$	−18.98	174^{+30}_{-30}	$9.31^{+0.17}_{-0.17}$	$1.02^{+0.16}_{-0.16}$
GN-38509	$9.19^{+0.40}_{-0.40}$	1.05	$9.43^{+0.31}_{-0.31}$	0.87	$2.08^{+0.23}_{-0.23}*$	−19.15	137^{+23}_{-23}	$8.92^{+0.30}_{-0.30}$	$0.94^{+0.15}_{-0.15}$
GN-29648†	$9.71^{+0.01}_{-0.01}$	1.38	$10.31^{+0.06}_{-0.06}$	1.40	$1.93^{+0.21}_{-0.21}*$	−19.00	–	–	–
GN-28074	–	–	–	–	$1.65^{+0.24}_{-0.24}*$	−20.15	–	–	–
GN-20621	$8.41^{+1.58}_{-1.58}$	1.38	$8.08^{+0.10}_{-0.10}$	1.11	$1.86^{+0.13}_{-0.13}$	−18.61	–	–	–
GS-17341†	$8.54^{+0.32}_{-0.32}$	1.09	$8.84^{+0.032}_{-0.03}$	1.14	$1.95^{+0.21}_{-0.21}*$	−19.54	–	–	–
GS-13329	$9.52^{+0.14}_{-0.14}$	0.75	$8.26^{+0.41}_{-0.41}$	1.16	$1.78^{+0.14}_{-0.14}$	−18.59	409^{+66}_{-66}	$8.60^{+0.15}_{-0.15}$	$5.86^{+0.94}_{-0.94}$
GN-11836	$8.17^{+0.15}_{-0.15}$	1.94	$8.52^{+0.50}_{-0.50}$	2.98	$1.96^{+0.13}_{-0.13}$	−18.89	451^{+74}_{-74}	$8.35^{+0.19}_{-0.19}$	$0.86^{+0.14}_{-0.14}$
GS-9598†	$9.08^{+0.38}_{-0.38}$	0.96	$9.48^{+0.02}_{-0.02}$	3.11	$1.93^{+0.21}_{-0.21}*$	−18.70	–	–	–
GS-8083	$8.27^{+0.14}_{-0.13}$	1.08	$8.30^{+0.15}_{-0.15}$	2.11	$1.89^{+0.13}_{-0.13}$	−18.67	72^{+11}_{-11}	$8.73^{+0.38}_{-0.38}$	$5.90^{+0.94}_{-0.94}$
GN-2916	$8.98^{+0.97}_{-0.97}$	0.95	$9.57^{+0.05}_{-0.05}$	1.30	$1.78^{+0.14}_{-0.14}$	−19.42	–	–	–
GN-1093	$8.43^{+0.63}_{-0.63}$	1.55	$8.77^{+0.39}_{-0.39}$	1.29	$1.91^{+0.14}_{-0.14}$	−18.03	–	–	–
GN-954	$10.93^{+0.11}_{-0.11}$	1.60	$9.68^{+0.30}_{-0.30}$	0.67	$1.79^{+0.21}_{-0.21}*$	−19.94	331^{+53}_{-53}	$8.46^{+0.11}_{-0.11}$	$0.80^{+0.13}_{-0.13}$
Tentative									
GS-200679†	$8.16^{+0.20}_{-0.20}$	1.67	$8.53^{+0.13}_{-0.13}$	0.98	$1.82^{+0.22}_{-0.22}*$	−20.26	408^{+65}_{-65}	$8.07^{+0.21}_{-0.21}$	$1.91^{+0.31}_{-0.31}$
GN-23924†	–	–	$11.01^{+0.03}_{-0.03}$	1.81	$2.07^{+0.13}_{-0.13}*$	−20.05	–	–	
Tentative Hβ									
GS-20057765	$7.40^{+0.78}_{-0.97}$	0.53	$8.08^{+0.30}_{-0.30}$	1.45	–	−19.21	–	–	–
GS-20030333	–	–	$8.61^{+0.20}_{-0.20}$	1.76	–	−19.29	94^{+15}_{-15}	$8.24^{+0.08}_{-0.08}$	$5.49^{+0.88}_{-0.88}$
GS-164055†	$7.27^{+0.68}_{-0.87}$	0.55	$7.99^{+0.23}_{-0.23}$	1.60	–	−18.75	–	–	–
GN-4685	$9.91^{+0.22}_{-0.21}$	0.80	$9.92^{+1.24}_{-1.24}$	0.55	–	−18.15	–	–	–

CIGALE and BEAGLE fitting by including the light produced by the central AGN. The comparisons are shown in Fig. 4, where we plot both the absolute mass differences ($\Delta M_* = \log M_{\mathrm{REF}} - \log M_{\mathrm{FPHO}}$) and the same values normalized by the errors on both estimates combined in quadrature as functions of stellar mass estimated by `ForcePho`. The comparisons indicate that both photometric and spectral fitting, which do not spatially decompose AGN and host galaxy light, tend to systematically overestimate stellar masses by about 2–3σ (1–2 dex); however, spectroscopic fitting by BEAGLE appears to be slightly more accurate than CIGALE. This bias appears uniform and not strongly affected by the host mass. However, `ForcePho` struggles with fitting bright, morphologically complex sources, thus fits could not be obtained for the brighter, more massive hosts of our sample AGN, which complicates the assessment of stellar mass overestimation in the high-mass regime. In principle, M_* estimates for more massive hosts should be less affected by the presence of AGN as most of our sample AGN are relatively faint (Fig. 2) and stellar light would be expected to dominate over the AGN continuum in cases of massive hosts.

Table 6. Table summarizing the measurements obtained from the stacked spectra and their variation across the redshift bins. The first column lists the values being measured, second column measurements for the stack of all sample sources. The subsequent columns give the measurements for $z > 5$, $3.5 < z < 5$, and $z < 3.5$ bins, respectively. The line fluxes are all given in 10^{-20} erg s^{-1} cm^{-2}. In case of a non-detection, a 3σ upper limit is given. The line flux uncertainties on the values in column two reflect the 20 per cent systematic error arising from flux calibration differences between different R1000 grating/filter combinations.

Value	All redshifts	$z < 3.5$	$3.5 < z < 5$	$z > 5$
$F_{H\alpha,nr}$	676^{+135}_{-135}	3130^{+19}_{-150}	832^{+3}_{-3}	295^{+3}_{-3}
$F_{H\alpha,br}$	413^{+83}_{-83}	2236^{+46}_{-439}	307^{+4}_{-4}	518^{+5}_{-5}
$F_{H\beta,nr}$	160^{+32}_{-32}	815^{+7}_{-6}	253^{+2}_{-2}	$95.9^{+1.2}_{-1.3}$
$F_{H\gamma,nr}$	$85.1^{+17.1}_{-17.1}$	288^{+6}_{-8}	$99.3^{+1.9}_{-1.8}$	$45.5^{+2.2}_{-4.6}$
$F_{[OII]\lambda3727}$	$97.8^{+19.6}_{-19.6}$	1172^{+8}_{-8}	$93.2^{+2.8}_{-2.6}$	$40.1^{+2.0}_{-2.0}$
$F_{[OIII]\lambda4363}$	$30.9^{+6.3}_{-6.3}$	116^{+5}_{-7}	$36.7^{+1.7}_{-1.6}$	$16.7^{+3.7}_{-1.8}$
$F_{[OIII]\lambda5007}$	695^{+139}_{-139}	3333^{+8}_{-10}	1022^{+4}_{-4}	485^{+2}_{-2}
$F_{HeII\lambda4686}$	< 3.2	< 10.8	< 4.2	< 2.4
$F_{[SII]\lambda6716}$	$14.3^{+2.9}_{-2.9}$	168^{+8}_{-15}	$11.1^{+0.9}_{-1.0}$	< 3.0
$R_{[SII]}$	$0.90^{+0.07}_{-0.07}$	$0.96^{+0.06}_{-0.58}$	$0.88^{+0.13}_{-0.11}$	–
$F_{[NII]\lambda6583}$	$5.70^{+1.46}_{-1.46}$	492^{+10}_{-147}	$5.1^{+1.3}_{-1.3}$	< 1.5
$F_{[OI]6300}$	$60.1^{+12.5}_{-12.5}$	322^{+13}_{-13}	$28.1^{+5.3}_{-4.6}$	$32.3^{+5.9}_{-5.1}$

5.4 Dynamical masses

We also utilize morphological information gained from the `ForcePho` fits to constrain the dynamical masses of our AGN hosts. We utilize the calibrations from A. der Wel et al. (2022) and calculate the M_{dyn} via the following formula:

$$M_{\rm dyn} = K(n)K(q)\frac{\sigma_*^2 R_e}{G}, \tag{6}$$

where σ_* is the stellar velocity dispersion and R_e is the half light radius. $K(n)$ and $K(q)$ are morphological correction factors based on the Sérsic index (n) and axis ratio (q) and defined in A. der Wel et al. (2022) with $K(n) = 8.87 - 0.831n + 0.0241n^2$ and $K(q) = \left[0.87 + 0.38e^{-3.71(1-q)}\right]^2$.

6 HOST SCALING RELATIONS AND MORPHOLOGIES

In addition to studying the scaling relations of the full sample, in order to assess the potential redshift evolution, we also split it into three redshift bins. The first bin consists of 15 sources at $z > 5$ (including the tentative Hβ objects, Appendix B). The second bin contains 13 objects at $3.5 < z < 5$ and the final one six objects at $z < 3.5$. We focus on exploring the BH–stellar mass (M_{BH}–M_*) and BH–velocity dispersion (M_{BH}–σ_*) scaling relations as those involve the quantities most readily constrained by our data for the majority of our sample. Our `ForcePho` morphological fits also allow us to constrain dynamical masses for a smaller subsample of objects and investigate their positions with respect to the M_{BH}–M_{dyn} scaling relations.

6.1 The M_{BH}–M_* relation

BH mass–stellar mass relations for our entire sample and each redshift bin are presented in Fig. 5. We use the local M_{BH}–M_* relation from A. E. Reines & M. Volonteri (2015) for our comparisons as their BH mass estimation methods are consistent with ours (carried out using Hα measurements together with equation 4) and their sample focuses on late-type galaxies (i.e. consistent with the prevalent morphologies in our sample and most high-z galaxies), whereas studies like J. Kormendy & L. C. Ho (2013) focus on early type. For completeness, we also compare our measurements with scaling relations derived by J. E. Greene et al. (2020); however, we caution that they utilized different BH mass estimators, hence comparison with our results incurs additional uncertainties. From the figure, it is apparent that, overall, our sample BHs are overmassive with respect to the local relations, with the mean stellar to BH mass ratio of ~ 0.01 placing them 1–2 dex above the local relations from A. E. Reines & M. Volonteri (2015) and J. E. Greene et al. (2020), while the tentative Hβ sources have M_{BH}/M_* approaching unity. When split across the separate redshift bins, the sample exhibits some redshift evolution in the M_{BH}–M_* plane, with sources in the $3.5 < z < 5$ bin being about 0.5 dex closer to the local relation than those in the $z > 5$ bin. All objects in the $z < 3.5$ bin appear consistent with the local relation, suggesting that the local relation is being established below this redshift. However, the small number of sources in this bin, due to JADES spectroscopic target selection being biased against low-redshift objects, makes it hard to assess significance. It should be noted that the data from Y. Harikane et al. (2023) also follow a similar trend between $z > 5$ and $3.5 < z < 5$ redshift bins; however, their sample alone lacks the statistics to establish a robust trend. The higher source count of our sample establishes this evolution more robustly.

The offset from the local relation observed in the higher redshift bins does not appear to depend strongly on the M_{BH}/M_* ratio itself, albeit some extra deviation can be seen at the lower end of M_{BH} and M_*. This is indicative of some observational bias being present, as pointed out by J. Li et al. (2025a). However, as explored in I. Juodžbalis et al. (2024b), it is unlikely that all of the observed deviation from the local scaling relations can be attributed to selection effects, especially given that the bias should primarily apply for the most luminous AGN, while our sample includes dormant BHs. Another argument against biases playing a dominant role in the observed offset is that the same orders-of-magnitude offset is not seen in the M_{BH}–σ_* relation, which will be explored in the following section.

We note that the overmassive nature of high-z BHs remains regardless of how the stellar mass is inferred, i.e. regardless of whether it is obtained via spectrosopic or imaging decomposition, and regardless of the stellar fitting code adopted. Within this context, it should also be pointed out that the stellar mass estimates plotted in Fig. 5 may actually be overestimated since, as illustrated by Fig. 4, a fitting that decomposes AGN from host galaxy emission lowers the M_* estimates by about 3σ, potentially making our BHs even more overmassive. Finally, recent results indicating that part, or most, of the Balmer break observed in these AGN is likely non-stellar (K. Inayoshi & R. Maiolino 2024; F. D'Eugenio et al. 2025a; X. Ji et al. 2025) indicates that the stellar masses are likely overestimated, making the overmassive nature of BHs even more prominent.

6.2 The M_{BH}–σ_* and M_{BH}–M_{dyn} relations

We present the $M_{BH} - \sigma_*$ for our sources in the left pannel of Fig. 6. In this case all of our sources are much closer to the local scaling relation. The slight offset present is consistent with the scatter, particularly when taking into account the uncertainties on σ_* values. The only significant outlier (GN-28074) has σ_* inferred from R1000 data, which is less reliable due to the lower resolution

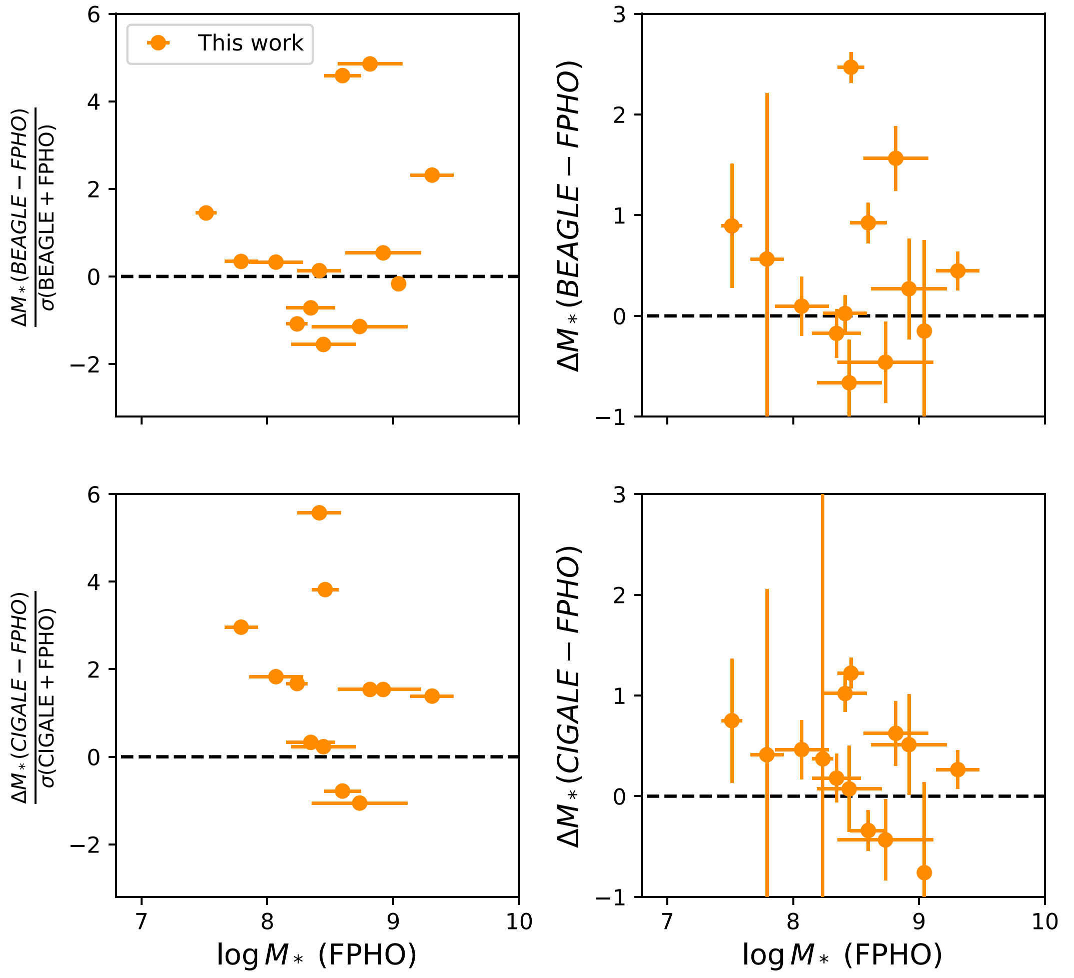

Figure 4. **Left column:** comparison between stellar mass estimates obtained from `ForcePho` and those obtained from fitting prism spectra (top) and integrated photometry (bottom). The value on the y-axis is the logarithmic difference in masses obtained by a given estimate (either CIGALE or BEAGLE) and `ForcePho` photometry, normalized to the total error on both estimates. **Left column:** same as the right column, except the absolute values of logarithmic difference are shown.

(Fig. 3). This lack of offset in the M_{BH}–σ_* relation across the whole redshift range, which is not reflected in the M_{BH}–M_* relation, seems to imply that the gas required for these sources to reach the local stellar mass scaling relations is already present, but it has not yet been efficiently converted to stars. In this scenario, BH feedback is an attractive solution to explain this inhibiting of star formation either through turbulence or heating. Ejective AGN feedback is instead unlikely as this would remove gas and make the two scaling relations more consistent; lack of significant ejective feedback in these AGN was already pointed out by R. Maiolino et al. (2025), who found a general lack of outflows. Alternatively, or in addition, contribution from dark matter (and with high DM/stellar ratio) may contribute to the M_{BH}–σ_* relation, while leaving an offset on the M_{BH}–M_* relation; this aspect will be explored in a separate paper (W. McClymont et al. 2026).

Additionally, this consistency of our sources with the local M_{BH}–σ_* relation implies that the offset seen in the M_{BH}–M_* relation cannot be entirely attributed to selection effects wherein lower mass BHs in more massive (higher M_* and σ_*) hosts are missed by observations. Indeed, selection effects on the BH masses should be seen as similar, orders of magnitude, offsets on the M_{BH}–σ_* relation. In fact, as the M_{BH}–σ_* relation is tighter than M_{BH}–M_* relation, the offset in Fig. 6 should be even more apparent than in Fig. 5, which is not seen. Selection effect produces a characteristic 'banana' shape (J. Li et al. 2025a) as BHs in less massive hosts appear to be more overmassive. While both Figs 5 and 6 exhibit hints of excess deviation in the lower M_*/σ_* regime, indicative of this selection effect being present, the overall major shift towards local scaling relation when going from M_* to σ_* cannot be explained this way.

The right panel of Fig. 6 shows the M_{BH}–M_{dyn} relation for a subsample of 14 sources for which robust morphological constraints based on `ForcePho` fitting were possible. We focus on comparing with the M_{BH}–M_* relation from J. Kormendy & L. C. Ho (2013) as it is derived for gas-poor early type galaxies for which the stellar mass closely tracks the dynamical mass. As we show in Fig. 6, our sample AGN are largely consistent with the local relation by J. Kormendy & L. C. Ho (2013) and lie in the same region as most of their data points albeit generally occupying the lower mass range. This consistency with local M_{BH}–M_{dyn} and M_{BH}-σ_* relations together with the offset in the M_{BH}-M_* one implies either high gas fractions ($f_{gas} > 0.5$) or significant DM

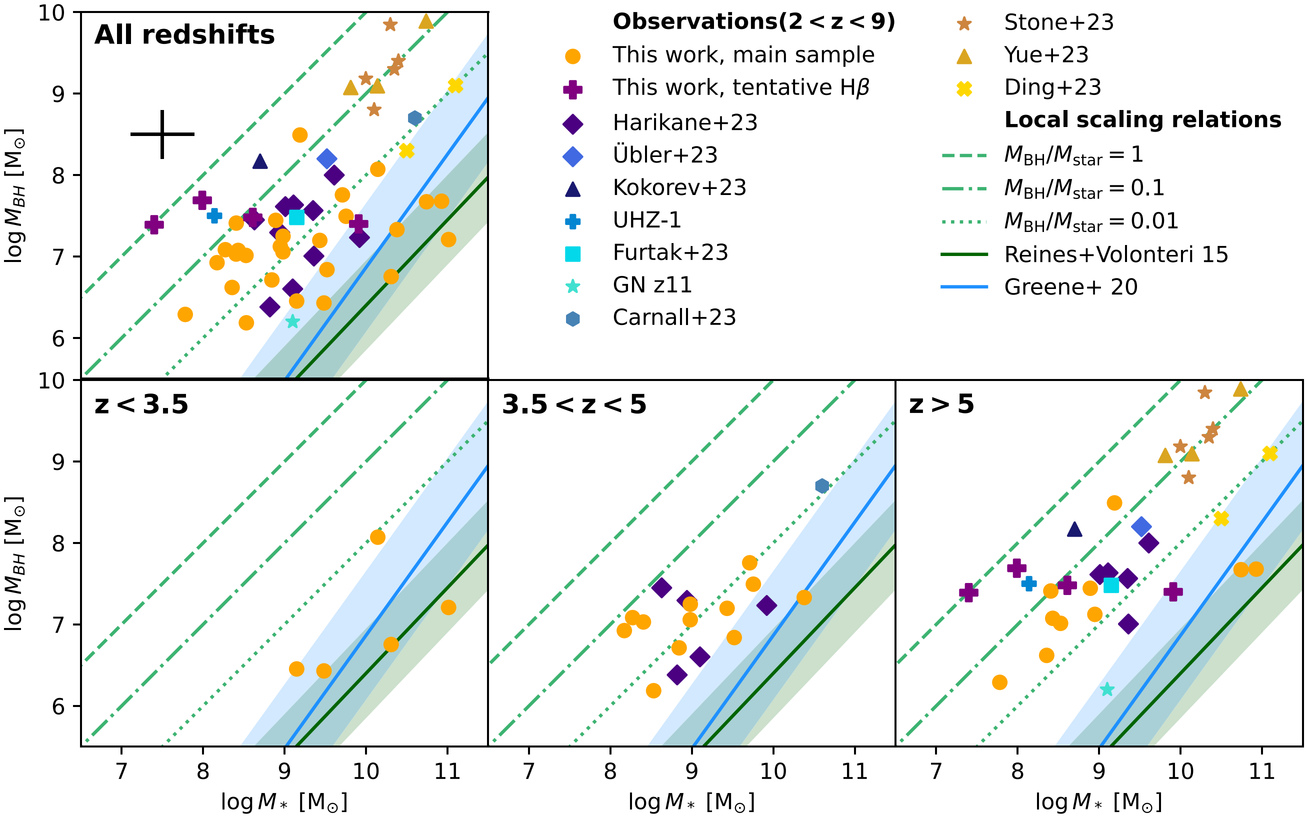

Figure 5. $M_{BH}-M_{star}$ relations of our sample sources for the entire sample and the three redshift bins. Main sample sources are shown as orange dots, the tentative Hβ detections – as purple crosses. Previous *JWST* observations by A. D. Goulding et al. (2023), Y. Harikane et al. (2023), H. Übler et al. (2023), and V. Kokorev et al. (2023) are shown in blue coloured markers. QSO observations by X. Ding et al. (2023), M. A. Stone et al. (2023), and M. Yue et al. (2024b) are shown as brown stars, triangles, and yellow crosses, respectively. The solid dark green line shows the local relation from A. E. Reines & M. Volonteri (2015) with the scatter indicated by green shading. Likewise, the blue line and shading show the relation and scatter from J. E. Greene et al. (2020). The constant M_{BH}/M_{star} ratios are shown by lighter green lines. The average errors on each data point are indicated by the black cross in the upper left panel.

contribution present in our sample of AGN hosts. If high gas fraction is primarily responsible for the effect, rather than high DM fraction, this would further indicate that the gas required to bring our sources on to the local M_{BH}–M_* scaling relation is already present. This implies that the feedback inhibiting star formation in our sample sources is likely of preventative rather than ejective nature.

As the consistency of our sources with the local M_{BH}–σ_* and M_{BH}–M_{dyn} scaling relations might imply the presence of AGN (non-ejective) feedback inhibiting star formation, we endeavor to explore the form this feedback takes by comparing our objects to HII regions and emission line galaxies on the $L_{H\beta}$–σ relation found by J. Melnick et al. (2017). If AGN feedback operates through excess turbulence induced in the NLR, our sources would be expected to deviate from the relation by drifting towards higher σ values for the same Hβ luminosity. We conduct the comparison using the L–σ relation derived by J. Melnick et al. (2017) and individual galaxy measurements by R. Chávez et al. (2014). Only sources with available R2700 data are used for this comparison, with the $\sigma_{[OIII]}$ values measured from the [O III]$\lambda\lambda$4959,5007 doublet and corrected for the LSF. We show the comparison in Fig. 7. As it can be seen in the figure, our sample of AGN does not exhibit significant deviations from the scaling relation and falls in line with emission line galaxies from R. Chávez et al. (2014). This indicates that the AGN feedback present in our sources is not dominated by turbulence, which would cause them to move towards higher $\sigma_{[OIII]}$ values for a fixed luminosity. Therefore, star formation in our sources is likely inhibited through heating, which is corroborated by the presence of a strong [O III]λ4363 auroral line emission in a fraction of our sources and its clear detection in the spectral stacks as discussed in Section 7.

6.3 Morphologies of Type 1 AGN hosts

Morphologies of galaxies hosting AGN are thought to trace the connections between growing BHs and their hosts and have been a subject of extensive research (G. Kauffmann et al. 2003; M. Pović et al. 2012; T. Getachew-Woreta et al. 2022). Until the launch of *JWST*, this has been largely limited to galaxies at $z < 2$ and while a comprehensive study of AGN and star-forming galaxy morphology is beyond the scope of this paper, the depth and resolution provided by *JWST* allows us to make headway. Our `ForcePho` fits have produced a subsample of 14 AGN hosts with good constraints on their half-light radii (R_e), Sérsic indices (n_s) and stellar masses, and enables comparison with size-mass relations derived for star-forming galaxies. The comparison of our objects with the R_e–M_* relations derived by N. Allen et al. (2024) and T. B. Miller et al. (2024), around the same redshifts,

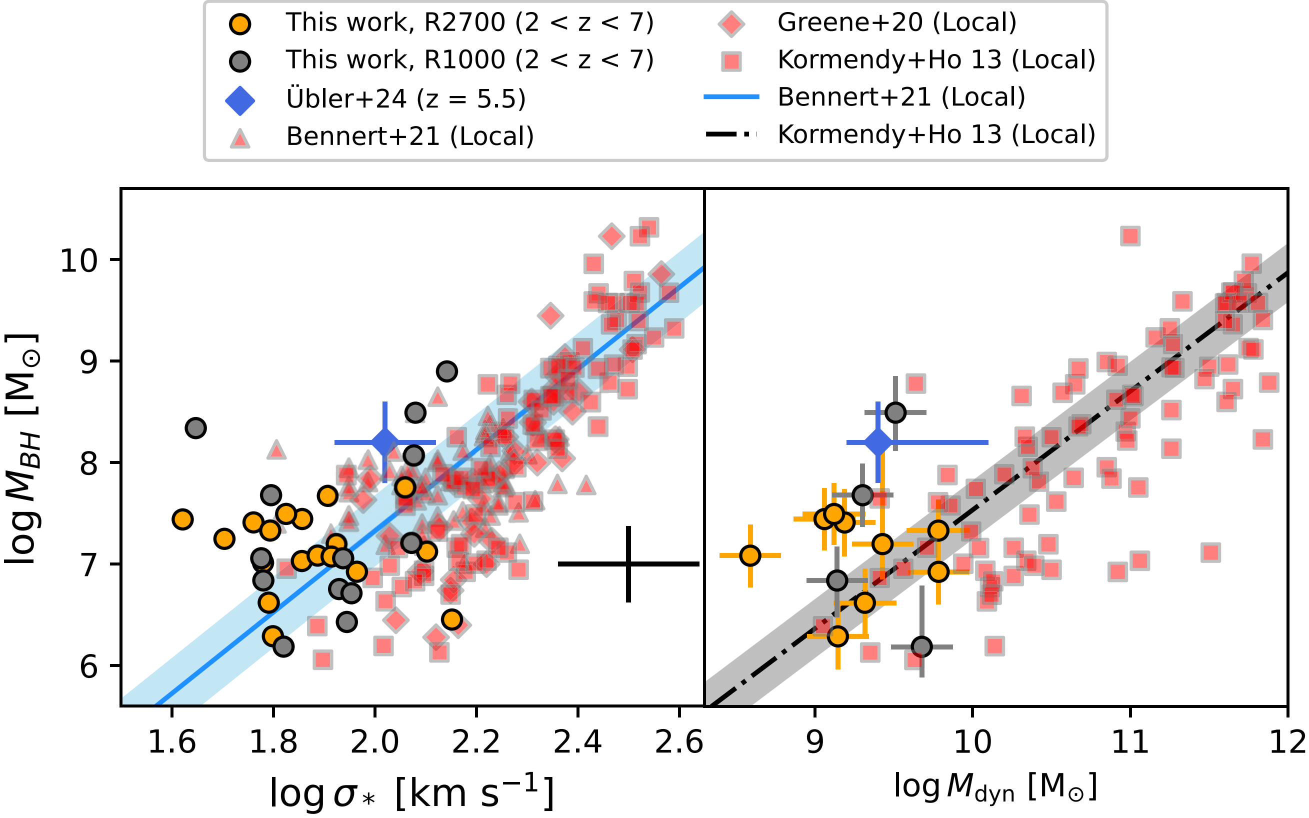

Figure 6. **Left panel:**$M_{BH}-\sigma_*$ relation for our AGN sample sources. The orange points show sources for which σ_* was estimated from R2700 data, grey points – those for which we used R1000 measurements. The blue line and the shaded region indicate the local relation from V. N. Bennert et al. (2021) and the 0.3 dex scatter on it, respectively. The average uncertainties of our data are shown by the black cross. Local measurements by J. Kormendy & L. C. Ho (2013), V. N. Bennert et al. (2021), and J. E. Greene et al. (2020) are shown by the red points. **Right panel:**$M_{BH}-M_{dyn}$ relation for a subsample of our AGN with robust morphological constraints. The markers have the same meaning as in the left panel. The black dash–dotted line is the scaling relation from J. Kormendy & L. C. Ho (2013) with grey shading indicating the scatter.

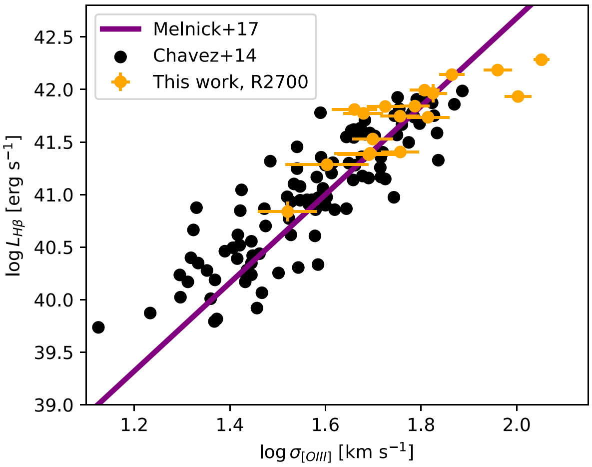

Figure 7. The Hβ luminosity–[O III] velocity dispersion relationship. The purple line shows the empirical relationship of J. Melnick et al. (2017) and emission-line galaxy measurements by R. Chávez et al. (2014) are shown by black dots. Our Type 1 AGN with R2700 data available are shown with yellow points. The Type 1 AGN are all consistent with the standard relation.

is shown in Fig. 8. The bulk of our objects are consistent with the relations; however, there is a significant population of AGN that are considerably more compact than star-forming galaxies at similar masses.

The apparent population of compact AGN hosts (Fig. 8) may indicate that these BHs may be fed by the same gas compaction mechanisms that are thought to drive bursty star formation in the early Universe (S. Tacchella et al. 2016; N. Emami et al. 2021; W. McClymont et al. 2025, and McClymont, in preparation). This compaction is thought to occur due to intense gas inflow events triggered by minor mergers, disc instabilities (A. Dekel & A. Burkert 2014; S. Tacchella et al. 2016) or accreting gas with low angular momentum from the halo (L. V. Sales et al. 2012; A. Renzini 2025). If such compaction mechanisms also end up feeding the central BH, it would explain the population of compact AGN hosts found in our sample and indicate that high-z AGN grew through different feeding modes than their local counterparts (as already suggested by D. D. Kocevski et al. 2017), which are primarily fed through major mergers and interactions within galaxy clusters (T. Storchi-Bergmann & A. Schnorr-Müller 2019) as well as galactic bars (F. Combes 2023; L. A. Silva-Lima et al. 2023).

The Sérsic index distribution for our sources is shown in Fig. 9 and clearly indicates that about 60 per cent of our sources are well fit by $n_s \approx 1$, indicating that most of the fitted AGN reside in late type, discy systems. On the other hand, the distribution

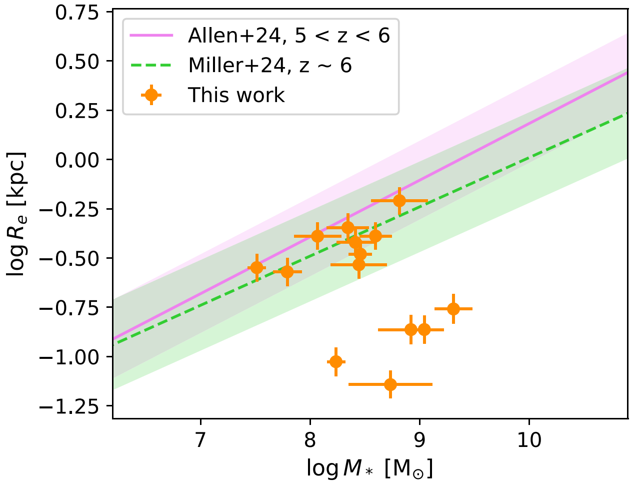

Figure 8. Location of our sample sources (orange points) relative to the mass–radius relations derived for star-forming galaxies by N. Allen et al. (2024) (purple solid line) and T. B. Miller et al. (2024) (green dashed line). The coloured shading indicates the ∼ 0.2 dex scatter on both relations.

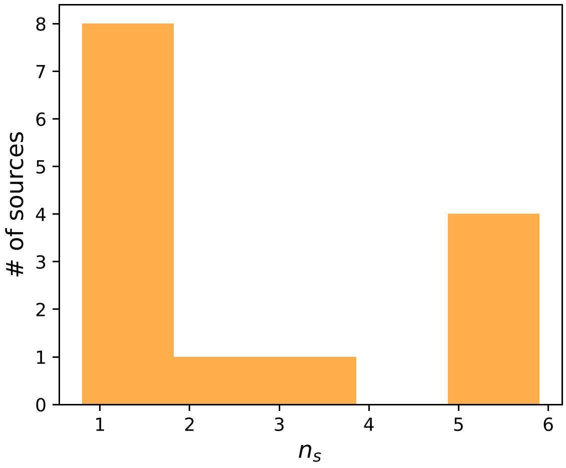

Figure 9. Histogram showcasing the distribution of Sérsic indices of our sample sources. It can be seen that the majority of our sources have n_s between 1 and 2, with a subset approaching steeper profiles at $n_s = 5$.

is clearly bimodal, with about 30 per cent of AGN hosts fit by more concentrated profiles. While the latter result may indicate that a fraction of AGN are hosted in more early type, spheroidal concentrated systems, we caution that a steeper profile may be the result of residual nuclear AGN emission.

Finally, we caution that the number statistics provided by our sample are small and suffer from biases inherent to the `ForcePho` fitting procedure (as discussed in Section 5.3), therefore it is too early to draw sweeping conclusions about the behaviour of AGN hosts at high redshift. Nevertheless, our results indicate the need for dedicated studies exploring AGN host morphologies at high redshifts.

7 STACKED SPECTRA OF TYPE 1 AGN

In order to further our investigation into the emission line properties of our sample sources, in particular to enhance the weak spectral features, we stack the R1000 spectra in our sample. The stacking was carried out as follows – first, each spectrum was de-redshifted to its rest frame utilizing the narrow-line redshifts derived by our pipeline fitting procedure. Afterwards we resample each spectrum onto a common wavelength grid, derived such that its bin widths would be half the size of the narrowest bin of the original spectra. This resampling is carried out using `spectres` (A. C. Carnall 2017). After resampling, we perform the stacking via a weighted sum with weights derived from the inverse rms errors on each bin. This method maximizes the S/N ratio of the stacked spectra, complimenting the median stacking done without weighting, normalized by $F_{[OIII]}$ carried out by Y. Isobe et al. (2025). We also experiment with normalizing the resampled spectra to $F_{[OIII]}$ and $F_{H\alpha,BLR}$ values, in order to investigate how robust the measured line ratios, on which we base our conclusions, are to different weighting schemes and find no significant differences. The errors on the stacks were estimated as the inverse square root of the sum of weights for each bin.

The above procedure was used to obtain stacks for all sample sources as well as those in each of the previously defined redshift bins. We focus our stacking on the regions surrounding the Hα and Hβ lines as stacks covering the full wavelength range are prone to producing continuum artefacts due to flux calibration issues between different R1000 gratings.

The stacked spectra in the region around Hα are shown in Fig. 10 and clearly show a decrease in the strength of [N II]$\lambda\lambda$6548,6583 and [S II]$\lambda\lambda$6716,6731 doublets relative to Hα as well as an increase in the prominence of the broad component relative to the narrow Hα, when going from lower to higher redshifts.

The stacked spectra in the region around Hβ are shown in Fig. 11 and illustrate the notable presence of the auroral [O III]λ4363 line across all redshifts. However, the He II λ4686 emission is entirely absent from the stacked spectra; the implications of this will be discussed in Section 7.2. In addition, the [O III]λ5007 emission profiles are narrow – suggesting a systematic lack of prominent large scale outflows in our sample of AGN, a feature also found in other Type 1 AGN *JWST*-selected samples (R. Maiolino et al. 2025).

We perform Gaussian fits to the lines found in our stacked spectra in order to obtain line fluxes from our stacked spectra. The fitting procedure followed that of Section 3, with the exception of the redshift of the narrow lines being set to zero and the [O II]$\lambda\lambda$3726,3728 doublet being fitted with a single Gaussian profile centred on 3727 Å as our spectral resolution is insufficient to disentangle its components. The results from this fitting are summarized in Table 6. It should be noted that the fluxes for the [O II]$\lambda\lambda$3726,3728 doublet were obtained from additional stacks centred on the line as, due to [O II]$\lambda\lambda$3726,3728 ending up on different R1000 gratings to Hβ, stacks centred on Hβ contained too few sources in the [O II]$\lambda\lambda$3726,3728 region to be representative of the whole sample. We also list the measured [S II] doublet ratios which change little across the different redshift bins, corresponding to n_e values between ∼ 500 and ∼ 800 cm^{-3} when estimated using the calibrations from M. Kaasinen et al. (2017).

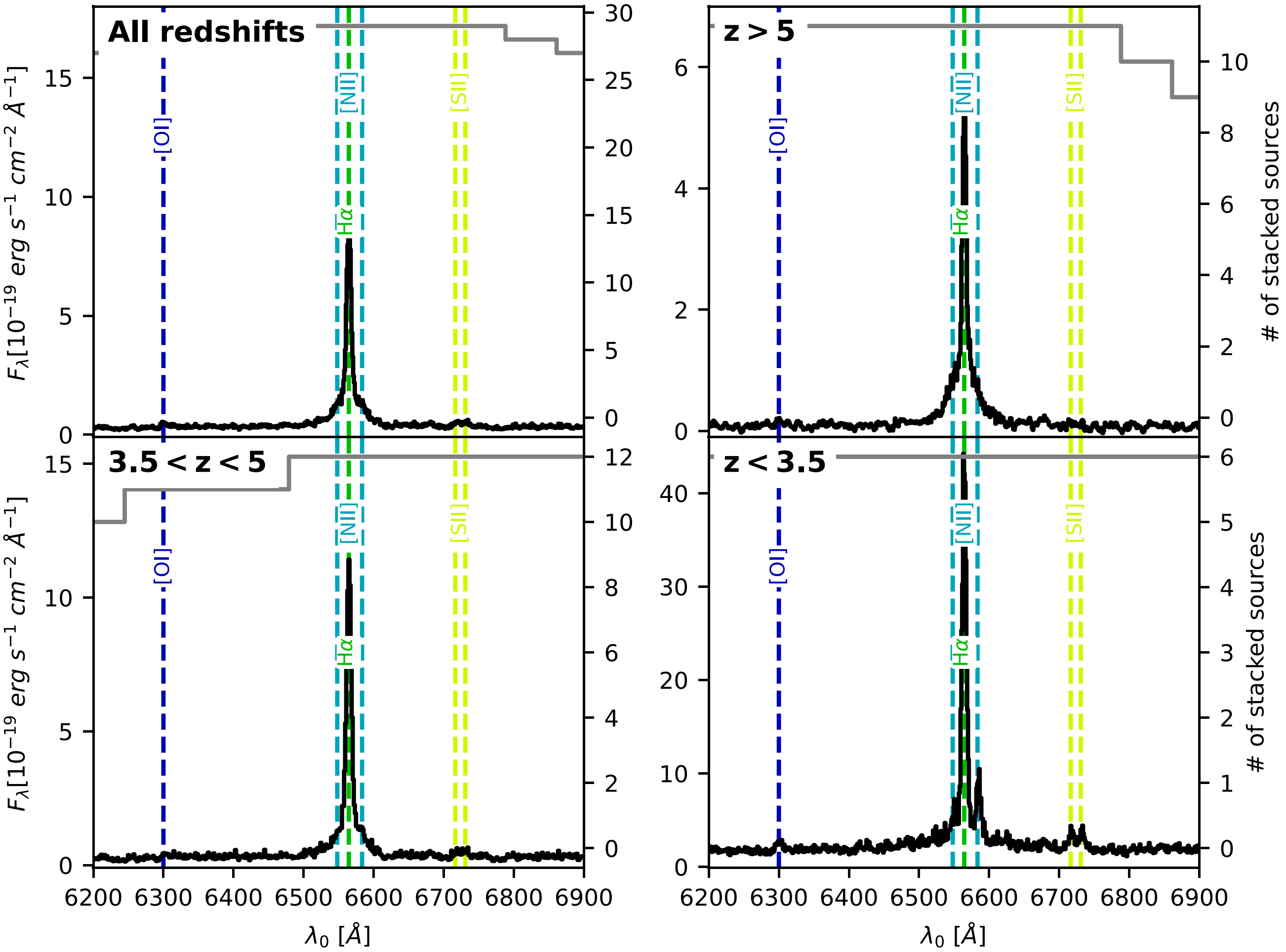

Figure 10. Medium-resolution stacks of the Hα region of our sample spectra. The black line shows the flux, while the grey line on top of each plot shows the number of sources that were stacked in each wavelength range. The positions of the [O I]λ6300, Hα, [N II], and [S II] lines are indicated by dashed vertical lines.

7.1 Balmer decrement and dust extinction

The (narrow) Hα to Hβ ratios measured from our stacked spectra show clear redshift evolution and range from $3.85^{+0.08}_{-0.20}$ to $3.29^{+0.03}_{-0.03}$ and $3.08^{+0.05}_{-0.05}$ for the $z < 3.5$, $3.5 < z < 5$, and $z > 5$ bins, respectively (Fig. 12). This is consistent with redshift evolution of dust obscuration, corresponding to A_V decreasing from ~ 1 to ~ 0.2, if the SMC extinction curve is assumed. These values are broadly consistent with those of individual sources in Table 2, for which the measured Balmer decrements generaly indicate minor to moderate dust obscuration. Although red outliers appear present across the redshift range. Either way, our sample sources do not exhibit Balmer decrements below the Case B value of 2.86 as found in a Type 1 AGN sample from M. Brooks et al. (2024) and emission line galaxies by C. Scarlata et al. (2024). The interpretation of M. Brooks et al. (2024) for obtaining $F_{H\alpha}/F_{H\beta} < 2.86$ was increased temperature in the ISM. Following this interpretation, our ratios of > 3 may be explained by lower ISM temperatures or higher dust obscuration in the NLR masking the lower ratio. However, our stacks display clear [O III]λ4363 emission, which indicates $T_e \approx 2 \times 10^4$ K across all bins, when using `pyNeb` (V. Luridiana, C. Morisset & R. A. Shaw 2015) and assuming $n_e = 600\ \mathrm{cm}^{-3}$. This indicates that the ISM in our sources is warm and may suggest that the A_V values in Table 2 may be underestimated as they were calculated assuming a standard Case B ratio of 2.86. However, as pointed out by D. E. Osterbrock & G. J. Ferland (2006), A. Smith et al. (2022), and L. Sandles et al. (2024), the intrinsic Hα and Hβ flux ratio varies by less than 10 per cent in the range $5000\ \mathrm{K} \leq \mathrm{T_e} \leq 20\,000\ \mathrm{K}$ and $500\ \mathrm{cm}^{-3} \leq \mathrm{n_e} \leq 10\,000\ \mathrm{cm}^{-3}$. Thus, a significant underestimation of A_V is unlikely.

It should be noted that the Hα and Hβ ratio for the stack of all sample sources is $F_{H\alpha}/F_{H\beta} \approx 4.2$, this is considerably higher than the stacks in the individual redshift bins and is inconsistent with the $F_{H\gamma}/F_{H\beta} \approx 0.53$, above the Case B value, for the same stack. Since this inconsistency is not present in the stacks of individual redshift bins, a likely reason for this discrepancy is flux calibration issues between the different grating/filter combinations of R1000. In order to check for any issues with our stacking procedure itself, we generate mock spectra with a fixed Case B $F_{H\gamma}/F_{H\beta}$ of 0.47 and find that the stacked spectra recover the set value. Thus the deviations in the stack of the entire sample are likely due to systematic errors in the flux calibrations (A. J. Bunker et al. (2024) points our ~ 10 per cent flux differences between prism and gratings). These systematics do not affect the individual redshift bins as much since the stacked lines are more likely to end up in the same grating/filter. Comparing the $F_{H\alpha}/F_{H\beta}$

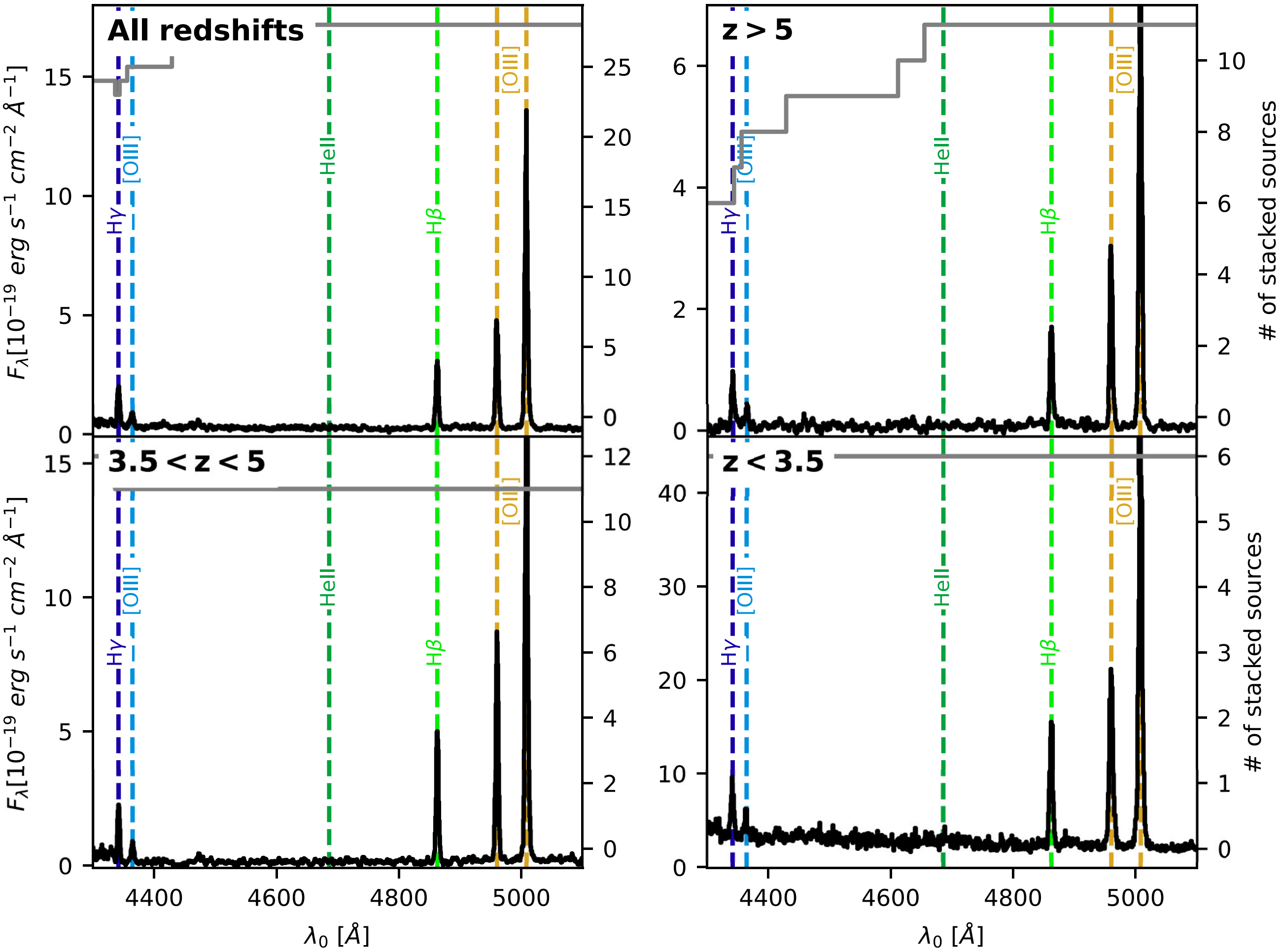

Figure 11. Medium-resolution stacks of the Hβ region of our sample spectra. The lines hold the same meaning as in Fig. 10. The dashed vertical lines indicate the locations of the Hγ, Hβ, [O III], and He II emission lines.

and $F_{H\gamma}/F_{H\beta}$ values of the entire sample stack to a weighted mean of the results in the individual redshift bins we find that the magnitude of this systematic uncertainty is in the 10–20 per cent range. We thus add 20 per cent to the fit uncertainties presented in the 'All redshifts' column of Table 6 and caution that any stacking of involving the full range of grating/filter combinations of R1000 must carefully account for the flux calibration differences.

7.2 Narrow-line ratio diagnostics

Both recent and pre-*JWST* era observations have shown that traditional narrow line diagnostic diagrams, such as the BPT (J. A. Baldwin et al. 1981) and VO87 (S. Veilleux & D. E. Osterbrock 1987) diagrams, struggle to robustly identify Type 2 AGN at higher redshifts due to the sensitivity of their lines to metallicity and more intense starburst activity (D. Masters et al. 2014; A. L. Coil et al. 2015; J. Scholtz et al. 2023; H. Übler et al. 2023). As a significant fraction of AGN are expected to be in the Type 2 regime (B. Vijarnwannaluk et al. 2022; J. Scholtz et al. 2023), exploring alternative narrow line diagnostics is crucial in working towards a complete census of high-redshift AGN in both obscured and unobscured regimes. The statistics and redshift coverage of our sample allow for thorough testing of classical and newly established Type 2 AGN diagnostics and assessing their redshift evolution.

We therefore utilize our broad-line AGN sample to check their location on the new and old narrow line ratio diagnostic diagrams. We first focus on the traditional N2 = log [N II]/Hα, R3 = log [O III]/Hβ BPT diagram (J. A. Baldwin et al. 1981) as well as similar diagrams incorporating [O I]λ6300, [S II] and He II λ4686 lines (S. Veilleux & D. E. Osterbrock 1987; L. J. Kewley et al. 2001; M. Shirazi & J. Brinchmann 2012). Panel **a** of Fig. 13 shows the distribution of our sources in the traditional N2-R3 BPT diagram (J. A. Baldwin et al. 1981). Most of them lie firmly in the star-forming regions of the plot as found in other studies of high-redshift Type 1 and Type 2 AGN (Y. Harikane et al. 2023; J. Scholtz et al. 2023; H. Übler et al. 2023; R. Maiolino et al. 2024; G. Mazzolari et al. 2025, 2024b; B. E. Backhaus et al. 2025). We also utilize the stacked R1000 spectra to investigate the presence of faint UV/optical lines. The N2 and R3 ratios from the stacks are also shown in Fig. 13 and showcase that, even if detected, the [N II] emission is too weak to classify our sources as AGN. In addition, the stacks in Fig. 13 also show strong evolution of the N2 ratio with redshift as the $z < 3.5$ stack is considerably closer to the boundary than the higher redshift ones, albeit still not in the AGN region of the diagram. This evolution is likely

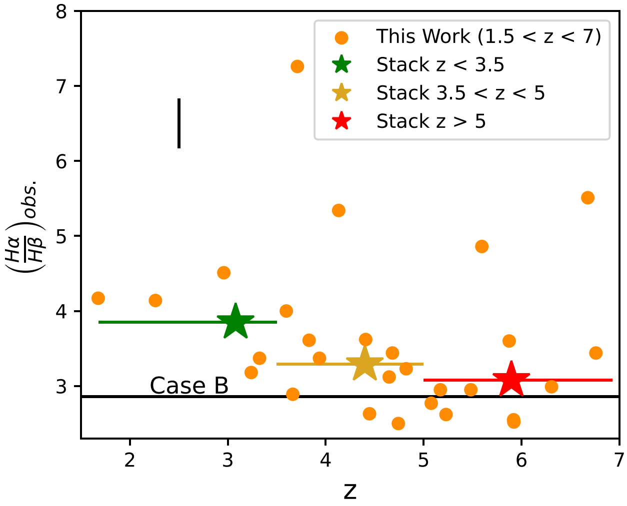

Figure 12. Showcase of the Hα to Hβ ratio evolution for our sample AGN. The orange points show the individual sources with the black bar displaying the median error. Sample stacks are shown as coloured stars placed at the median redshift values of each stack. The y errors on the stacks are smaller than the markers, while the x errors show the width of each stacked bin. The Case B value is shown by the solid black line.

caused by higher redshift sources generally being more metal poor and the [N II] doublet's sensitivity to metallicity, although the magnitude of the decrease shown by the stacks may be overestimated due to blending of weak [N II] with broad Hα. More generally, photoionization models of the NLR of AGN have shown that the decreasing metallicity of the high-z AGN host is indeed expected to result into the steady decrease of both [N II]/Hα and [O III]/β (K. Nakajima & R. Maiolino 2022; H. Übler et al. 2023; R. Maiolino et al. 2024).

A similar, although lesser, effect is seen in the $\mathrm{S2} = \log[\mathrm{SII}]/\mathrm{H}\alpha$ versus R3 diagram (S. Veilleux & D. E. Osterbrock 1987) shown in panel **b** of Fig. 13, where the [S II] doublet gets progressively weaker with redshift (see also J. Scholtz et al. 2023; H. Übler et al. 2023). This offset, while still present, is considerably less extreme in $\mathrm{O1} = \log[\mathrm{OI}]/\mathrm{H}\alpha$ *vs.* R3 (S. Veilleux & D. E. Osterbrock 1987), shown in panel **c** of Fig. 13, and does not show the same consistent evolution with redshift across the stacks. This would indicate that lowering metallicity is a strong contributor to the decrease in effectiveness of the standard emission line diagnostic diagrams, as both nitrogen and sulphur have delayed enrichment with respect to that of oxygen (C. Kobayashi, A. I. Karakas & M. Lugaro 2020).

We also investigate the positions of our sample sources on the He2-N2 diagram from M. Shirazi & J. Brinchmann (2012) and G. Tozzi et al. (2023), which replaces the [O III] in the BPT with He II λ4686, as used in recent *JWST* studies. However, the He II line is robustly detected in only two sources across the entire sample and is otherwise absent even when the spectra are stacked across the full redshift range and individual bins. These stacks yield an upper limit on the He II λ4686 to Hβ ratio of ~ 0.02 and place our sources in the star-forming regions of the He2-N2 diagram (panel **d** of Fig. 13). While the offset on the N2, S2, and O1 BPT diagrams may be attributed to low metallicity (K. Nakajima & R. Maiolino 2022), the absence of metallicity-insensitive high ionization lines (such as He II λ4686) may be indicative of our sample AGN being inefficient at producing high-energy ionizing photons. Whether this inefficiency is intrinsic to the structures of the accretion discs of these AGN and/or is caused by dense gas blanketing the BLR and NLR remains to be investigated (see e.g. K. Inayoshi, S. Kimura & H. Noda 2024; E. Lambrides et al. 2024; P. Madau & F. Haardt 2024; R. Maiolino et al. 2025). It is important to notice that there are also noticeable exceptions; for instance the prominent type 1.8 AGN at z=5.5 studied by H. Übler et al. (2023) and X. Ji et al. (2024) does show clear He II emission, both broad and narrow, despited being totally undetected in deep X-ray data. Additionally, as seen in panel **d** of Fig. 13, some SDSS AGN are similarly weak in He II λ4686 therefore local analogues of this higher redshift population likely exist. It is also important to note that, the scenario of nuclear blanketing of the ionizing radiation would provide an alternative or additional explanation for the offset of our AGN on the BPT diagrams, whereby the AGN ionizing source does not reach the circumnuclear region to form a NLR, hence the observed narrow lines would be dominated by star formation in the host galaxy.

In addition to the traditional strong emission line diagnostics, we also utilize our sample to test some newly proposed AGN diagnostics diagrams, mainly those based on the [O III]λ4363 (G. Mazzolari et al. 2024b) line. Specifically, these authors propose a log[OIII]4363/Hγ (O3Hg) vs log[OIII]5007/[OII]3727 (O3O2) diagram, where they identify a region of high O3Hg populated only by AGN, while other parts of the diagram is populated by both AGN and SF galaxies hence inconclusive. The O32-O3Hg diagram from G. Mazzolari et al. (2024b) with our sample is shown in Fig. 14. As can be seen there, most of our individual sources do not have strong enough detections of the [O III]λ4363 or [O II]λ3727 lines to be reliably classified using this diagnostic. However, all required lines are clearly detected in the stacked spectra. The lowest ($z < 3.5$) stack is largely coincident with the position of the SDSS AGN, while the two $z > 3.5$ stacks showcase strong evolution in [O III]/[O II] ratio going from $z \sim 2$ to $z \sim 4$, which moves both of them slightly beyond the decision boundary and into the region populated by both SFGs and AGN. This weakening of the [O II] relative to the [O III] is likely indicative of more extreme ionization conditions in higher redshift galaxies or lower metallicities (A. J. Cameron et al. 2024). These results indicate that, while the O32-O3Hg diagnostic appears to be more efficient in selecting AGN than the BPT, it still struggles at higher redshifts. It should however be noted that G. Mazzolari et al. (2024b) are quite conservative in defining the boundary identifying the AGN-only region of the diagram, and that the high-z stack would be inconsistent with the envelope of their star-forming photoionization models.

Overall, our investigation of the narrow emission-line diagnostics shows that there is a considerable population of AGN that are unidentifiable by narrow emission lines only. This results in the AGN fraction in galaxy evolution estimated in previous studies (e.g. J. Scholtz et al. 2023; G. Mazzolari et al. 2025) being a lower limit on the overall number of AGN, as there is a considerable number of AGN that can only be identified through broad component in their permitted lines.

8 SHAPES OF THE BROAD EMISSION LINES

Recent works (R. Maiolino et al. 2024; F. D'Eugenio et al. 2025a; V. Rusakov et al. 2025) have found that many AGN found by *JWST* exhibit extended wings in their broad-line profiles that cannot be accommodated by a single Gaussian. V. Rusakov et al. (2025) and D. J. D. Santos et al. (2025a) suggested that these profiles are

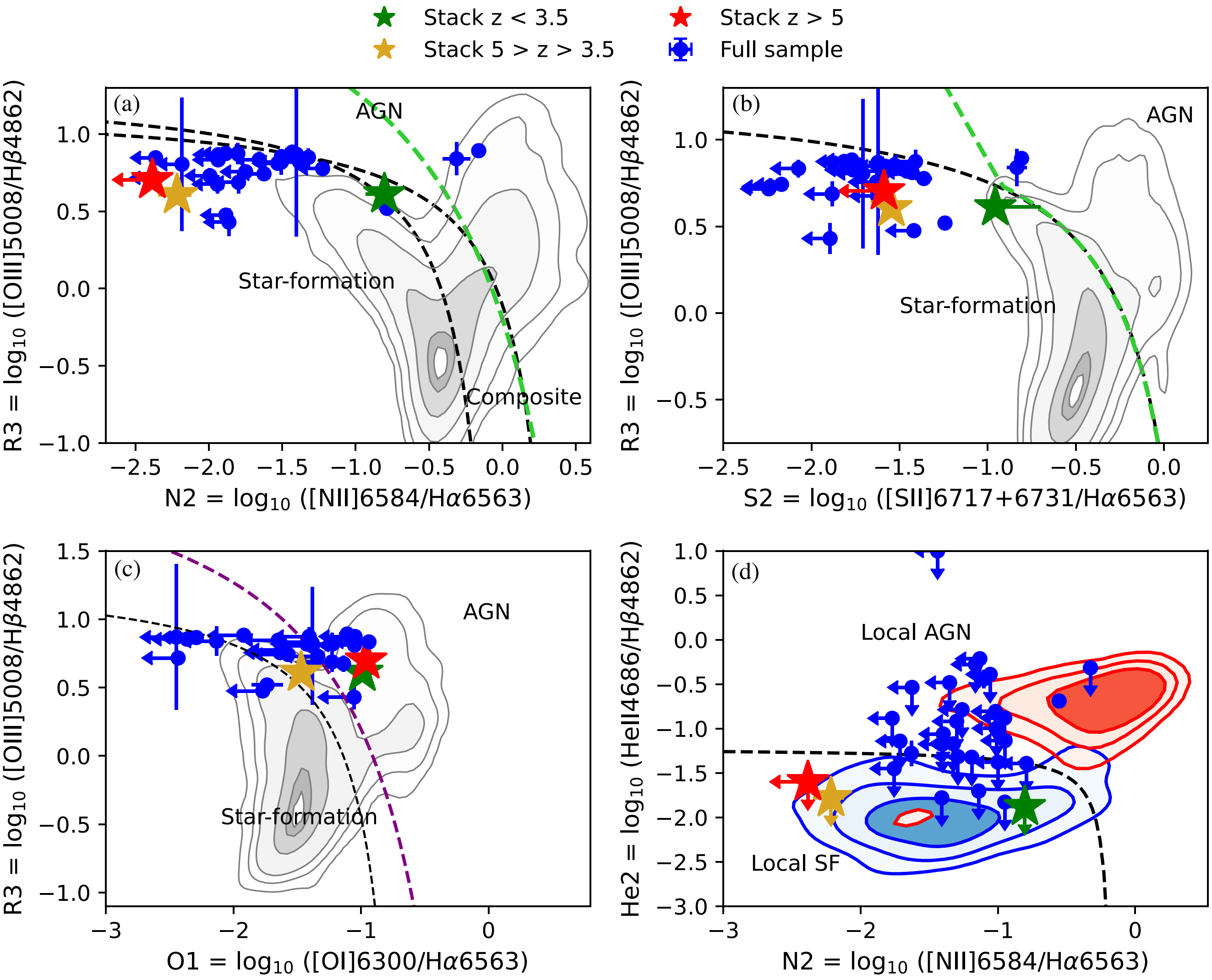

Figure 13. **a.** Showcase of our sample sources (blue circles) and the stacks across the three redshift bins (coloured stars) on the classic BPT diagnostic diagram. The black dashed lines represent the AGN – star-forming demarcation lines from L. J. Kewley et al. (2001) and G. Kauffmann et al. (2003), while the green dashed line is the one used in J. Scholtz et al. (2023) for high-z galaxies. The grey contours are SDSS galaxies. It can be seen that most of our sources lie in the star-forming region due to weak [N II] emission, while the stacked spectra show a strong redshift evolution of the N2 ratio. **b.** Position of our sample sources and stacks on the S2 diagram. The dashed black line is the demarcation from L. J. Kewley et al. (2001), while other symbols have the same meanings as in panel **a**. As in the previous panel, most of our sources lie in the star-forming region of the plot and a significant redshift evolution in the stacks is observed. **c.** Same as panel **b**, but for the O1 diagram with the purple line being the boundary from G. Mazzolari et al. (2025). This diagnostic does not exhibit consistent redshift evolution; however, most of our sources straddle the boundary. **d.** Location of the stacked and individual sample spectra on the He II diagram. SDSS AGN and star-forming galaxies selected through BPT are shown in red and blue contours, respectively. The dashed demarcation line is from M. Shirazi & J. Brinchmann (2012).

exponential in shape and result from Compton scattering in a dense medium. These results would indicate significant overestimation of BH masses and underestimation of accretion rates. However, 'wingy' profiles, not well reproduced by a single Gaussian, have been seen in more generally in most luminous QSOs, where they are well reproduced by either broken power laws, double Gaussians (T. Nagao, A. Marconi & R. Maiolino 2006; W. Kollatschny & M. Zetzl 2013; D. J. D. Santos et al. 2025a) and are largely attributed to the complex internal dynamics of the BLR. If this latter scenario is true, then detecting the more extended wings even in less luminous AGN may be a matter of signal-to-noise. We thus attempt to test these scenarios by exploring the shapes of our Type 1 candidates by investigating the performance of single Gaussian, double Gaussian, and exponential profiles.

We construct the double Gaussian model as a simple superposition of two Gaussians centred on the same wavelength. The widths of the two components were constrained to the same priors as in Section 3. It should be noted that we do not interpret the second Gaussian profile as tracing the presence of a second BH (although this could be the case in some objects, see H. Übler et al. 2024) – this component is introduced to empirically model the extended wings not fit by a single Gaussian. As for the exponential profile, this was constructed following the prescriptions of V. Rusakov et al. (2025) and consisted of an intrinsically Gaussian component, modelling the unscattered BLR emission, convolved

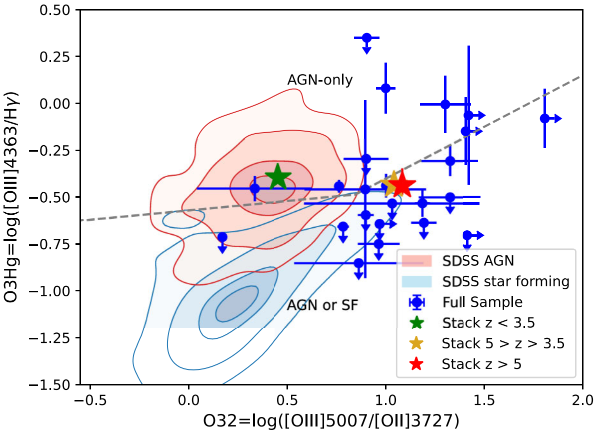

Figure 14. Diagnostic diagram of the [O III]λ4363/Hγ and [O III]λ5007/[O II]λ3727 from G. Mazzolari et al. (2024b). The AGN and star-forming galaxies from SDSS are shown in red and blue contours, respectively. Our sample sources and stacks are shown with blue circles and coloured stars as in Fig. 13. The grey dashed line indicates the boundary between the region populated by AGN only (above it) and the one with a mixture of AGN and star-forming galaxies (below it).

with a broken symmetric exponential of the form

$$N(\lambda_0, B, W) = B\exp(-|\lambda - \lambda_0|/W), \tag{7}$$

where λ_0 is the central wavelength, B the amplitude, and W the e-folding length. The full BLR profile of V. Rusakov et al. (2025) would then have the form

$$f_s N(\lambda) * G(\lambda) + (1 - f_s)G(\lambda), \tag{8}$$

where f_s is the fraction of light scattered, $N(\lambda)$ the scattering exponential from equation (7), and $G(\lambda)$ the intrinsic Gaussian. The prior on the FWHM of the exponential profile (FWHM $\equiv 2W \ln 2$) is the same as that set on the broad Gaussians in the Section 3 fits.

We then refit all of our main sample sources (excluding the six tentative objects) for a total of 28 fitted, with the two models described above and quantify the relative performance using the BIC (equation 1). We find that for most of our sample sources (22) a single-Gaussian fit is preferred. However, six of our sample sources (GS-49729, GN-73488, GN-28074, GS-204851, GS-38562, and GS-159717) exhibit broad wings that cannot be accommodated by a single Gaussian fit (see Fig. 15 for an illustration). For these sources, the double Gaussian and exponential profiles generally fit equally well, with the double Gaussian outperforming the exponential in terms of BIC for 5 of them and performing equally well for the remaining sixth (see Table 7 for a summary). Treating the entire profile of the sources with extended BLR wings as a result of virial broadening does change the BH mass estimates, however, the resulting 0.3–0.4 dex differences are well within the scatter on the virial estimators. In addition, the second Gaussian component in GN-28074 was found by I. Juodžbalis et al. (2024a) to kinematically match an outflow in [O III], thus interpreting it as originating in the BLR is likely inappropriate.

We note that the 6 AGN in Table 7 are among the most luminous in our sample, suggesting that the reason for the apparent simplicity of the remaining broad profiles may be low signal-to-noise. To test this, we stack the objects best-fitted by a single Gaussian profile. The stacking was performed with the same methods as in Section 7. We also stack the objects in Table 7 to obtain further constraints on the shapes of their profiles. The results for each stack are shown in Fig. 16. As shown in the figure, the double Gaussian is strongly preferred over the simple Gaussian or the exponential models for both stacks. Given the diversity in luminosities, BH masses, and line widths of the AGN that ended up in the Gaussian profile stack, there is a possibility of the extended wings being spuriously introduced by stacking faint broad components and brighter, narrower ones. To mitigate this, we experiment with weighting the stacks by the inverse FWHM of the Hα line as well as removing BHs with $M > 10^8$ M$_\odot$ from the stack and find that the feature persists. This result suggests that non-Gaussianity may be intrinsic to the vast majority of AGN BLR and only apparently identified in the brightest QSOs due to S/N constraints. In Fig. 16 (bottom) we also stack those objects for which the single Gaussian fit was not satisfactory, not surprislingly showing broad wings. Interestingly, as shown in the same figure, a fit with a double-Gaussian is preferred relative to the exponential fit in both stacks.

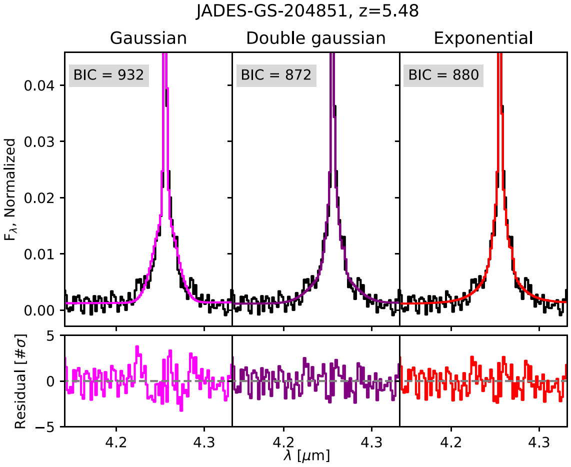

Figure 15. An example comparison of the single Gaussian, double Gaussian, and exponential fits to one of our objects exhibiting extended BLR wings. It can be seen that the single Gaussian model leaves symmetric systematic residuals that are considerably reduced when fitting a double Gaussian or Exponential profiles.

The origin of the broader component is currently unclear—it may be due to the inner part of the BLR (J. W. Sulentic et al. 2002), turbulence in the BLR (W. Kollatschny & M. Zetzl 2013), a combination of rotation and turbulence and/or probing different regions of the BLR (D. J. D. Santos et al. 2025a), or an outflowing component (e.g. J. H. Matthews et al. 2020). Another possibility is that such wings are due to electron scattering, as suggested by A. Laor (2006) and V. Rusakov et al. (2025). The latter actually propose that most of the broad-line profile of *JWST*-selected AGN is produced by electron scattering. However, we discuss in the following section that this scenario is highly unlikely for our sample.

8.1 A scattering origin of the broad lines?

Most models assume that the clouds of the BLR are in virial equilibrium around the BH, with possible contributions from an outflow or inflow component. This assumption is at the basis of the virial relations between BH mass, width (or velocity dispersion) of the permitted broad line and continuum luminosity,

Table 7. Comparison of the BIC values between the three tested models for the sources exhibiting a wingy BLR as well as the BH masses obtained from single and double Gaussian fits. The first column gives the source ID, columns one to three the BIC values for the Gaussian, Double-Gaussian, and Exponential models, respectively. The final two columns list the BH masses obtained from single Gaussian and double Gaussian profiles respectively.

Object ID	$\mathrm{BIC_{Gauss}}$	$\mathrm{BIC_{2Gauss}}$	$\mathrm{BIC_{Exp}}$	$\log M_{BH(\mathrm{Gauss})}$	$\log M_{BH(\mathrm{2Gauss})}$
GS-159717	3766	3559	3857	$7.85^{+0.30}_{-0.30}$	$7.44^{+0.30}_{-0.30}$
GN-73488	901	744	882	$7.95^{+0.30}_{-0.30}$	$7.55^{+0.30}_{-0.30}$
GN-28074	6819	4321	6868	$8.55^{+0.30}_{-0.30}$	$8.09^{+0.30}_{-0.30}$
GS-204851	932	872	880	$7.68^{+0.31}_{-0.32}$	$7.23^{+0.31}_{-0.30}$
GS-38562	839	804	799	$7.53^{+0.31}_{-0.30}$	$7.23^{+0.31}_{-0.30}$
GS-49729	2682	1305	1659	$8.07^{+0.30}_{-0.30}$	$7.67^{+0.30}_{-0.30}$

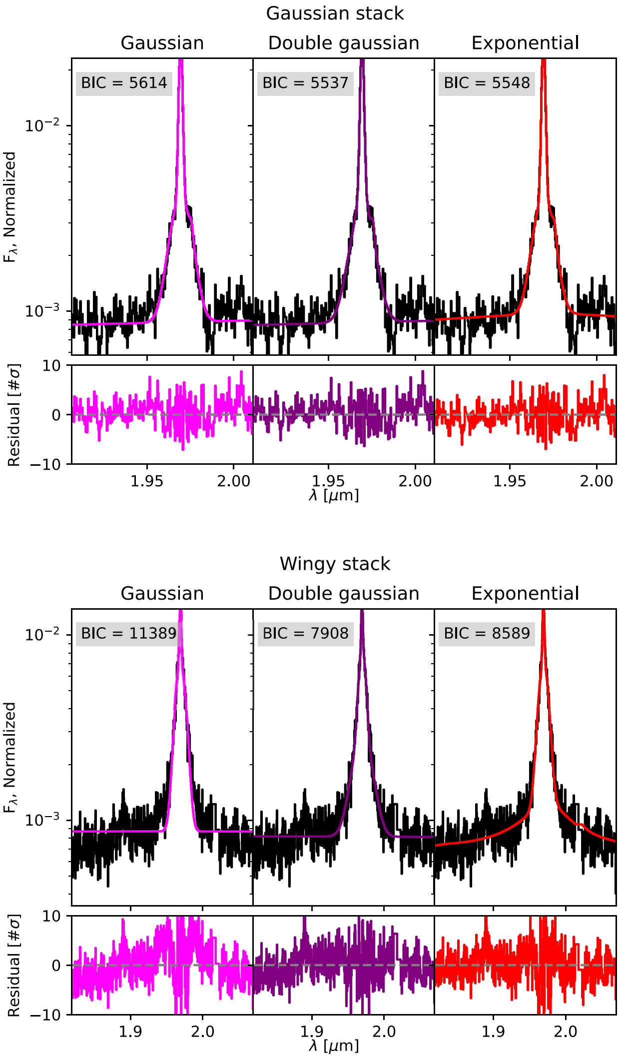

Figure 16. Showcase of the performance of the three models on the stacks of the objects with simple Gaussian profiles (top) and those with extended BLR wings (bottom). The stacks are all redshifted to $z = 2$ and the narrow lines not part of the Hα –[N II] complex are excluded from fitting and BIC calculation. It can be seen that the double Gaussian model is preferred for both stacks.

derived from reverberation mapping (e.g. P. Du et al. 2015, 2018; E. Dalla Bontà et al. 2020; S.-S. Li et al. 2021). This assumption has been verified by comparing these AGN with the BH masses inferred from the M_{BH}–σ_* relation for BHs with direct dynamical measurements (e.g. D. Park et al. 2012; J.-H. Woo et al. 2015).

However, recently V. Rusakov et al. (2025) and R. P. Naidu et al. (2025) have suggested that the observed widths of the broad lines seen in the high-z AGN and LRDs discovered by *JWST* are not tracing the motions of the BLR clouds, but scattering from a medium located outside the BLR. According to their models, the intrinsic width of the broad line would be 5–10 times narrower compared to the observed width, and claim that the observed width is mostly the result of scattering by the outer medium. Given that in the virial relations the mass of the BH scales quadraticaly with the line width, this would imply that the BH masses might be overestimated by about two orders of magnitude. While a more extensive discussion will be presented in a separate paper, in this section, we briefly illustrate that these scenarios are unlikely to apply to the majority of our sample sources.

V. Rusakov et al. (2025) fit the Hα profiles in the high S/N spectra of 13 *JWST*-discovered AGN at z∼3–7. They find that, with the exception of one object, an exponential profile of the broad line is preferred to a single Gaussian (although a double Gaussian fit is not attempted by them). They suggest that this is evidence for an intrinsically very narrow 'broad' Hα associated with the nuclear BLR, which is embedded in an outer ionized medium whose free electrons scatter the line into a much broader exponential profile. In this scenario, the outer ionizing medium embedding the BLR must have a column density of ionized gas on the order of 10^{24} cm^{-2} to explain the observed broad Hα wings in their sample. This scenario has difficulties in explaining our sample, as discussed in the following paragraphs.

The previous section has shown that an exponential profile is not necessarily the best fit – we have seen in our sample that a double-Gaussian profile often fits better the individual profiles and stacks. In addition, as discussed in the previous section, profiles with extended wings that can be approximated with power laws or exponential profiles are commonly seen in many AGN (S. Collin et al. 2006; T. Nagao et al. 2006; W. Kollatschny & M. Zetzl 2013; D. J. D. Santos et al. 2025a), especially those approaching QSO-like luminosities, which include nearby AGN with reverberation studies, which were used to calibrate the virial relations. Therefore, the proposed electron scattering scenario should apply to the a significant fraction of AGN/QSOs, including those used for calibrating the reverberation mapping (S. Collin et al. 2006; E. Dalla Bontà et al. 2020). This would seem to imply that the BH masses are overestimated by orders of magnitude for most

BHs in AGN/QSOs. However, the consistency with the M_{BH}–σ_* relation (D. Park et al. 2012; J.-H. Woo et al. 2015), defined by cases for which the BH mass is measured directly, together with the consistency with direct BH mass measurements in AGN (N. Winkel et al. 2025), excludes that BHs are generally overestimated by orders of magnitude via the virial relations. Moreover, low-z QSOs with 'wingy' profiles are generally not Compton thick to X-ray radiation (which is another prediction of the scattering scenario proposed by V. Rusakov et al. 2025) and exhibit the same X-ray properties as other Type 1 AGN (E. Lusso et al. 2020; R. Maiolino et al. 2025).

Another physical problem that remains to be addressed for the electron scattering scenario is the recombination within the scattering medium. The hypothetical ionized scattering medium located outside the BLR proposed by V. Rusakov et al. (2025) should have a large amount of H^+ ($\sim 10^{24}$ cm^{-2} based on the large N_e from $\tau_{\rm scatter} \sim 1$), therefore producing its own Hα emission, independent of the Hα emission from the BLR that has been scattered. The highly ionized medium located outside the BLR must be photoionized by the same central accretion disc and, in order to explain the ubiquity of the scattering scenario proposed by V. Rusakov et al. (2025), must be nearly entirely covering the BLR (and therefore the accretion disc). However, to allow a significant fraction of ionizing photons to reach such an outer ionized (electron scattering) medium, the covering factor of the inner BLR should be much smaller, or otherwise it would prevent ionizing photons from reaching the outer ionized medium. Both the BLR and the hypothesized outer ionized medium emit Hα via recombination. The width of the Hα emitted by the outer medium is presumably narrower than the Hα intrinsically coming from the BLR, hence it can only be part of the narrow component of Hα (given that in the best-fit models of V. Rusakov et al. 2025 the widths of the BLR lines are typically as narrow as FWHM$_{\rm intrinsic} \lesssim$ 600 km s^{-1}). Meanwhile, in the scenario proposed by V. Rusakov et al. (2025), the Hα coming from BLR is usually not seen directly (only a small fraction of this is transmitted and unscattered), while the bulk of the BLR emission is scattered in the putative exponential wings (i.e. what we see as very broad lines in the *JWST* spectra). To the first order, the ratio of the Hα fluxes of the outer scattering medium (produced by recombination) and the inner BLR is roughly proportional to their covering factor relative to the accretion disc that is responsible for the photoionzation. The covering fraction ratio should be reflected by the occurrence rate of exponential-profile BLR among all BLRs, barring selection effects. In the high S/N sample of V. Rusakov et al. (2025) only one source out of 13 has a broad-line profile dominated by a single Gaussian, while all others are dominated by the exponential wings, hence seen through the putative scattering medium. Therefore, according to the scenario proposed by V. Rusakov et al. (2025), the ratio between the narrow component of Hα (coming from recombination in the proposed scattering medium) and the broad component of Hα (coming from the electron scattering of the BLR) should be at least 12:1. This is completely inconsistent with our observations. Fig. 17 shows the distribution of the narrow-to-broad Hα flux ratio in our sample. All of our AGN have this ratio smaller than eight, and smaller than four for 80 per cent of the sampole. The high S/N sample in V. Rusakov et al. (2025) has a distribution even more skewed towards low values. The vertical dashed line shows the expected value in the scenario proposed by V. Rusakov et al. (2025). This ratio of 12:1 is a lower limit, since the narrow component must also include the standard narrow component from the NLR, Hα emission by star formation in the host, and, in some cases, by the residual emission from the BLR that is transmitted and not scattered.

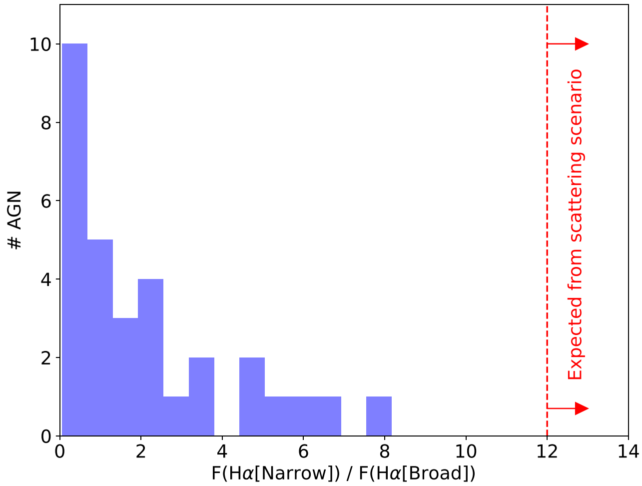

Figure 17. Distribution of the ratio between narrow and broad component of Hα in our sample. The vertical dashed line indicates the lower limit of the ratio expected in the scenario proposed by V. Rusakov et al. (2025) whereby the broad component results from electron scattering of a proposed much narrower BLR component from a hypothetical ionized medium surrounding the BLR.

In addition to the caveats discussed above, the electron scattering scenario appears to require very high ionization to produce $N_e \sim 10^{24}$ cm^{-2}. For reference, A. Laor (2006) inferred an ionization parameter of $\log(U) \sim -0.5$ for the scattering medium of NGC 4395, which has only optically thin scattering with $\tau_{\rm scatter} \approx 0.34$, lower than the typical $\tau_{\rm scatter} \sim 1$ inferred for V. Rusakov et al.'s (2025) sample. Thus, the proposed electron scatter dominated scenario would appear to require $\log(U) \sim 0$, larger than typically inferred for the BLR, despite being at larger distances. Additionally, such a large ionization parameter has implications for the radiation pressure and implications for the stability of such ionized medium, which according to V. Rusakov et al. (2025) should be common to all newly discovered AGN (which are a significant fraction of the whole galaxy population, as discused in the next section). Detailed exploration of this aspect is, however, beyond the scope of this work and will be presented in a separate paper.

R. P. Naidu et al. (2025) proposed a different scattering scenario. In contrast to V. Rusakov et al. (2025), in the R. P. Naidu et al. (2025) scenario the scattering medium is largely neutral, but warm, with $N_{\rm H} \sim 10^{26}$ cm^{-2} and $n_{\rm H} \sim 10^{11}$ cm^{-3}. Such a neutral, warm medium would be responsible for producing a strong Balmer absorption, similarly to the scenario proposed by K. Inayoshi & R. Maiolino (2024) and X. Ji et al. (2025) for LRDs. However, R. P. Naidu et al. (2025) further suggest that the same medium introduces Balmer scattering of Hβ and Hα, analogous to the Lyα scattering in observations, but from hydrogen atoms whose $n = 2$ state is populated by collisional excitation and Lyα trapping. According to the scenario proposed by R. P. Naidu et al. (2025), the intrinsic width of the Balmer lines in the BLR could be much narrower than observed and that the double peaked Balmer line profiles produced by this scattering would resemble Balmer absorption, and give apparent widths much broader than the intrinsic BLR. They propose that this mechanism applies to all LRDs, hence resulting into an overestimation of the BH masses

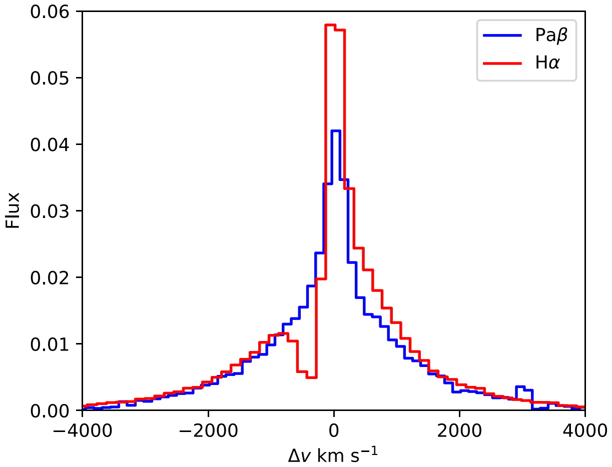

Figure 18. Comparison of the Hα and Paβ line profiles of GN-28074 (I. Juodžbalis et al. 2024a), to evaluate the resonant-scattering scenario. The two lines are shown in velocity space, and have been normalized to the same flux in the wings. In the resonant-scattering scenario of R. P. Naidu et al. (2025), Paβ should have a considerably narrower-line profile than Hα, contrary to observations.

by orders of magnitude. The scenario proposed by R. P. Naidu et al. (2025) can be tested via lower redshift LRDs in our sample, as discussed in the following.

Here we focus specifically on the case of GN-28074 at z=2.3. This object was already presented in I. Juodžbalis et al. (2024a) as a more luminous ‘Rosetta Stone’ for understanding higher-z LRDs. This object presents broad permitted lines, a Balmer break, and absorption of Hα and Hβ (and HeIλ10830), which I. Juodžbalis et al. (2024a) demonstrate requires absorption by gas with densities $n > 10^9\ cm^{-3}$. The same mechanism likely occurs in most LRDs (K. Inayoshi & R. Maiolino 2024; X. Ji et al. 2025), including the source presented in R. P. Naidu et al. (2025). However, the detection of bright Paschen lines in GN-28074 offers the possibility of testing the Balmer scattering scenario proposed by R. P. Naidu et al. (2025). If the broad wings observed in Hα and Hβ were due to Balmer scattering of a much narrower BLR line, then the same wings should not be seen in Paβ, which would mostly be tracing the intrinsic BLR emission. In the R. P. Naidu et al. (2025) scenario the population of n=3 of hydrogen is much lower than n=2, even in the case of high temperatures and densities (making the population of levels thermalized in a Maxwellian distribution), hence making the column density of hydrogen atoms in the n=3 state much smaller than n=2. This should make the wings seen in the Balmer lines not observable in Paβ and make it much narrower than Hα or Hβ, due to the much smaller cross-section of Paschen scattering. However, the Paβ line of GN-28074 shows prominent broad wings and an overall similar shape to Hα. This is illustrated in Fig. 18 where the Hα and Paβ profiles of GN-28074 are overlaid, after normalizing them to the same flux of the wings. Paβ does not show evidence of absorption – this is expected in the simpler scenario proposed by I. Juodžbalis et al. (2024a), X. Ji et al. (2025), and K. Inayoshi & R. Maiolino (2024), in which the high density in the absorbing medium populates n=2, but not n=3 levels. However, the most important feature is the presence of broad wings of Paβ – as shown by the figure, Paβ has proportionally more flux in the wings than Hα, in contradiction to what is expected by the Balmer scattering scenario. A more extensive analysis of this source arriving at the same conclusion is presented in M. Brazzini et al. (2025).

Finally, if the BH masses were overestimated by two orders of magnitude, this would certainly help to bring them down to the local M_{BH}–M_{star} relation. However, since they are located close to the local M_{BH}–σ relation (Section6.2), reducing their BH mass by two orders of magnitude would make them severely undermassive on the latter relation, which is considered more fundamental and universal (J. Kormendy & L. C. Ho 2013; A. B. Newman et al. 2025).

In summary, both the electron scattering and Balmer scattering scenarios for explaining the broad wings of the Balmer lines appear untenable for the vast majority of our objects, although they may apply to a few rare cases. Therefore, there is no evidence that the BH masses have been systematically overestimated by orders of magnitude as proposed by V. Rusakov et al. (2025) and R. P. Naidu et al. (2025).

9 UV LUMINOSITY FUNCTION OF AGN AND THEIR HOSTS

We utilize the increased statistical power afforded by the expanded sample to estimate the contribution of Type 1 AGN and their hosts to the UV luminosity function (LF) at $4 < z < 7$ (note that this redshift bin is slightly wider and extended to higher redshift than the $4 < z < 6$ one used in the previous work by R. Maiolino et al. 2024). The total number densities of AGN hosts were estimated by rescaling the galaxy UVLF at z = 6 from R. J. Bouwens et al. (2021) by the ratios of number of AGN hosts to that of star-forming galaxies spectroscopically targeted by JADES in each magnitude bin. As JADES primarily targeted star-forming UV-bright galaxies, our background galaxy sample is strongly biased against quiescent hosts. However, this bias is unlikely to be significant as high redshift galaxies are generally star-forming (P. Popesso et al. 2023).

The UV magnitude bins were chosen to include roughly the same amount of AGN hosts and were centred on $M_{UV} = -18.375$, $M_{UV} = -18.975$, and $M_{UV} = -19.8$ with the brightest bin introduced to include a small subset of UV bright AGN. We find that AGN make up 5 per cent, 9 per cent, and 2 per cent of all galaxies in corresponding magnitude bins although these values are likely lower limits due to our conservative sample selection. The source counts are 7, 9, and 4 for the faintest, medium, and brightest bins, respectively. The overall UVLF estimate is plotted as green points in Fig. 19. While our sample statistics are not constraining enough to obtain a reasonable fit to a functional form, rescaling the R. J. Bouwens et al. (2021) results down to 6 per cent can reasonably reproduce the densities observed in the two fainter bins. The brightest bin, however, sits significantly below this rescaled curve and may indicate a steepening of the UVLF of faint AGN hosts relative to the bright population, however, statistics there are small.

Overall, our sample contains 20 AGN at $4 < z < 7$, almost double the amount published in R. Maiolino et al. (2024). This allows us to explore variations in number density estimates due to cosmic variance. We investigate cosmic variance first, by splitting our sample across GOODS-S and GOODS-N fields. Both fields end up containing 10 AGN at the redshift range considered thus any variation in bin densities is due to variance in galaxy counts per field and the AGN UV luminosity. As shown in the left panel of Fig. 19, GOODS-N field contains an excess of faint AGN when

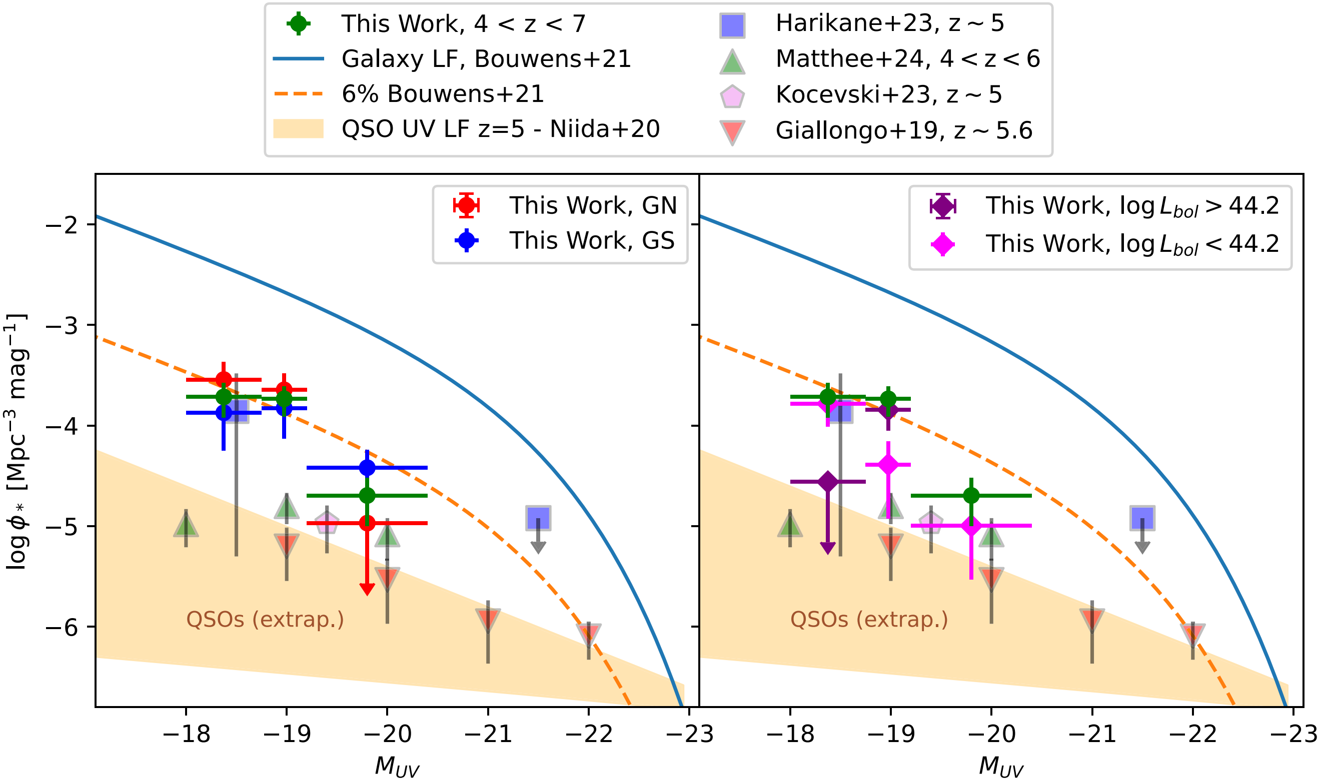

Figure 19. UVLF of our Type 1 AGN hosts between $z = 4$ and $z = 7$. Density estimates for the whole sample are shown with green points. The left panel shows the variance in the LF when the sample is split across the two fields – GN and GS with red and blue points, respectively. The right panel shows results from a split in L_{bol} with high- and low-luminosity bins shown in purple and magenta diamonds, respectively. The highest MUV bin contains the same amount of sources across both L_{bol} ranges thus the points overlap. The solid blue line shows the galaxy LF at $z \sim 5$ from R. J. Bouwens et al. (2021), while the dashed orange line shows the same LF scaled down to 6 per cent. The orange shaded region shows the range of extrapolated QSO LFs from M. Niida et al. (2020). Results from X-ray AGN studies by E. Giallongo et al. (2019) are shown in orange triangles. The remaining points showcase results from other *JWST* surveys as indicated in the legend.

compared to GOODS-S. On the contrary, GOODS-S has more sources at higher M_{UV} relative to GOODS-N. Clearly, these differences highlight that cosmic variance plays an important role in the number density and luminosity distribution of AGN in small fields and can affect the statistics by at least a factor of a few. This also highlights that the evolutionary patterns of AGN (as imprinted in the luminosity function) are likely different in different environments and different primeval conditions.

Fig. 19 also showcases a comparison between our results (the numerical values for which are given in Table 8; Y. Harikane et al. 2023; D. D. Kocevski et al. 2023; J. Matthee et al. 2024) and those from QSOs (M. Niida et al. 2020) and X-ray AGN (E. Giallongo et al. 2019) surveys together with results from the first years of *JWST* observations (Y. Harikane et al. 2023; D. D. Kocevski et al. 2024; J. Matthee et al. 2024). We find that density estimates lie significantly above the extrapolated QSO luminosity functions as well as those from X-ray based AGN surveys (Fig. 19) as found by R. Maiolino et al. (2024) for a subsample of our sources. Our estimated AGN fractions, however, are somewhat lower than theirs, with AGN hosts contributing about 6 per cent of galaxy density, as opposed to ~10 per cent found by R. Maiolino et al. (2024). This could likely be attributed to an increase in the number of galaxy spectra taken by the JADES survey along with an expanded (and higher) redshift range considered here. However, confirming that the UV luminosity function of the newly discovered AGN is one or two orders of magnitude higher than the extrapolation of QSOs, indicated that *JWST* is likely uncovering a new population of AGN possibly formed through a different route. Additionally, confirming that the new population of AGN is much more numerous than X-ray-selected AGN is in line with the finding that they are X-ray weak (R. Maiolino et al. 2025) and that X-ray surveys have likely found only the tip of the iceberg of the population, either less (X-ray) absorbed or intrinsically more X-ray loud.

In order to investigate the variance of the UVLF with varying AGN bolometric luminosity, we split our sample into high ($L_{bol} > 10^{44.2}$ erg s^{-1}) and low ($L_{bol} < 10^{44.2}$ erg s^{-1}) luminosity halves, containing 10 sources each. The resulting density estimates are shown in the right panel of Fig. 19. As it is shown there, the differences in the luminous end ($M_{\rm UV} < -19.5$) are not drastic with the brightest MUV bins completely overlapping, while the high luminosity ($\log L_{bol} > 44.2$) sample contains far fewer sources in the faintest M_{UV} bin. This may indicate some level of contribution of AGN emission to the UV magnitude for more luminous AGN or a correlation between *Lbol* and SFR of the host, which brightens the UV luminosity of the hosts of luminous AGN and 'depletes' the lowest UV luminosity bin. However the discrepancy between the luminosity bins is not large. This indicates that the AGN component is either subdominant due to low accretion rates, as is clearly exemplified by

Table 8. Summary of the UVLF measurements shown in Fig. 19. The first two columns list the central MUV of each magnitude bin and the bin width respectively. Column three shows the number densities of the entire AGN sample, fourth and fifth column shown the number densities split across GOODS-N and GOODS-S fields while the final two columns show the number densities across the high ($\log L_{bol} > 44.2$) and low ($\log L_{bol} < 44.2$) luminosity bins. All number densities are given in units of Mpc^{-3} mag^{-1}.

$M_{\rm UV}$	$\Delta M_{\rm UV}$	$\log\phi_{\rm All}$	$\log\phi_{\rm GN}$	$\log\phi_{\rm GS}$	$\log\phi_{\rm HiLum}$	$\log\phi_{\rm LoLum}$
-18.375	0.375	$-3.72^{+0.14}_{-0.2}$	$-3.54^{+0.18}_{-0.30}$	$-3.87^{+0.20}_{-0.37}$	$< -4.56^{+0.30}$	$-3.78^{+0.15}_{-0.23}$
-18.975	0.225	$-3.73^{+0.12}_{-0.18}$	$-3.64^{+0.16}_{-0.26}$	$-3.83^{+0.18}_{-0.30}$	$-3.84^{+0.14}_{-0.21}$	$-4.39^{+0.23}_{-0.53}$
-19.8	0.6	$-4.70^{+0.18}_{-0.30}$	$< -4.97^{+0.30}$	$-4.42^{+0.18}_{-0.30}$	$-5.00^{+0.23}_{-0.53}$	$-5.00^{+0.23}_{-0.53}$

GN-38509 (I. Juodžbalis et al. 2024b) or due to their UV emission being weak. Dust obscuration provides a tempting explanation for this weakness; however, most of our sources, with the exception of GN-209777, show low to moderate attenuation ($0 < A_V < 2.0$) of the NLR and host galaxy. Thus either the dust is concentrated towards the BLR or the AGN have intrinsically red SEDs if the lack of AGN contribution to the UV emission is to be explained by a physical deficiency in UV photons.

We conclude by mentioning that our updated UV luminosity function confirms that AGN and their hosts can potentially contribute to the reionization of the Universe, although a more quantitative assessment requires a proper disentangling between AGN and host galaxy contribution to the observed UV radiation, and should also take into account of the cosmic variance revealed by our study (S. Asthana et al. 2024; P. Dayal et al. 2024; A. Grazian et al. 2024; P. Madau et al. 2024); such an analysis is beyond the scope of this paper.

10 CONCLUSIONS

In this paper we have presented a robust sample of Type 1 AGN spanning redshifts from $z = 1.7$ to $z = 7$ with the tentative broad Hβ emitters reaching $z = 9$, enabling us to probe AGN from Cosmic Noon to the Epoch of Reionization. The luminosity regime investigated is > 2 dex fainter than that of all-sky QSO surveys and about ~ 0.5 dex below that of other *JWST* AGN surveys. Thus our sample presents a deep view into the low-luminosity regime of AGN activity. It should be noted that only $\sim$30 per cent of our sample sources exhibit LRD like spectra (K. N. Hainline et al. 2025) thus, while LRDs make up a significant fraction of the Type 1 AGN population, most Type 1 AGN are not LRDs.

The low luminosities of most of our AGN sample allow for reasonable estimates of the stellar masses of their hosts. Most BHs in our sample are significantly overmassive with respect to the local M_{BH}–$Mstar$ relations, with the highest excess occurring at $z > 5$, while all AGN at $z < 3.5$ are consistent with the local M_{BH}–M_* scaling relation (although our statistics in the lower redshift regime are less constraining). This is nevertheless indicative of the local M_{BH}–M_* relation being established at $z < 4$, consistent with the findings of some BH growth models (A. Trinca et al. 2024) and observational work by Y. Sun et al. (2025).

When comparing our BH masses to the inferred stellar velocity dispersions of each of our sources, we find that all our objects, irrespective of redshift, are consistent with local scaling relations. For a subsample we could also infer the dynamical mass of the host galaxy, and finding also in this case that our sources are consistent with the local M_{BH}–M_{dyn} relation. This suggests that most of the gas required to bring our sources to agreement with the local scaling relations is likely already present, but star formation is being inhibited by AGN feedback. Alternatively, the dynamical mass of these early systems could be dark matter dominated. However, both of these scenarios require additional testing in simulations. In addition, the lack of a significant, offset relative to local M_{BH}–σ_* and M_{BH}–M_{dyn} relations (Fig. 6) suggests that the overmassive nature of BHs at high redshifts can not be ascribed entirely to selection effects although these are certainly present (I. Juodžbalis et al. 2024b; J. Li et al. 2025a).

Comparison of the NLR of our AGN to the $L_{H\beta}$–σ relation from J. Melnick et al. (2017) shows no significant deviation between them and star-forming galaxies. This is suggestive of a lack of turbulent or ejective feedback present in our sample AGN and implies that star formation in our sources is likely inhibited through heating of the gas.

Our evaluation of different narrow-line diagnostics reveals that no single narrow-line diagnostic method is capable of selecting a complete and pure sample of Type II AGN at high redshifts. The [O III]λ4363 diagnostics from G. Mazzolari et al. (2024b) are promising in terms of purity; however, their completeness suffers at higher redshift due to weakening of the [O II]λ3727 with respect to [O III]λ5007.

The lack of He II λ4686 or any other high ionization line emission in our sources, even in the stacked spectra, is curious and indicates a deficiency in high-energy photons reaching the NLR. This may be connected to the relative prevalence of Balmer absorption features of *JWST*-discovered broad-line AGN (I. Juodžbalis et al. 2024a; J. Matthee et al. 2024; B. Wang et al. 2024), which traces high-density gas surrounding their nuclei. This gas, in addition to producing Balmer absorption lines, could likely attenuate UV emission by bound–free absorption from n=1 and n=2 states of hydrogen, reducing the ionizing photon budget and potentially leading to non-stellar Balmer breaks as theoretically shown by K. Inayoshi & R. Maiolino (2024) and demonstrated observationally by X. Ji et al. (2025) and R. P. Naidu et al. (2025). However, more in-depth studies investigating the prevalence of Balmer absorption lines in low-luminosity Type 1 AGN as well as follow-up observations exploring their nature are needed to robustly establish this scenario.

We also investigated the recent claims that the broad lines observed in the *JWST*-discovered AGN are driven by electron scattering by an ionized medium (V. Rusakov et al. 2025), or Balmer scattering by a neutral medium (R. P. Naidu et al. 2025) around the BLR. In these scenarios the intrinsic width of Hα produced by the BLR would be much narrower than observed. As a consequence, the BH masses estimated via the virial relations applied to the observed width would have been systematically overestimated by orders of magnitude. We have shown that both of these scattering effects do not contribute significantly to the BLR line widths for the majority of our sample sources. A more complete analysis of the physical implications of these scenarios is deferred to a future paper.

Lastly, we have assessed the UV luminosity function of the AGN in our sample and their host galaxies. We confirm that these

AGN are at least one to two orders of magnitude more abundant than the extrapolation of luminous QSOs and X-ray-selected AGN. This suggests that *JWST* is uncovering a different population, possibly formed through different processes and is in line with the finding that they are X-ray weak (R. Maiolino et al. 2025). Moreover, our abundance estimates are likely lower limits due to conservative sample selection. We found substantial cosmic variance, by a factor of a few, between GOODS-S and GOODS-N, which should be taken into account when assessing the fraction of AGN in the early Universe. We also find a dependence of the UV luminosity function on the AGN bolometric luminosity, which should also be taken into account when assessing their space density.

ACKNOWLEDGEMENTS

This work is based on observations made with the NASA/ESA/CSA *James Webb Space Telescope*. The data were obtained from the Mikulski Archive for Space Telescopes at the Space Telescope Science Institute, which is operated by the Association of Universities for Research in Astronomy, Inc., under NASA contract NAS 5-03127 for *JWST*. These observations are associated with program 1180, 1181, 1210, 1286, and 3215. This work was performed using resources provided by the Cambridge Service for Data Driven Discovery (CSD3) operated by the University of Cambridge Research Computing Service (www.csd3.cam.ac.uk), provided by Dell EMC and Intel using Tier-2 funding from the Engineering and Physical Sciences Research Council (capital grant EP/T022159/1), and DiRAC funding from the Science and Technology Facilities Council (www.dirac.ac.uk). IJ acknowledges support by the Huo Family Foundation through a P.C. Ho PhD Studentship. RM, IJ, JS, FDE, and GCJ acknowledge support by the Science and Technology Facilities Council (STFC), by the ERC through Advanced Grant 695671 'QUENCH', and by the UKRI Frontier Research grant RISEandFALL. RM also acknowledges funding from a research professorship from the Royal Society. WMB gratefully acknowledges support from DARK via the DARK fellowship. This work was supported by a research grant (VIL54489) from VILLUM FONDEN. ECL acknowledges support of an STFC Webb Fellowship (ST/W001438/1). YI is supported by JSPS KAKENHI Grant No. 24KJ0202. ST acknowledges support by the Royal Society Research Grant G125142. AJB acknowledges funding from the 'FirstGalaxies' Advanced Grant from the European Research Council (ERC) under the European Union's Horizon 2020 research and innovation programme (Grant agreement No. 789056). SC, GV, and BT acknowledge support by European Union's HE ERC Starting Grant No. 101040227 – WINGS. MP acknowledges support from the research project PID2021-127718NB-I00 of the Spanish Ministry of Science and Innovation/State Agency of Research (MICIN/AEI/10.13039/501100011033), and the Programa Atracción de Talento de la Comunidad de Madrid via grant 2018-T2/TIC-11715. BER acknowledges support from the NIRCam Science Team contract to the University of Arizona, NAS5-02015, and *JWST* Program 3215. HÜ acknowledges funding by the European Union (ERC APEX, 101164796). Views and opinions expressed are however those of the authors only and do not necessarily reflect those of the European Union or the European Research Council Executive Agency. Neither the European Union nor the granting authority can be held responsible for them.

DATA AVAILABILITY

The data used in this study has been made public on the *JWST* DAWN archive as part of JADES DR3. The catalogue table can be provided by the corresponding author upon reasonable request.

REFERENCES

Abuter R. et al., 2024, Nature, 627, 281
Allen N. et al., 2025, A&A, 698, A30
Ananna T. T., Bogdán Á., Kovács O. E., Natarajan P., Hickox R. C., 2024, ApJ, 969, L18
Asthana S., Haehnelt M. G., Kulkarni G., Bolton J. S., Gaikwad P., Keating L. C., Puchwein E., 2025, MNRAS, 542, 2968
Bañados E. et al., 2018, Nature, 553, 473
Backhaus B. E. et al., 2025, ApJ, 994, 125
Baker W. M. et al., 2025a, A&A, 702, A270
Baker W. M. et al., 2025b, preprint (arXiv:2509.09761)
Baker W. M. et al., 2025c, Nat. Astron., 9, 141
Baker W. M. et al., 2025d, MNRAS, 539, 557
Baker W. M. et al., 2025e, A&A, 697, A90
Baldwin J. A., Phillips M. M., Terlevich R., 1981, PASP, 93, 5
Belli S. et al., 2024, Nature, 630, 54
Bennert V. N. et al., 2021, ApJ, 921, 36
Bertemes C. et al., 2025, A&A, 693, A176
Bezanson R. et al., 2018, ApJ, 868, L36
Bongiorno A. et al., 2014, MNRAS, 443, 2077
Boquien M., Burgarella D., Roehlly Y., Buat V., Ciesla L., Corre D., Inoue A. K., Salas H., 2019, A&A, 622, A103
Bouwens R. J. et al., 2021, AJ, 162, 47
Brazzini M., D'Eugenio F., Maiolino R., Juodžbalis I., Ji X., Scholtz J., 2025, MNRAS, 544, L167
Bromm V., Loeb A., 2003, ApJ, 596, 34
Brooks M. et al., 2024, ApJ, 986, 177
Bruzual G., Charlot S., 2003, MNRAS, 344, 1000
Bugiani L. et al., 2025, ApJ, 981, 25
Bunker A. J., NIRSPEC Instrument Science Team, JAESs Collaboration, 2020, in da Cunha E., Hodge J., Afonso J., Pentericci L., Sobral D., eds, Proc. IAU Symp. 352, Uncovering Early Galaxy Evolution in the ALMA and JWST Era. Kluwer, Dordrecht, p. 342
Bunker A. J. et al., 2023, A&A, 677, A88
Bunker A. J. et al., 2024, A&A, 690, A288
Bushouse H. et al., 2022, JWST Calibration Pipeline, Zenodo, https://doi.org/10.5281/zenodo.7229890
Calzetti D., Armus L., Bohlin R. C., Kinney A. L., Koornneef J., Storchi-Bergmann T., 2000, ApJ, 533, 682
Cameron A. J., Katz H., Witten C., Saxena A., Laporte N., Bunker A. J., 2024, MNRAS, 534, 523
Capelo P. R., Dotti M., Volonteri M., Mayer L., Bellovary J. M., Shen S., 2017, MNRAS, 469, 4437
Carnall A. C., 2017, preprint (arXiv:1705.05165)
Carnall A. C. et al., 2023, Nature, 619, 716
Carnall A. C. et al., 2024, MNRAS, 534, 325
Carniani S. et al., 2024, A&A, 685, A99
Charlot S., Fall S. M., 2000, ApJ, 539, 718
Chávez R., Terlevich R., Terlevich E., Bresolin F., Melnick J., Plionis M., Basilakos S., 2014, MNRAS, 442, 3565
Chevallard J., Charlot S., 2016, MNRAS, 462, 1415
Coil A. L. et al., 2015, ApJ, 801, 35
Collin S., Kawaguchi T., Peterson B. M., Vestergaard M., 2006, A&A, 456, 75
Combes F., 2023, preprint (arXiv:2302.12917)
D'Eugenio F. et al., 2024, Nat. Astron., 8, 1443
D'Eugenio F. et al., 2025a, ApJS, 277, 4
D'Eugenio F. et al., 2025b, preprint (arXiv:2503.11752)
D'Eugenio F. et al., 2026, MNRAS, 545, staf2117

Dale D. A., Helou G., Magdis G. E., Armus L., Díaz-Santos T., Shi Y., 2014, ApJ, 784, 83
Dalla Bontà E. et al., 2020, ApJ, 903, 112
Davies M. B., Miller M. C., Bellovary J. M., 2011, ApJ, 740, L42
Dayal P. et al., 2025, A&A, 697, A211
Dekel A., Burkert A., 2014, MNRAS, 438, 1870
Ding X. et al., 2023, Nature, 621, 51
Dojčinović I., Kovačević-Dojčinović J., Popović L. Č., 2023, Adv. Space Res., 71, 1219
Dorner B., 2012, Theses, Université Claude Bernard – Lyon I, https://theses.hal.science/tel-00738070 (Accessed Feb 2026)
Du P. et al., 2015, ApJ, 806, 22
Du P. et al., 2018, ApJ, 856, 6
Eisenstein D. J. et al., 2023, preprint (arXiv:2306.02465)
Emami N. et al., 2021, ApJ, 922, 217
Fan X., Bañados E., Simcoe R. A., 2023, ARA&A, 61, 373
Feltre A., Charlot S., Gutkin J., 2016, MNRAS, 456, 3354
Foreman-Mackey D., Hogg D. W., Lang D., Goodman J., 2013, PASP, 125, 306
Furtak L. J. et al., 2024, Nature, 628, 57
Getachew-Woreta T., Pović M., Masegosa J., Perea J., Beyoro-Amado Z., Márquez I., 2022, MNRAS, 514, 607
Giallongo E. et al., 2019, ApJ, 884, 19
Gilli R. et al., 2022, A&A, 666, A17
Gordon K. D., Clayton G. C., Misselt K. A., Landolt A. U., Wolff M. J., 2003, ApJ, 594, 279
Goulding A. D. et al., 2023, ApJ, 955, L24
de Graaff A. et al., 2024, A&A, 684, A87
Grazian A. et al., 2024, ApJ, 974, 84
Greene J. E., Strader J., Ho L. C., 2020, ARA&A, 58, 257
Greene J. E. et al., 2024, ApJ, 964, 39
Hainline K. N. et al., 2025, ApJ, 979, 138
Harikane Y. et al., 2023, ApJ, 959, 39
Harrison C. M., Ramos Almeida C., 2024, Galaxies, 12, 17
Ilić D., Popović L. Č., La Mura G., Ciroi S., Rafanelli P., 2012, A&A, 543, A142
Inayoshi K., Maiolino R., 2025, ApJ, 980, L27
Inayoshi K., Kimura S., Noda H., 2024, PASJ, 77, 811
Isobe Y. et al., 2025, MNRAS, 541, L71
Ji X. et al., 2024, MNRAS, 535, 881
Ji X. et al., 2025, MNRAS, 544, 3900
Juodžbalis I. et al., 2024a, MNRAS, 535, 853
Juodžbalis I. et al., 2024b, Nature, 636, 594
Kaasinen M., Bian F., Groves B., Kewley L. J., Gupta A., 2017, MNRAS, 465, 3220
Kauffmann G. et al., 2003, MNRAS, 346, 1055
Kelly B. C., Merloni A., 2012, Adv. Astron., 2012, 970858
Kewley L. J., Heisler C. A., Dopita M. A., Lumsden S., 2001, ApJS, 132, 37
Kobayashi C., Karakas A. I., Lugaro M., 2020, ApJ, 900, 179
Kocevski D. D. et al., 2017, ApJ, 846, 112
Kocevski D. D. et al., 2023, ApJ, 954, L4
Kocevski D. D. et al., 2025, ApJ, 986, 126
Kokorev V. et al., 2023, ApJ, 957, L7
Kokorev V. et al., 2024, ApJ, 975, 178
Kollatschny W., Zetzl M., 2013, A&A, 549, A100
Kormendy J., Ho L. C., 2013, ARA&A, 51, 511
Kroupa P., Subr L., Jerabkova T., Wang L., 2020, MNRAS, 498, 5652
Lagos C. d. P. et al., 2025, MNRAS, 536, 2324
Lambrides E. et al., 2024, preprint (arXiv:2409.13047)
Laor A., 2006, ApJ, 643, 112
Li J. et al., 2025a, ApJ, 981, 19
Li J., Shen Y., Zhuang M.-Y., 2025b, preprint (arXiv:2502.05048)
Li S.-S. et al., 2021, ApJ, 920, 9
Looser T. J. et al., 2024, Nature, 629, 53
Luo Y., Ardaneh K., Shlosman I., Nagamine K., Wise J. H., Begelman M. C., 2018, MNRAS, 476, 3523
Luridiana V., Morisset C., Shaw R. A., 2015, A&A, 573, A42
Lusso E. et al., 2013, ApJ, 777, 86
Lusso E. et al., 2020, A&A, 642, A150
Lyu J., Alberts S., Rieke G. H., Rujopakarn W., 2022, ApJ, 941, 191
Madau P., Haardt F., 2024, ApJ, 976, L24
Madau P., Giallongo E., Grazian A., Haardt F., 2024, ApJ, 971, 75
Maiolino R. et al., 2024, A&A, 691, A145
Maiolino R. et al., 2025, MNRAS, 538, 1921
Man A., Belli S., 2018, Nat. Astron., 2, 695
Masters D. et al., 2014, ApJ, 785, 153
Matthee J. et al., 2024, ApJ, 963, 129
Matthews J. H., Knigge C., Higginbottom N., Long K. S., Sim S. A., Mangham S. W., Parkinson E. J., Hewitt H. A., 2020, MNRAS, 492, 5540
Mazzolari G. et al., 2024a, preprint (arXiv:2412.04224)
Mazzolari G. et al., 2024b, A&A, 691, A345
Mazzolari G. et al., 2025, A&A, 700, A12
Mazzucchelli C. et al., 2023, A&A, 676, A71
McClymont W. et al., 2025, MNRAS, 544, 513
McClymont W. et al., 2026, MNRAS, 545, staf2092
Melnick J. et al., 2017, A&A, 599, A76
Merloni A. et al., 2010, ApJ, 708, 137
Miller T. B. et al., 2025, ApJ, 988, 196
Nagao T., Marconi A., Maiolino R., 2006, A&A, 447, 157
Naidu R. P. et al., 2025, preprint (arXiv:2503.16596)
Nakajima K., Maiolino R., 2022, MNRAS, 513, 5134
Nakajima K., Ouchi M., Isobe Y., Harikane Y., Zhang Y., Ono Y., Umeda H., Oguri M., 2023, ApJS, 269, 33
Nanayakkara T. et al., 2025, ApJ, 981, 78
Negrete C. A., Dultzin D., Marziani P., Sulentic J. W., 2012, ApJ, 757, 62
Netzer H., Lira P., Trakhtenbrot B., Shemmer O., Cury I., 2007, ApJ, 671, 1256
Newman A. B. et al., 2025, preprint (arXiv:2503.17478)
Niida M. et al., 2020, ApJ, 904, 89
Osterbrock D. E., Ferland G. J., 2006, Astrophysics of Gaseous Nebulae and Active Galactic Nuclei. University Science Books, New York, p. 480
Park D., Kelly B. C., Woo J.-H., Treu T., 2012, ApJS, 203, 6
Park M. et al., 2024, ApJ, 976, 72
Pei Y. C., 1992, ApJ, 395, 130
Planck Collaboration VI, 2020, A&A, 641, A6
Popesso P. et al., 2023, MNRAS, 519, 1526
Pović M. et al., 2012, A&A, 541, A118
Reines A. E., Volonteri M., 2015, ApJ, 813, 82
Renzini A., 2025, MNRAS, 536, L8
Rieke M., 2020, in da Cunha E., Hodge J., Afonso J., Pentericci L., Sobral D., eds, Proc. IAU Symp. 352, Uncovering Early Galaxy Evolution in the ALMA and JWST Era. Kluwer, Dordrecht, p. 337
Robertson B. E. et al., 2023, Nat. Astron., 7, 611
Rusakov V. et al., 2026, Nature, 659, 574
Sales L. V., Navarro J. F., Theuns T., Schaye J., White S. D. M., Frenk C. S., Crain R. A., Dalla Vecchia C., 2012, MNRAS, 423, 1544
Sandles L. et al., 2024, A&A, 691, A305
Santos D. J. D. et al., 2025a, A&A, 696, A30
Scarlata C., Hayes M., Panagia N., Mehta V., Haardt F., Bagley M., 2024, preprint (arXiv:2404.09015)
Schneider R., Valiante R., Trinca A., Graziani L., Volonteri M., Maiolino R., 2023, MNRAS, 526, 3250
Scholtz J. et al., 2025, A&A, 697, A175
Shakura N. I., Sunyaev R. A., 1973, A&A, 24, 337
Shirazi M., Brinchmann J., 2012, MNRAS, 421, 1043
Silva-Lima L. A., Martins L. P., Coelho P. R. T., Gadotti D. A., Gonçalves G., 2023, in Galactic Bars: Driving and Decoding Galaxy Evolution. p. 55
Smith A. et al., 2022, MNRAS, 517, 1
Stalevski M., Ricci C., Ueda Y., Lira P., Fritz J., Baes M., 2016, MNRAS, 458, 2288
Stern J., Laor A., 2012, MNRAS, 423, 600
Stone M. A., Lyu J., Rieke G. H., Alberts S., Hainline K. N., 2024, ApJ 964, 90
Storchi-Bergmann T., Schnorr-Müller A., 2019, Nat. Astron., 3, 48

Strait V. et al., 2023, ApJ, 949, L23
Sulentic J. W., Marziani P., Zamanov R., Bachev R., Calvani M., Dultzin-Hacyan D., 2002, ApJ, 566, L71
Sun Y., Rieke G. H., Lyu J., Stone M. A., Ji Z., Rinaldi P., Willmer C. N. A., Zhu Y., 2025, ApJ 983, 165
Tacchella S., Dekel A., Carollo C. M., Ceverino D., DeGraf C., Lapiner S., Mandelker N., Primack Joel R., 2016, MNRAS, 457, 2790
Tacchella S. et al., 2023, ApJ, 952, 74
Taylor A. J. et al., 2025, ApJ, 986, 165
Tozzi G., Maiolino R., Cresci G., Piotrowska J. M., Belfiore F., Curti M., Mannucci F., Marconi A., 2023, MNRAS, 521, 1264
Trefoloni B. et al., 2025, A&A, 700, A203
Trinca A., Schneider R., Valiante R., Graziani L., Zappacosta L., Shankar F., 2022, MNRAS, 511, 616
Trinca A. et al., 2024, preprint (arXiv:2412.14248)
Übler H. et al., 2023, A&A, 677, A145
Übler H. et al., 2024, MNRAS, 531, 355
Valentino F. et al., 2025, A&A, 699, A358
van der Wel A. et al., 2022, ApJ, 936, 9
Vanden Berk D. E. et al., 2001, AJ, 122, 549
Veilleux S., Osterbrock D. E., 1987, ApJS, 63, 295
Vestergaard M., Peterson B. M., 2006, ApJ, 641, 689
Vijarnwannaluk B. et al., 2022, ApJ, 941, 97
Wang B. et al., 2025, ApJ, 984, 121
Wang F. et al., 2020, ApJ, 896, 23
Winkel N. et al., 2025, ApJ, 978, 115
Woo J.-H., Yoon Y., Park S., Park D., Kim S. C., 2015, ApJ, 801, 38
Yue M., Eilers A.-C., Ananna T. T., Panagiotou C., Kara E., Miyaji T., 2024a, ApJ, 974, L26
Yue M. et al., 2024b, ApJ, 966, 176
Zappacosta L. et al., 2023, A&A, 678, A201
Zhao R. J., Furlanetto S. R., 2024, J. Cosmol. Astropart. Phys., 2024, 018

APPENDIX A: FITS AND SPECTRA OF THE SAMPLE AGN

Here we present the Hα fits to all sources in our sample not presented in the main text.

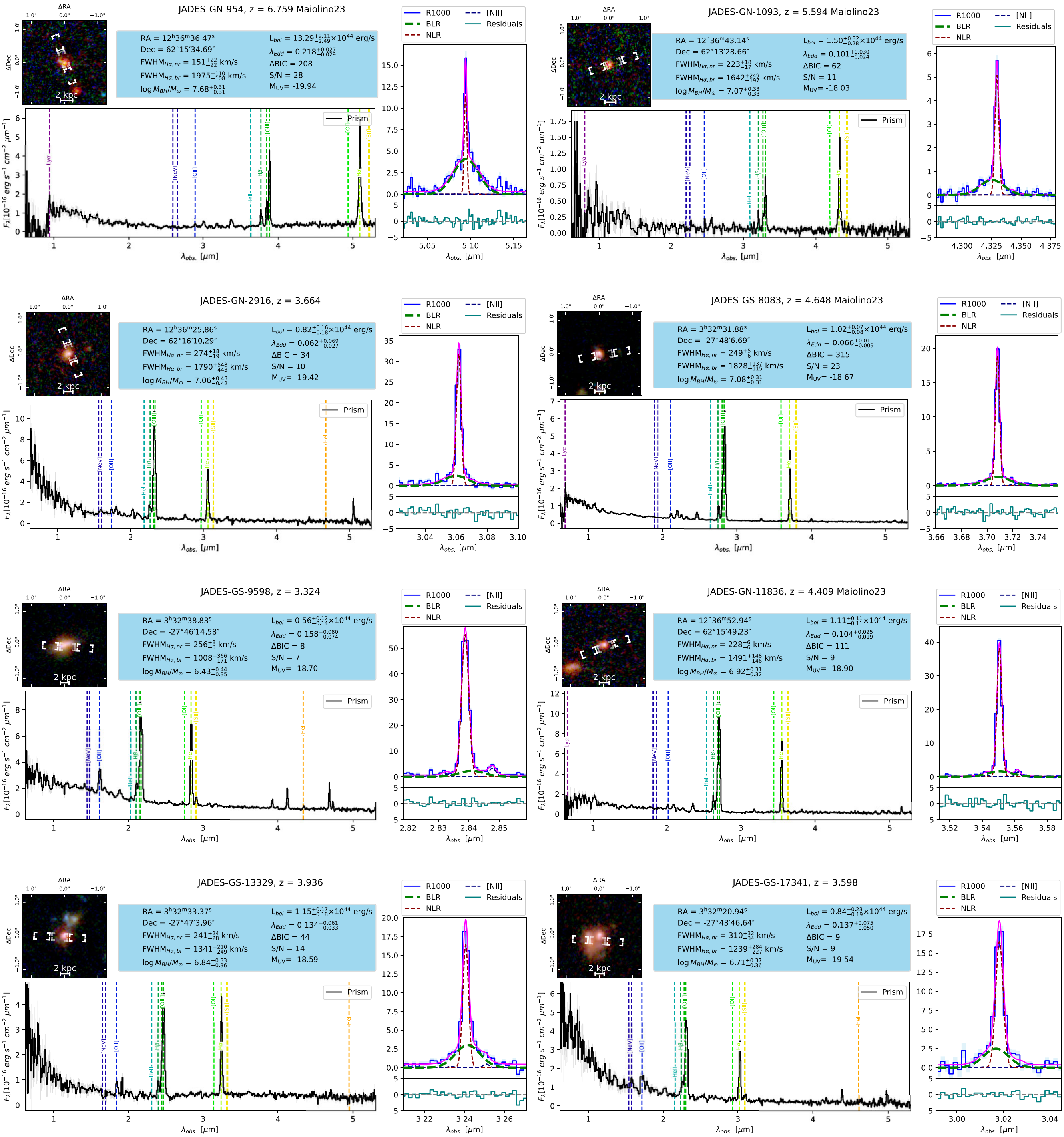

Figure A1. Same structure as Fig. 1 in the main text.

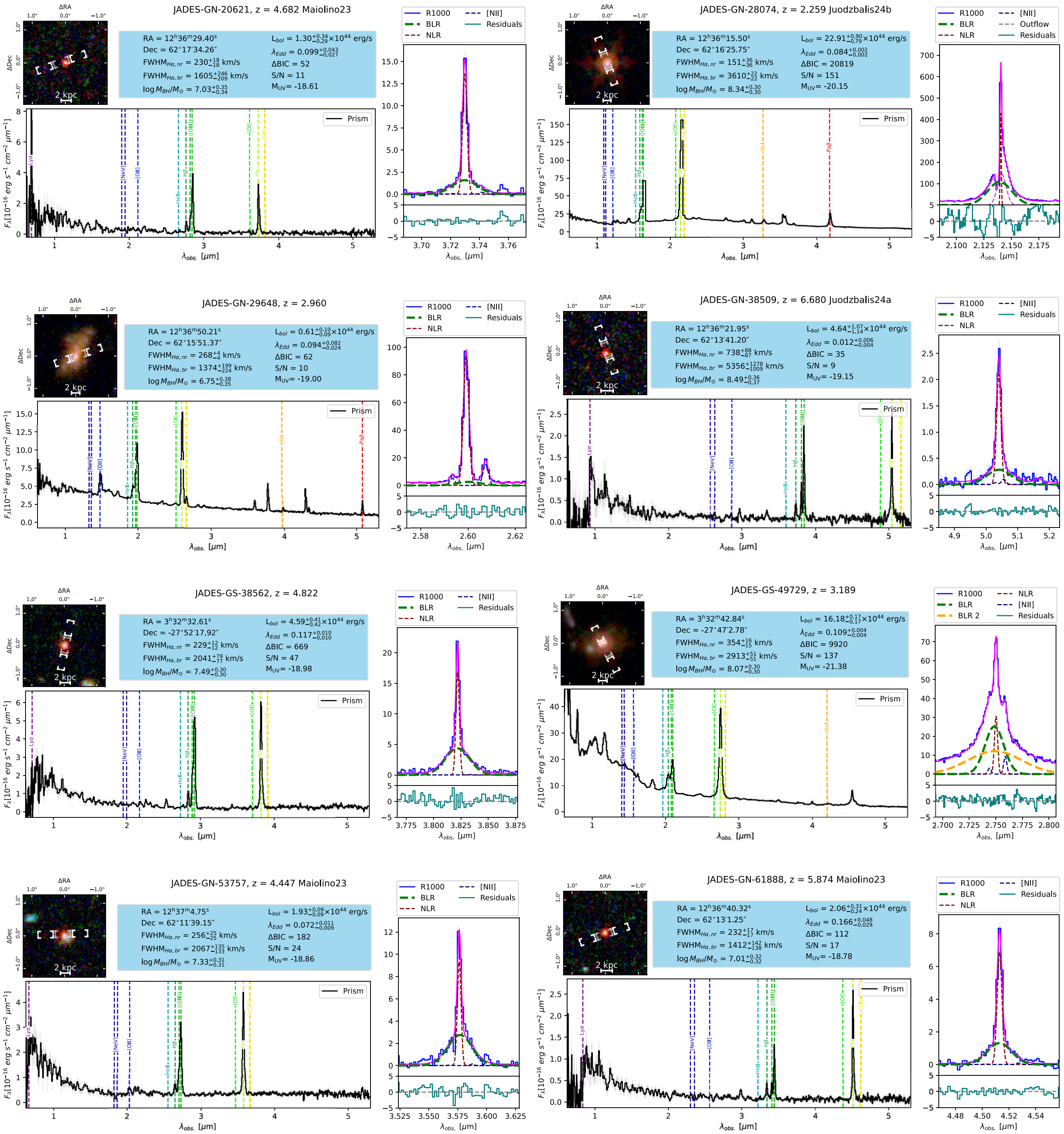

Figure A2. Same structure as Fig. 1 in the main text.

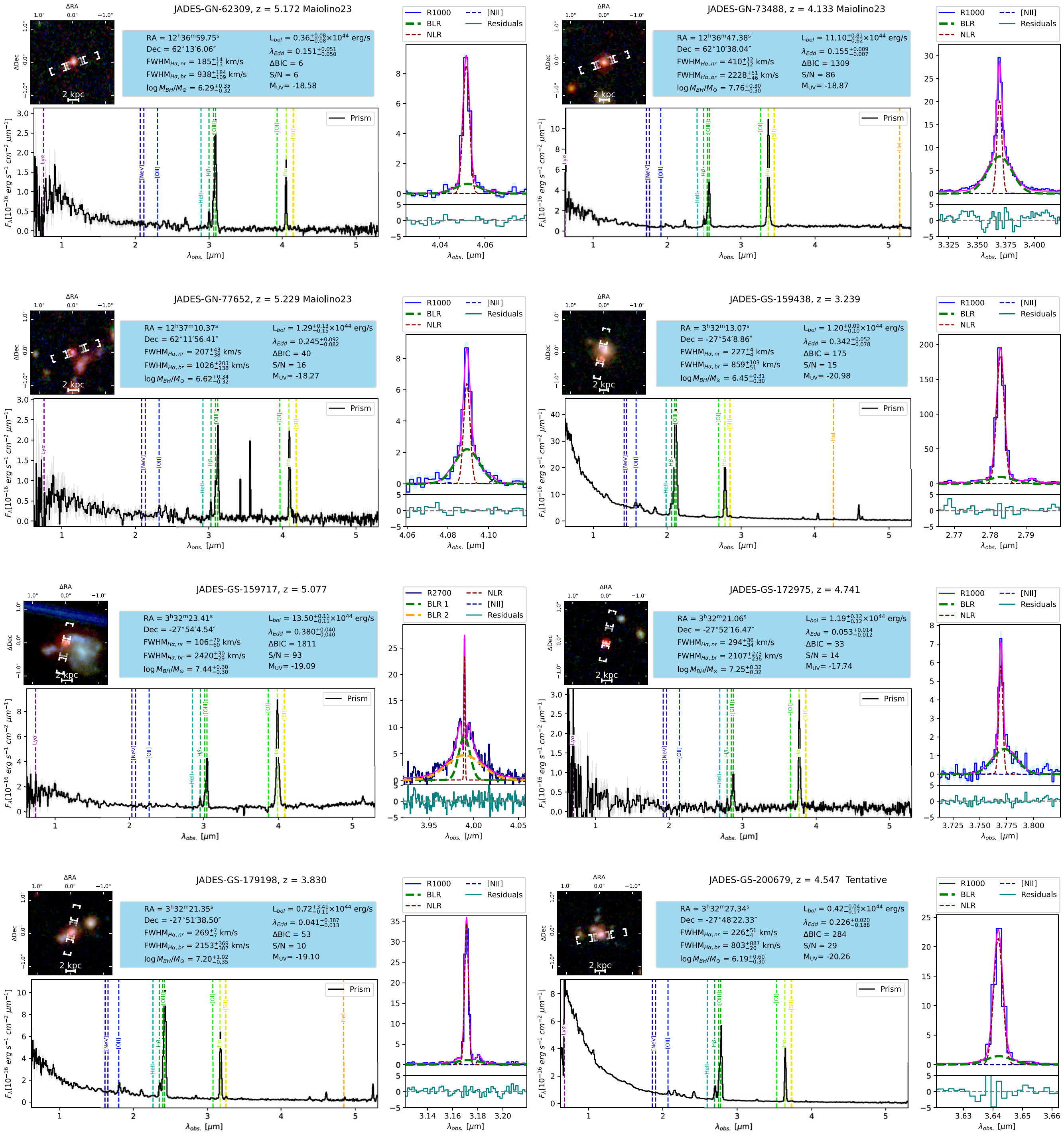

Figure A3. Same structure as Fig. 1 in the main text.

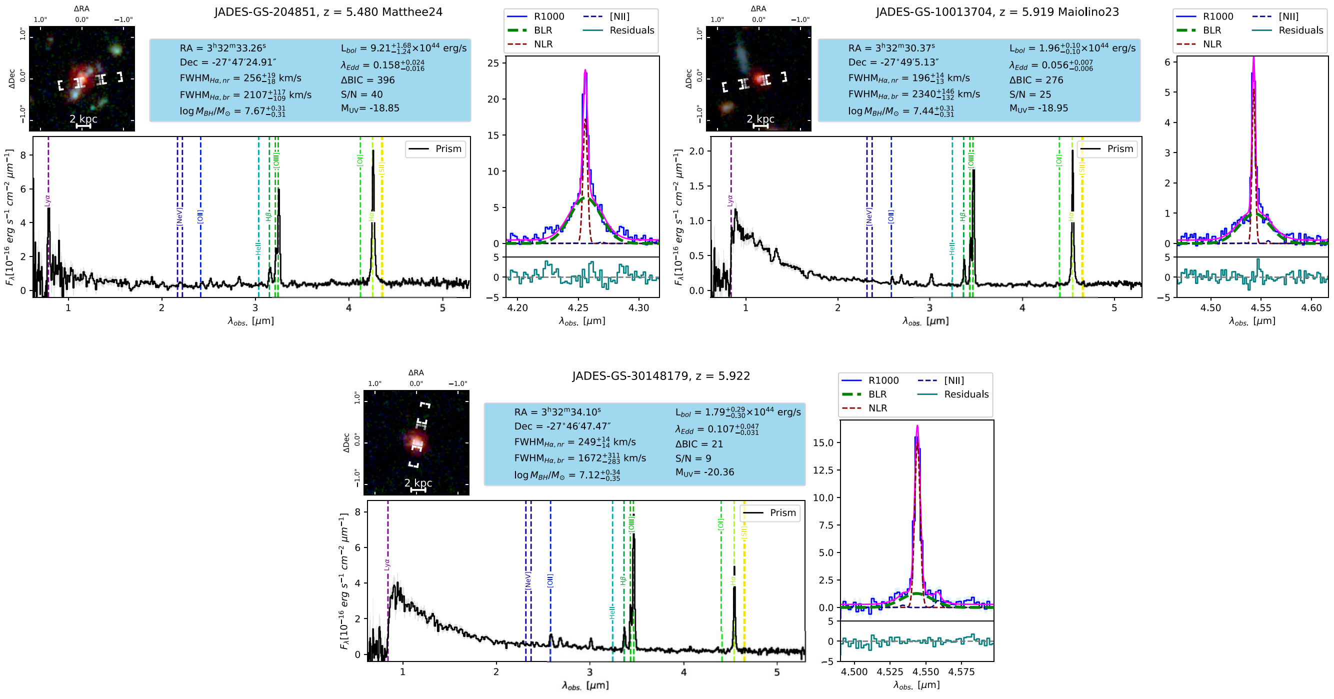

Figure A4. Same structure as Fig. 1 in the main text.

APPENDIX B: TENTATIVE BROAD Hβ EMITTERS

In this section we present the individual and stacked spectra of the four sources with tentative broad Hβ emission. The individual spectra are shown in Fig. B1 and display visually broad, but not formally significant Hβ profiles. A stack of these spectra (Fig. B2), however, does show a prominent broad Hβ profile. Lastly, the NIRCam cut-outs for these sources are shown in Fig. B3 and reveal their compact nature.

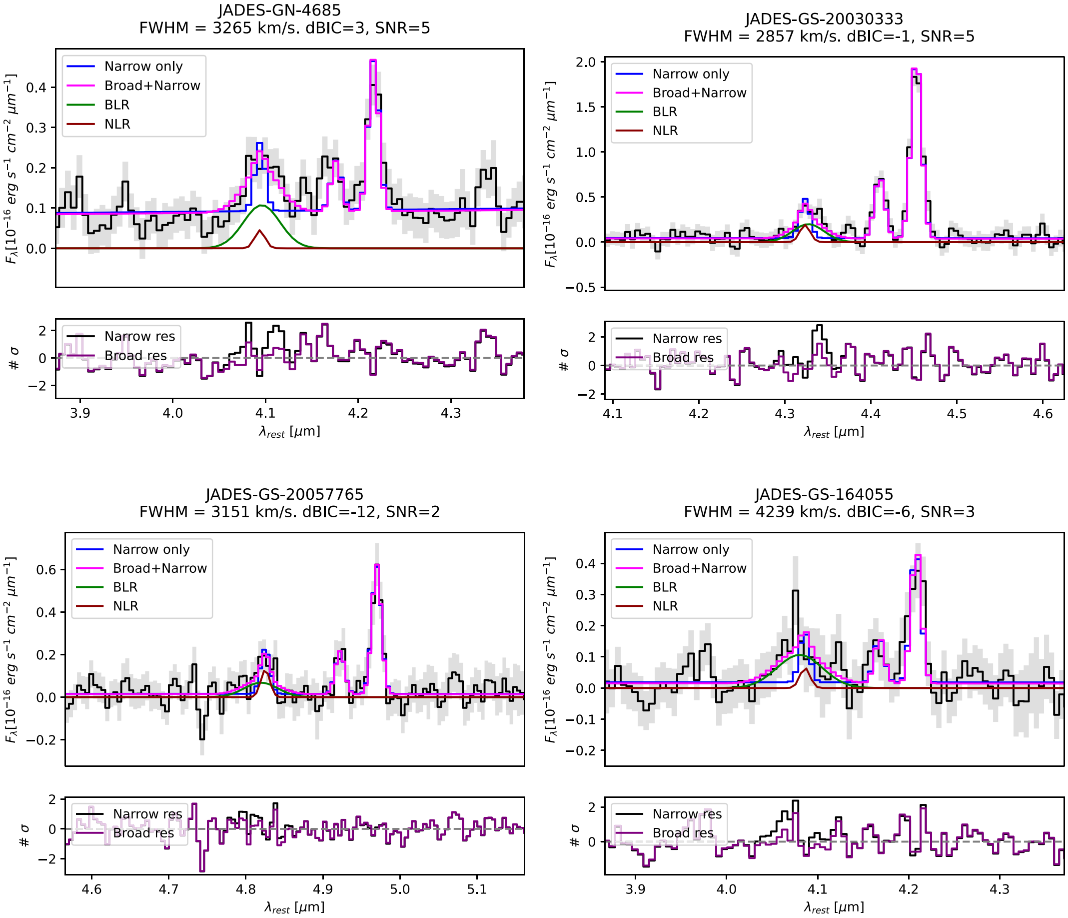

Figure B1. Showcase of the individual spectra of the tentative broad Hβ emitters. The narrow-line-only fit is shown in blue, while the solid magenta line shows the fit including a broad Hβ component. The BLR and NLR components of the broad-line fit are shown in green and dark red, respectively. The lower panel beneath each spectrum shows the residuals of the two fits. It can be seen that, while the narrow-line-only fit does leave larger residuals, they are not significant enough to include these objects in our main sample.

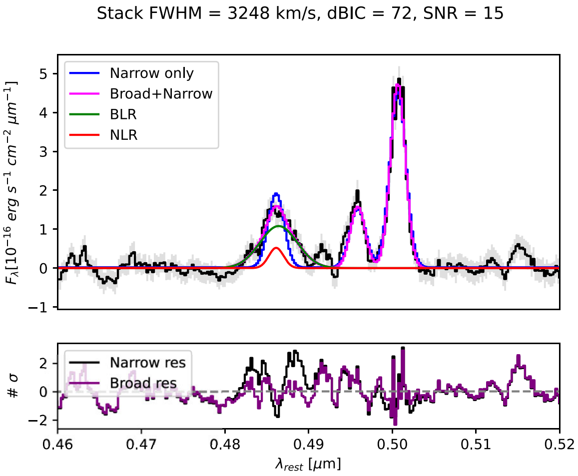

Figure B2. Stacked continuum-subtracted spectrum of the four objects visually identified to have broad Hβ in prism. The plot is organized the same as the individual ones in Fig. B1. It can be seen that not including a broad line in the fit leaves significant symmetric wings in the residual. In addition, the narrow-line fit would result in a [O III]/Hβ ratio of 3, uncharacteristically low for these high-redshift objects.

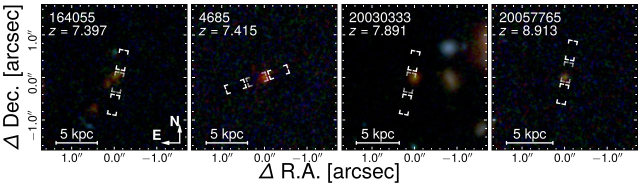

Figure B3. RGB NIRCam cut-outs of the tentative broad Hβ emitters. The shutter position is indicated in white rectangles. The images clearly showcase the compact LRD-like nature of these sources. However, GS-164055 does appear to be an interacting system.

APPENDIX C: ΔBIC AND S/N DISTRIBUTION OF THE PARENT SAMPLE

Here we present the distribution of ΔBIC and S/N values across the fitted parent sample, illustrating the number of sources removed by our selection criteria (Fig. C1).<?pgbrk fill ?>

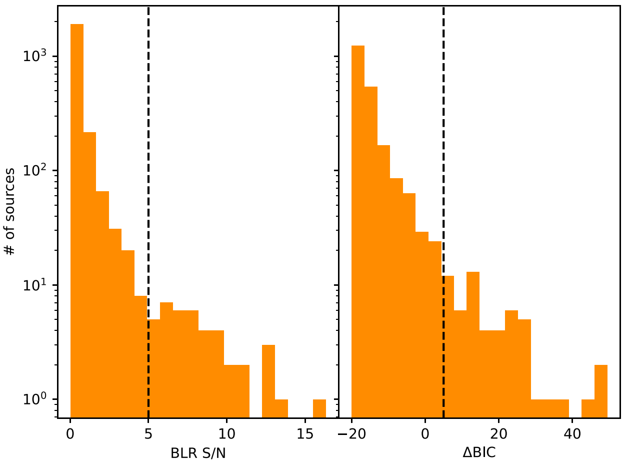

Figure C1. Distribution of the parent sample sources across the range of best-fitting S/N values of the BLR (left) and ΔBIC (right). The vertical dashed line indicates the selection cuts used in this work.

APPENDIX D: OUTFLOWS IN OUR SAMPLE AGN

We note that most of our sample sources display narrow [O III]λ, λ4959,5007 lines, uncontaminated by the presence of outflows. While a detailed exploration into the energetics of the detected outflows is beyond the scope of this work, we show the Hβ+[O III] fits for the sources with significant outflows, which are GS-49729, GS-209777, and GN-23924 (Fig. D1). While GN-28074 also has outflow detections, a detailed exploration of the line shapes of this object is already published in I. Juodžbalis et al. (2024a) and M. Brazzini et al. (2025).

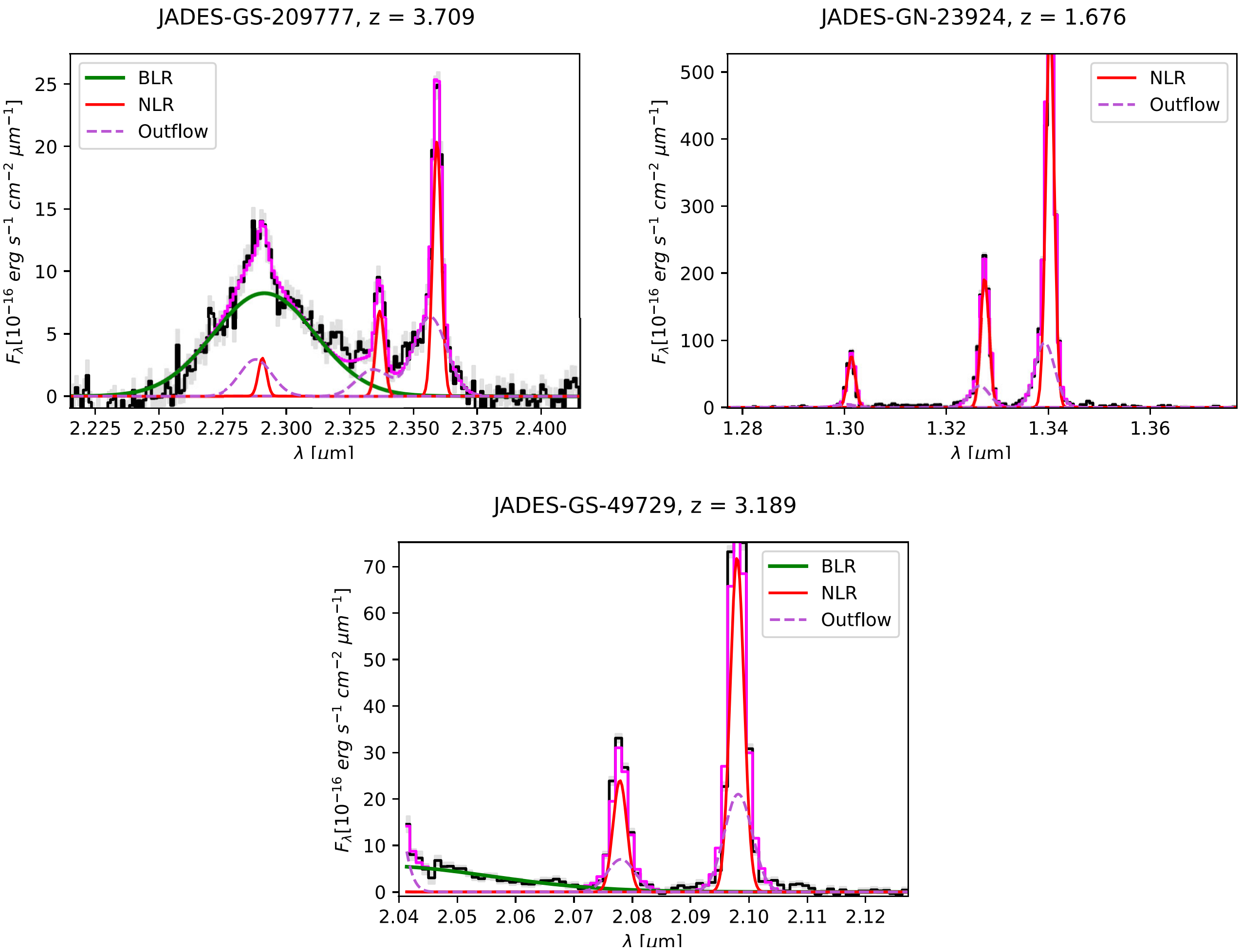

JADES-GS-209777, z = 3.709

JADES-GN-23924, z = 1.676

JADES-GS-49729, z = 3.189

Figure D1. Fits to the continuum-subtracted Hβ+[O III] complex for the sources with significant outflow detections. The narrow lines are shown in red, broad lines (if present) – green and outflow components – violet. The magenta line shows the combined best fit. For GS-49729 (bottom), most of the Hβ line is in the detector gap and could not be recovered.

APPENDIX E: EXAMPLE BEST-FITTING SEDS AND DUST ATTENUATION COMPARISON

In this section we present some examples of successful and unsuccessful SED fitting results (Fig. E1). Fig. E2 shows the comparison between A_V derived from line fitting and BEAGLE SED fits. While BEAGLE A_V is quite uncertain for the majority of the sources, reflecting the uncertainties in fitting stellar continua to AGN, a subset of sources shows continuum A_V considerably larger than the values given by the Balmer decrement. However, all sources in that region are LRDs for which the mismatch between continuum attenuation inferred from standard SED fitting and line A_V signifies the non-setallar nature of their optical continuum (X. Ji et al. 2025; R. P. Naidu et al. 2025).

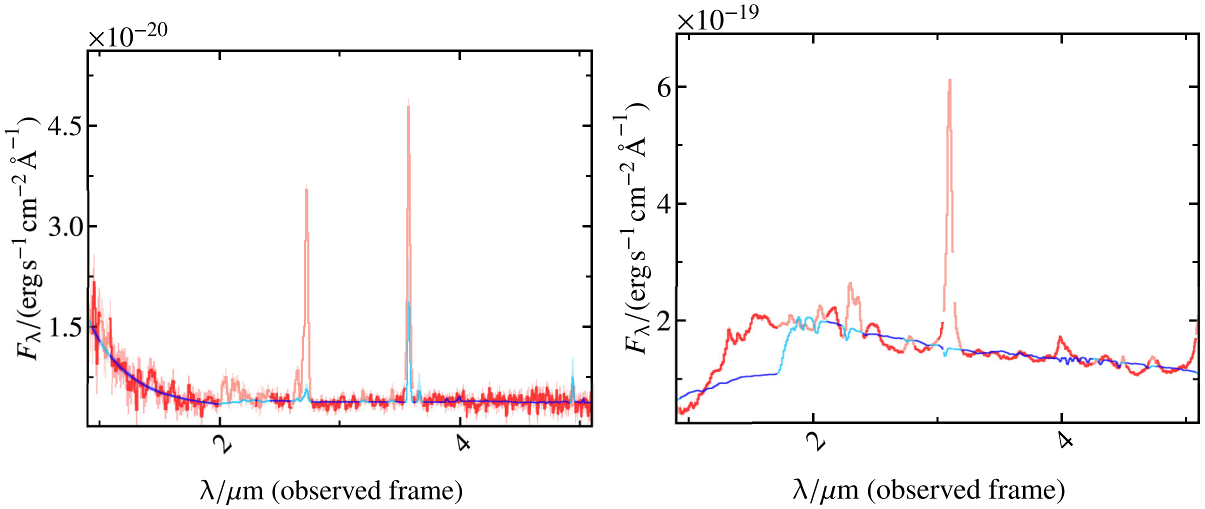

(a) GN-53757, `BEAGLE`

(b) GS-209777, `BEAGLE`

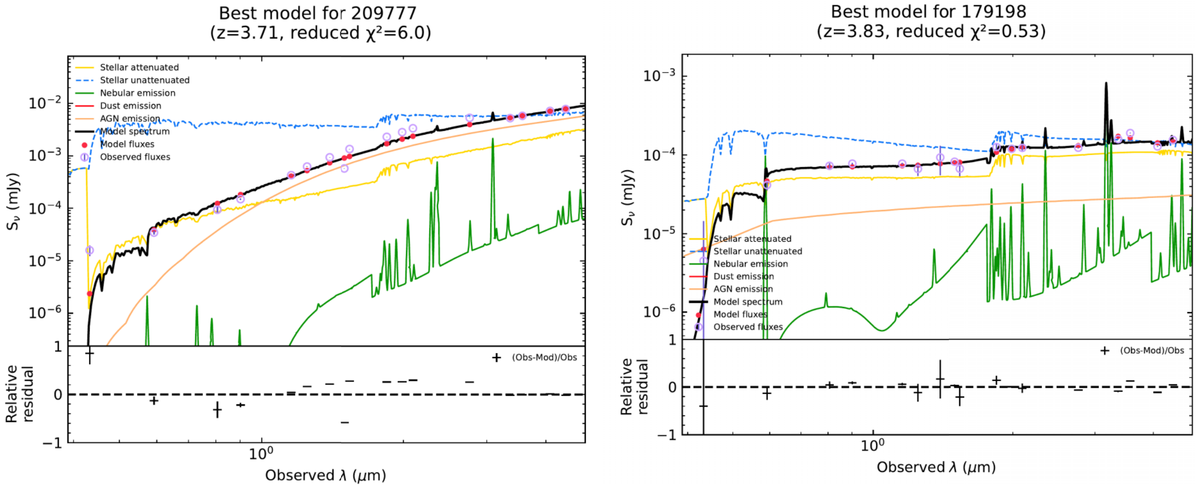

(c) GS-209777, `CIGALE`

(d) GS-179198, `CIGALE`

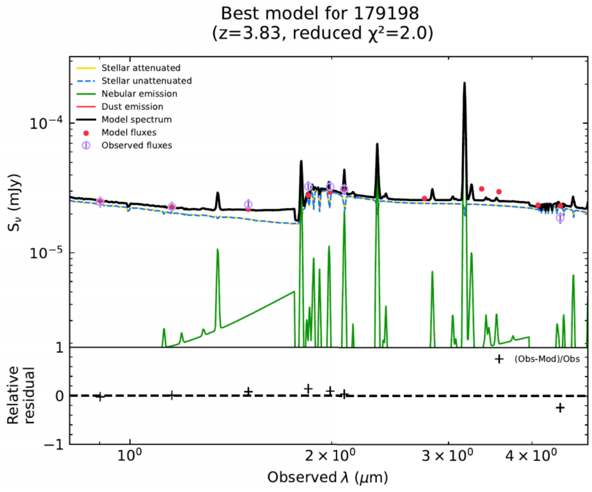

(e) GS-179198, `ForcePho`

Figure E1. Examples of SED fits to our sample sources. Panels **a** and **b** show `BEAGLE` fits to GN-53757 and GS-209777, respectively. The prism spectrum is shown in red, the best fit in blue, and the lighter colours denote masked regions. It is apparent that `BEAGLE` fails to reproduce the GS-209777 spectrum while performing well for GN-53757. Panels **c** and **d** show `CIGALE` fits to GN-209777 and GS-179198, respectively. `cigale` fitting leaves significant residuals for GN-209777, hence we do not use the resultant stellar mass estimates. Panel **e** shows `cigale` fit to `ForcePho` photometry of GS-179198.

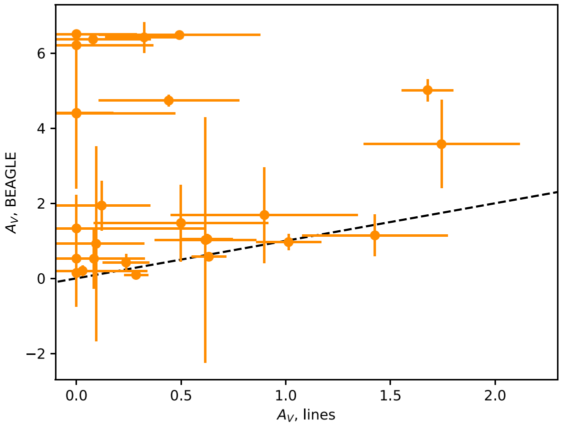

Figure E2. A comparison between the A_V values measured from the Balmer decrement of hydrogen lines (x-axis) and A_V derived from BEAGLE fits (y-axis). The uncertainties on BEAGLEA_V reflect both fitting and systematic errors incorporated in the same way as those on BEAGLEM_* . As shown in the plot, most sources are consistent with a 1–1 relation, except for a subset consisting almost entirely of LRDs.

This paper has been typeset from a TEX/LATEX file prepared by the author.